Palaeoproterozoic eclogites record lithobaric mixing during subduction and exhumation

Thesis submitted in accordance with the requirements of the University of Adelaide for an Honours Degree in Geology

Dillon Albert Brown

October 2018

THE UNIVERSITY of ADELAIDE

PALAEOPROTEROZOIC ECLOGITES RECORD LITHOBARIC MIXING DURING SUBDUCTION AND EXHUMATION

RUNNING TITLE: Ancient eclogites and metapelites in Tanzania

ABSTRACT

The interrogation of mineral assemblages that preserve evidence of having reached eclogite-facies conditions provides insight into the thermal state of subduction regimes. One of the first appearances of such assemblages in the geological record is documented in the Palaeoproterozoic Usagaran Belt in central Tanzania, where ca. 2000 Ma relic eclogite-facies assemblages are preserved. The eclogites contained the assemblage garnet + omphacite + rutile + quartz and have subsequently been overprinted by diopside + plagioclase + hornblende + ilmenite ± orthopyroxene. The eclogitic domains are preserved within low-strain domains, and these are encased by comparatively high-strain garnet-kyanite metapelitic gneisses and garnet-bearing mafic gneisses. Mineral equilibria forward modelling indicate that the eclogites reached minimum peak pressures of ca. 15–18 kbar and Zr-in-rutile thermometry applied to armoured rutile in garnet yields peak temperatures of 755–768 °C. Peak pressure–temperature (*P–T*) conditions are consistent with a cool geothermal gradient of 460 °C/GPa. The retrograde history of the eclogite-facies rocks is characterised by post-peak near-isothermal decompression to granulite-facies conditions of 6.5–7 kbar and 800 °C. Elevated Zr concentrations in fine-grained rutile and the preservation of prograde compositional zoning in garnet indicates that peak metamorphic conditions and near-isothermal exhumation occurred within ca. 1 Ma. The comparatively high-strain metapelitic domains record lower peak pressures (7.3–8.3 kbar and 683–700 °C) than the relic eclogites, indicative of a separate *P–T* history where the maximum *P–T* conditions coincide approximately with the post-peak assemblages in the

eclogites. In light of the results from mineral equilibria forward modelling, the regional-scale association between the relic eclogites and high-strain gneisses is consistent with an exhumation model involving either extrusion or extension, or a combination of both. This model permits the juxtaposition of deeply buried rocks with mid-crustal material.

KEYWORDS

Tanzania, Palaeoproterozoic, subduction, eclogite, metapelite, high-pressure, metamorphism, pseudosection

TABLE OF CONTENTS

LIST OF FIGURES AND TABLES

1. INTRODUCTION

When and how did subduction-driven geodynamics begin on Earth? These questions are controversial, and still unresolved. A growing body of literature suggests widespread subduction began in the late Mesoarchean (Nutman *et al*., 2002; Smithies *et al*., 2005; Brown, 2006; Cawood *et al*., 2006; Moyen *et al*., 2006; Van Kranendonk *et al*., 2007; Shirey & Richardson, 2011). Other views suggest that subduction-driven geodynamics emerged much later, potentially in the Neoproterozoic (Hamilton, 1998, 2011; Stern, 2005, 2007, 2016). Brown (2006) described the hallmark of subduction-related processes as the first appearance of dual metamorphic belts in the geological record. That is, the occurrence of high-temperature granulite metamorphic belts and associated high-pressure metamorphic belts. The subsequent appearance of both high-pressure and ultrahigh-pressure metamorphic rocks in the Neoproterozoic (Fig. 1) is inferred to mark the onset of modern-style plate tectonics – a variant form of plate tectonics akin to present day processes (Stern, 2005; Brown, 2006, 2007; Brown & Johnson, 2018).

Eclogites form at high pressures and low to medium temperatures. Metamorphism along low geothermal gradients is attributable to subduction regimes and as such, eclogites and associated high-pressure rocks are widely interpreted to record the thermal state of palaeosubduction systems (Hacker, 1996; Brown, 2006).

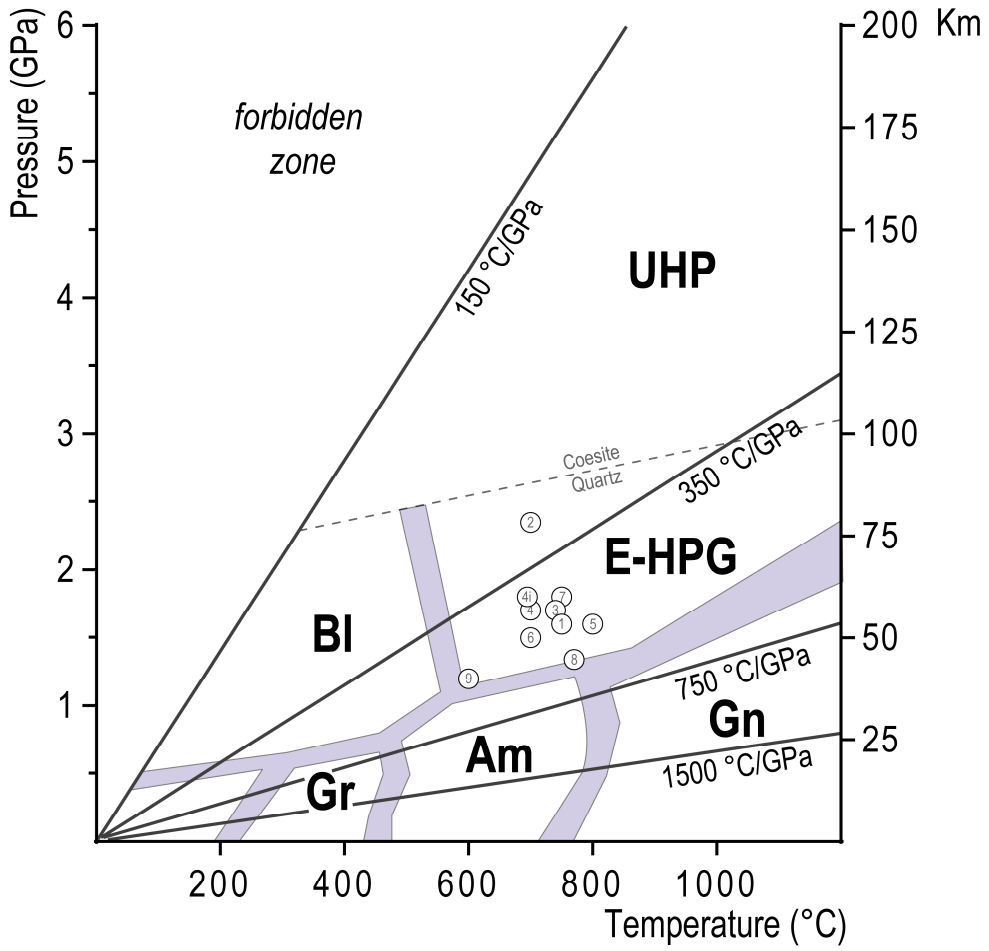

Fig. 1: Peak pressure–temperature (*P–T*) conditions for Palaeoproterozoic eclogites observed in the geological record. (1): Snowbird Tectonic Zone, Canada (Baldwin *et al*., 2004, 2007), (2): Trans-Hudson Orogen, North America (Weller & St-Onge, 2017), (3): Nagssugtoqidian Orogen, South-East Greenland (Nutman *et al*., 2008; Müller *et al*., 2018), (4): Belomorian Province, Russia (Li *et al*., 2015, 2017; Yu *et al*., 2017), (5): Eburnian-Transamazonian Orogen, Southern Cameroon (Loose & Schenk, 2018), (6): Ubendian Orogen, Tanzania (Boniface *et al*., 2012), (7): Usagaran Orogen, Tanzania (Möller *et al*., 1995; Collins *et al*., 2004), (8): Hengshan Complex, North China (Zhao *et al*., 2001; Kröner *et al*., 2006), (9): Nimrod Orogen, Transantarctic Mountains, Antarctica (Peacock & Goodge, 1995; Goodge *et al*., 2001).Shown on the vertical axis to the right is the burial depth (in km) associated with the magnitude of pressure. The fields separated by the bold violet lines correspond to metamorphic facies where: Gr = Greenschist, Am = Amphibolite, Gn = Granulite, Bl = Blueschist, E-HPG = Eclogite-High Pressure Granulite, and UHP = Ultra High Pressure. Facies abbreviations are after Brown (2014). The transition from E-HPG to UHP is marked by the coesite-quartz transition (dashed grey line). The solid lines emanating from the origin of the plot represent various geothermal gradients (annotated) corresponding to different *P–T* regimes. Palaeoproterozoic eclogites fall within the E-HPG facies and adopt thermal gradients between 350 and 750 °C/GPa.

Although rocks older than ca. 1500 Ma having preserved evidence of reaching eclogite-facies conditions are rare (O'Brien & Rötzler, 2003), the fact that some examples exist in the geological record (Fig. 2; Table 1) suggests that modern-style subduction processes were operating by this time.

The scarcity of such rocks of this age has been argued to reflect either (1) an issue of preservation or (2) their lack of formation as a consequence of higher geothermal gradients inferred to have existed in the comparatively early Earth (Condie *et al*., 2016; Möller *et al*., 1995; Weller & St-Onge, 2017). Not only is there a paucity of evidence for either argument, but there is a question of how rocks behaved in early subduction systems. This is especially relevant when considering the association between mafic eclogites and their country rock hosts.

Relic eclogitic mineral assemblages preserved as boudins or lenses are consistently observed in association with host rocks at the outcrop scale (Table 1; Cuthbert *et al*., 2000; Chopin, 2003; Reddy *et al*., 2003; Collins *et al*., 2004; Bousquet, 2008; Palmeri *et al*., 2009). Notably, the host rocks invariably lack eclogitic mineral assemblages. Rock associations of this sort are commonly interpreted to represent metamorphism of a single rock package, where the existing mineralogical variability between rocks is argued to reflect the eradication of high-pressure mineral assemblages in some of the eclogitic rocks during exhumation. Despite such explanations, the question of whether high-pressure assemblages and their structural hosts typically record a contemporaneous history (Meyre *et al*., 1999; Chopin & Schertl, 1999; Yea *et al*., 2000; Cuthbert *et al*., 2000; Liu *et al*., 2001; Janák *et al*., 2009) or a separate subduction-related history – where their association

may be better explained by a structural mixing process (Liu *et al*., 2003; Štípská *et al*., 2006; Bousquet, 2008) – is one that remains enigmatic.

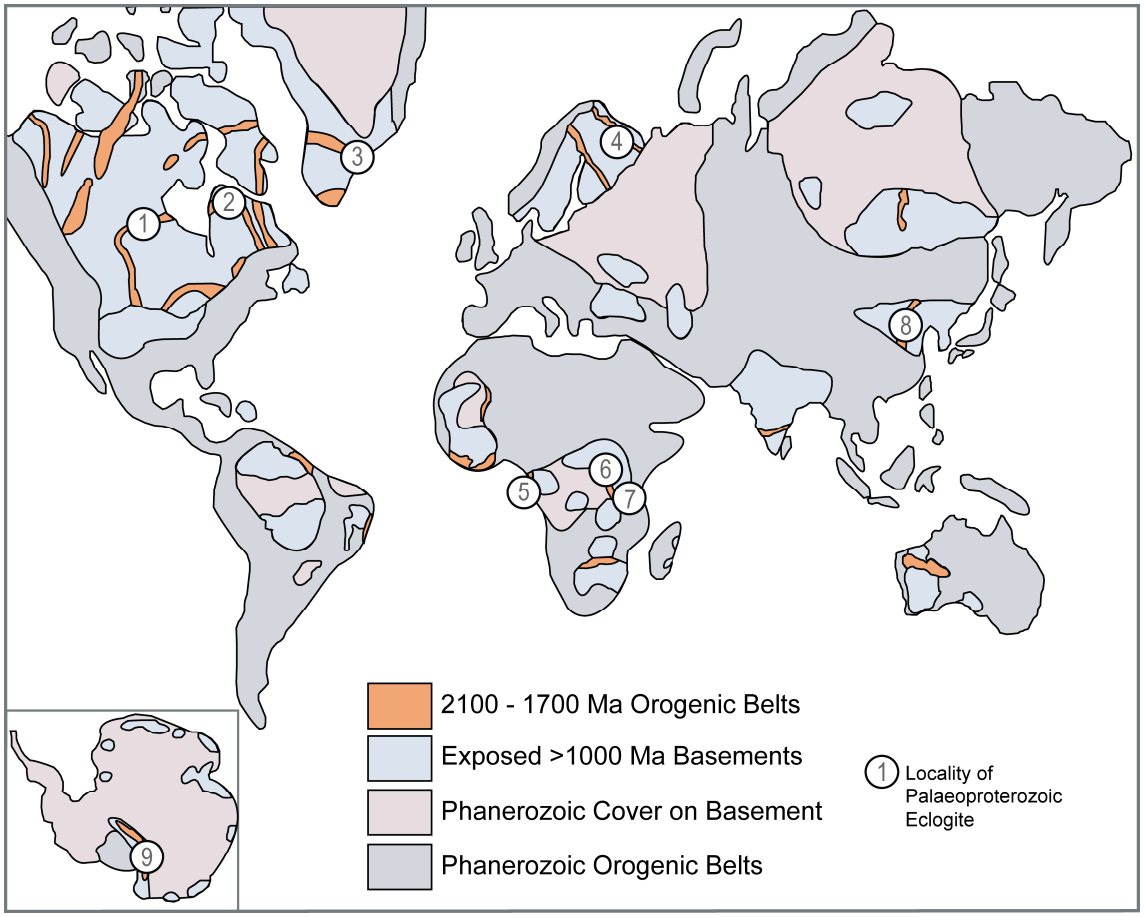

Fig. 2: Global distribution of documented Palaeoproterozoic eclogites. The numbered identifiers for each eclogite example correlate with those presented in Figure 1. Figure modified from Boniface *et al*. (2012). (1): Snowbird Tectonic Zone, Canada (Baldwin *et al*., 2004, 2007), (2): Trans-Hudson Orogen, North America (Weller & St-Onge, 2017), (3): Nagssugtoqidian Orogen, South-East Greenland (Nutman *et al*., 2008; Müller *et al*., 2018), (4): Belomorian Province, Russia (Li *et al*., 2015, 2017; Yu *et al*., 2017), (5): Eburnian-Transamazonian Orogen, Southern Cameroon (Loose & Schenk, 2018), (6): Ubendian Orogen, Tanzania (Boniface *et al*., 2012), (7): Usagaran Orogen, Tanzania (Möller *et al*., 1995; Collins *et al*., 2004), (8): Hengshan Complex, North China (Zhao *et al*., 2001; Kröner *et al*., 2006), (9): Nimrod Orogen, Transantarctic Mountains, Antarctica (Peacock & Goodge, 1995; Goodge *et al*., 2001).

Table 1: Summary of previous studies concerning eclogites of Palaeoproterozoic age. Temperature and pressure refer to peak conditions. Geothermal gradients are calculated from minimum peak pressure–temperature estimates. Mineral abbreviations after Whitney and Evans, (2010): Zrn: zircon, Mnz: monazite, Ttn: titanite.

Terrane	*Location*	*Sample*	*Peak Age (Ma)*	*Retrograde Age (Ma)*	*Temperature (°C)*	*Pressure (kbar)*	*Geothermal Gradient (°C/GPa)*	*MORB-type Geochemistry?*	*Boudins/lenses within hosts?*
Usagaran Belt	Tanzania	Eclogite	1999.1 ± 1.1 U–Pb (Zrn) (Collins *et al*., 2004)	1991 ± 2 U–Pb (Zrn) (Collins *et al*., 2004) 1996 ± 2 U–Pb (Ttn) (Möller *et al*., 1995)	750–800 (Möller *et al*., 1995)	18 (Möller *et al*., 1995)	417	Yes (Möller *et al*., 1995)	Yes (Möller *et al*., 1995)
Ubendian Belt	Tanzania	Eclogite	1886 ± 16 U–Pb (Zrn) (Boniface *et al*., 2012)	1831 ± 11 U–Pb (Mnz) (Boniface *et al*., 2012) 1817 ± 26 U–Pb (Zrn) (Boniface *et al*., 2012)	700 (Boniface *et al*., 2012)	15 (Boniface *et al*., 2012)	467	Yes (Boniface *et al*., 2012)	Yes (Sklyarov *et al*., 1998)
Belomorian Province	Russia	Uzkaya Salma Eclogite	2000-1900 U–Pb (Zrn) (Li *et al*., 2017)	1830–1800 U–Pb (Zrn) (Li *et al*., 2017)	700–750 (Li *et al*., 2017)	17-18 (Li *et al*., 2017)	412	Yes (Skublov *et al*., 2010)	Yes (Volodichev *et al*., 2004; Mints *et al*., 2010; Li *et al*., 2015)
		Gridino Eclogite	1900 U–Pb (Zrn) (Yu *et al*., 2017)	-	695–755 (Yu *et al*., 2017)	>18 (Yu *et al*., 2017)	386	Yes (Li *et al*., 2015)	
Snowbird Tectonic Zone	Canada	Eclogite	1904 ± 0.3 U–Pb (Zrn) (Baldwin *et al*., 2004, 2007)	1895 U–Pb (Ttn) (Baldwin *et al*., 2004, 2007)	750 (Baldwin *et al*., 2004, 2007)	16 (Baldwin *et al*., 2004, 2007)	469	-	Yes (Baldwin *et al*., 2004, 2007)

Hengshan Complex	China	Eclogite	1850 ± 3 U–Pb (Zr) (Kröner *et al*., 2006)	-	770–840 (Zhao *et al*., 2001)	13.4–15.5 (Zhao *et al*., 2001)	575	-	Yes (Zhao *et al*., 2001)
Trans-Hudson Orogen	North America	Eclogite	1830.8 ± 4.7 U–Pb (Mnz) (Weller & St-Onge, 2017)	-	700–770 (Weller & St-Onge, 2017)	23.5–26.5 (Weller & St-Onge, 2017)	298	-	Yes (Weller & St-Onge, 2017)
Nagssugtoqidian Orogen	South-East Greenland	Eclogite	1870 U–Pb (Zr) (Nutman *et al*., 2008)	-	740–810 (Müller *et al*., 2018)	17–19 (Müller *et al*., 2018)	435	-	Yes (Nutman *et al*., 2008)
Eburnian-Transamazonian Orogen	Southern Cameroon	Eclogite	2093 ± 45 U–Pb (Zr) (Loose & Schenk, 2018)	-	800 (Loose & Schenk, 2018)	16–20 (Loose & Schenk, 2018)	500	Yes (Loose & Schenk, 2018)	Yes (Loose & Schenk, 2018)
Nimrod Orogen, Transantarctic Mountains	Antarctica	Eclogite	1730 U–Pb (Zr) (Goodge *et al*., 2001)	-	600–900 (Peacock & Goodge, 1995)	12–25 (Peacock & Goodge, 1995)	360	-	Yes (Loose & Schenk, 2018)

The Palaeoproterozoic Usagaran Belt in central Tanzania (Fig. 3a) preserves some of the oldest known relic eclogite-facies mineral assemblages, with ages of ca. 2000 Ma (Möller *et al*., 1995; Collins *et al*., 2004). Rudimentary thermobarometric methods have derived peak pressures of 18 kbar and temperatures of 750 °C (Möller *et al*., 1995), and geochemical arguments suggest the protoliths to the eclogites had MORB-like compositions (Möller *et al*., 1995; Lau, 2009). These findings are consistent with a subduction-related model for the development of the Usagaran eclogites. The relic eclogitic assemblages are located at Yalumba Hill, ca. 2 km south-east of Rudi village (Fig. 3b). This km-scale domain of relic high-pressure assemblages is regionally enclosed by high-strain migmatitic rocks that are well-exposed along a section of the Great Ruaha River, ca. 15 km south-west of Yalumba Hill (Fig. 3b; Möller *et al*., 1995; Reddy *et al*., 2003; Collins *et al*., 2004).

The pressure–temperature (*P–T*) conditions of the Usagaran eclogites and their enclosing high-strain fabrics are based on outdated methods. Furthermore, there exists a poor understanding of the tectonometamorphic relationship between the relic eclogites and the high-strain domains that enclose them. That is; do they share a common history as part of a coherently subducted and exhumed slab, or is their present-day association explained by structural juxtaposition and mixing? Current models for the Usagaran eclogites suggest they represent comparatively low-strain domains but share the same tectonometamorphic history as the enclosing high-strain rocks (Möller *et al*., 1995; Reddy *et al*., 2003).

The principal aims of this study are to constrain the peak metamorphic conditions of the Usagaran eclogites and the high-strain fabrics that enclose them. This will be accomplished using mineral equilibria forward modelling and modern thermobarometric techniques to elucidate the tectonometamorphic relationship between the relic eclogites and the enclosing high-strain rocks. An ancillary aim of this study is to place constraints on the timing of peak metamorphism in the high-strain fabrics. These aims articulate with the overarching goal to better understand the exhumation dynamics of ancient eclogites such as those preserved in the Usagaran Belt.

2. GEOLOGICAL BACKGROUND

Regionally, the Usagaran Belt is bordered by the ca. 2700 Ma Tanzanian Craton to the north-west and to the east, is the ca. 655–610 Ma East-African Orogen (Fig. 3a; Möller *et al*., 2000; Muhongo *et al*., 2001). To the west of the Usagaran Belt lies the Palaeoproterozoic Ubendian Orogen. The Usagaran Belt comprises two lithological units: the medium- to high-grade Isimani Suite and the lower grade Konse Group (Fig. 3b). The Konse Group consists of conformable sedimentary and volcanic formations that unconformably overlie the Isimani Suite (Mruma, 1989).

The most common rock types in the Isimani Suite are medium- to high-grade gneisses of mafic and metapelitic character. Migmatitic biotite-bearing gneisses consist of alternating quartzofeldspathic domains, and coarse-grained kyanite-garnet metapelitic gneisses are interlayered with garnet-bearing amphibolites. The metapelitic gneisses (Fig. 4a) preserve the mineral assemblage: garnet + kyanite + K-feldspar + quartz + biotite + plagioclase (Möller *et al*., 1995).

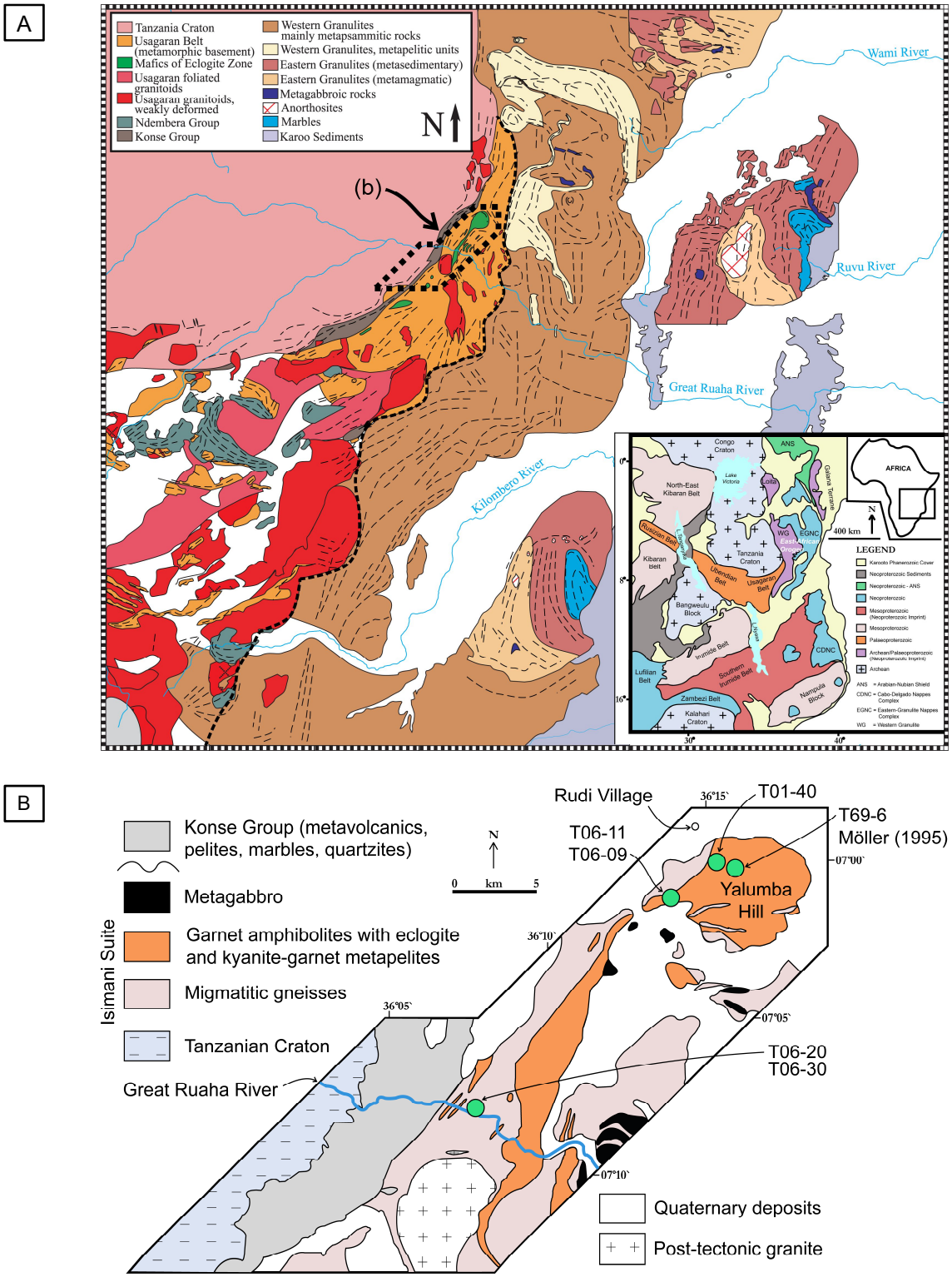

Fig. 3: (A) Regional geological map of central Tanzania including strike line contours. The region corresponding to (b) is the locality of this study. Map modified from Fritz *et al.* (2005). The inset map shows the geology of central-eastern Africa comprising the Tanzanian Craton, Ubendian Orogen, Usagaran Orogen and the East-African Orogen – modified from Boniface and Appel (2018). (B) Geological map of the Usagaran Orogen showing the sample localities (green circles) at the Great Ruaha River and Yalumba Hill. Included is sample T69-6 from Möller (1995) – map modified from Reddy *et al.* (2003).

Deformed migmatitic mafic gneisses (Fig. 4b, c) preserve mineral reaction textures consistent with garnet breakdown to fine-grained hornblende and plagioclase symplectites. The low-strain domains enclosed by the felsic-amphibolite-pelitic gneisses are typically preserved as boudins (Fig. 4d) and comprise relic eclogitic assemblages. Möller (1995) inferred a former eclogitic mineralogy based on the occurrence of omphacite in a single garnet porphyroblast. The overall mineral assemblage assigned to these domains is garnet, clinopyroxene, plagioclase, hornblende and quartz (Möller *et al*., 1995).

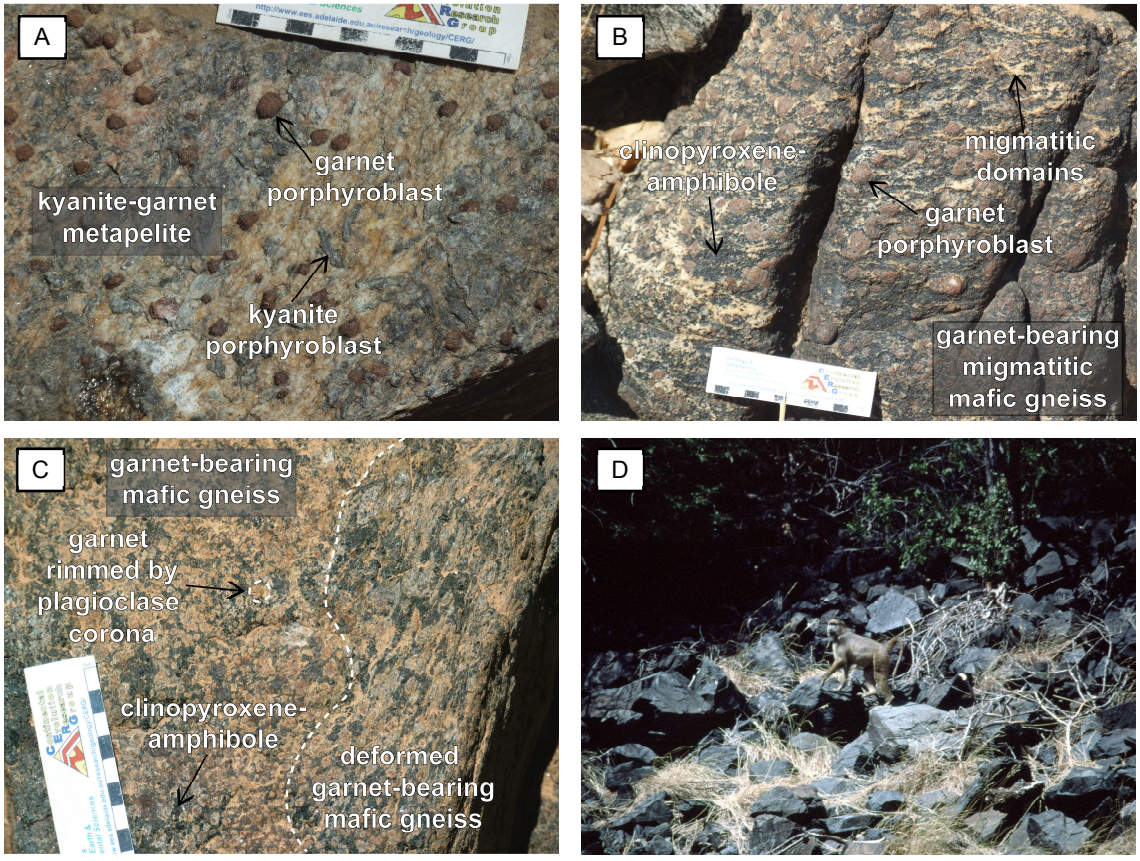

Fig. 4: (A) Kyanite-garnet metapelite (186492E, 9208414N) with large, red-brown garnets and grey-blue kyanite porphyroblasts – Great Ruaha River. (B) Migmatitic mafic gneiss (186225E, 9208532N) with garnet porphyroblasts, a clinopyroxene-amphibole matrix and quartzofeldspathic migmatitic domains – Great Ruaha River. (C) Mafic gneiss (186225E, 9208532N) comprising garnet surrounded by plagioclase coronae. To the right is a deformed domain, preserving garnet wrapped by clinopyroxene and amphibole – Great Ruaha River. (D) Massive, unfoliated partially retrogressed eclogite domains (199072E, 9227224N) – Yalumba Hill (Photo courtesy of Alan Collins). All coordinates are given in datum WGS 84 and grid 37S.

SHRIMP U–Pb zircon ages of ca. 2700 Ma from Isimani gneisses are interpreted to reflect the crystallisation ages of igneous protoliths (Reddy *et al*., 2003; Collins *et al*., 2004). Collins *et al*. (2004) inferred from detrital zircon SHRIMP U–Pb ages from a kyanite-garnet gneiss that the metapelitic rocks likely comprise a cover sequence atop ca. 2700 Ma granitoids of the Tanzania Craton (Möller *et al*., 1998; Maboko, 2000).

A SHRIMP U–Pb zircon age of 1999.1 ± 1.1 Ma from a retrogressed eclogite at Yalumba Hill is inferred to represent the timing of the eclogite-facies metamorphic event within the Isimani Suite (Collins *et al*., 2004). Monazite and rutile from the metapelitic high-strain domains enclosing the eclogitic domains yield a similar U–Pb age of 1999.5 ± 1.4 Ma (Möller *et al*., 1995), and zircon rims from an Isimani kyanite-garnet gneiss give a SHRIMP U–Pb age of 1989 ± 10 Ma (Collins *et al*., 2004).

Constraints on the retrograde evolution of the Usagaran Orogen are provided through titanite and zircon ages from mafic eclogite and pegmatite. Möller *et al*. (1995) obtained a U–Pb titanite cooling age of 1996 ± 2 Ma (T_c = 600-650 °C) for the eclogite and Collins *et al*. (2004) dated pegmatite-hosted zircons, yielding a SHRIMP U–Pb age of 1991 ± 2 Ma. The pegmatite cross-cut amphibolite-facies mylonites that overprint the eclogite-facies assemblages.

A greenschist-facies Neoproterozoic overprint has been identified for the Usagaran rocks. Rb–Sr biotite-whole-rock data for both Isimani gneisses and post-tectonic granites return ages of 1956 ± 53 Ma to 432 ± 5 Ma. Discordant U–Pb rutile ages from retrogressed eclogites show a lower intercept of 501 ± 26 Ma (Möller *et al*., 1995), recently validated

by an $^{40}Ar/^{39}Ar$ muscovite age of 535.4 ± 2.3 Ma from Isimani orthogneisses (Reddy *et al*., 2004). The ages of greenschist-facies metamorphism are likely associated with the development of the East-African Orogen (Fig. 3a; Möller *et al*., 1995; Reddy *et al*., 2004; Collins *et al*., 2004).

Three phases of deformation have been identified in the Usagaran Orogen. The first is correlated with the development of eclogite- and amphibolite-facies mineral assemblages (Mruma, 1989; Reddy *et al*., 2003). A second deformation event defined by amphibolite-facies assemblages is recorded by mylonitic foliations that overprint earlier fabrics (Reddy *et al*., 2003). Foliation geometries are consistent with a sinistral shear regime, likely associated with the exhumation of the Isimani Suite. Greenschist-facies shear zones, likely associated with the Neoproterozoic East-African Orogeny, cut earlier structural features.

Previous interpretations of the geotectonic evolution of the Usagaran Orogen suggest the subduction of the Isimani Suite was south-east dipping (Ring *et al*., 1997) and involved deep burial of a rifted marginal zone of the Tanzanian Craton, leading to metamorphism at eclogite-facies conditions (Reddy *et al*., 2003). Previous tectonic models all share at least one feature in common; they describe an exhumation history consistent with all Isimani rock types forming part of a coherent subducting slab system.

3. ANALYICAL METHODS

Both major and rare-earth element mineral compositions were routinely measured using electron probe micro analysis (EPMA) and Laser Ablation–Inductively Coupled Plasma Mass-Spectrometry (LA–ICP–MS) methods. Instrument operating conditions are described in Appendix 1a.

3.1. Rutile U–Pb Geochronology

In-situ U–Pb rutile geochronology was undertaken on metapelitic samples following Zack *et al*. (2011). See Appendix 2b for petrographic descriptions of samples. The isotopic compositions of ^{204}Pb, ^{206}Pb, ^{207}Pb, ^{208}Pb, ^{208}U, ^{232}Th and ^{238}U were measured using a RESOlution LR 193 nm Excimer laser system coupled with an Agilent 7900x ICP–MS at Adelaide Microscopy. *Iolite* (Hellstrom *et al*., 2008; Woodhead *et al*., 2008; Paton *et al*., 2011) was utilized for data processing to account for instrument drift and downhole fractionation effects, and the rutile U–Pb standards R10 and R19 were used for calibration (Luvizotto *et al*., 2009). A common lead correction was applied to all analyses through the implementation of the appropriate data reduction schemes in *Iolite* (Petrus & Kamber, 2012; Chew *et al*., 2014), coupled with the common lead correction model proposed by Andersen (2002) and the Stacey and Kramers (1975) Pb evolution model. Given rutile typically incorporates negligible concentrations of ^{232}Th, ^{208}Pb was used as the common lead proxy (Zack *et al*., 2011). Detailed analytical methods are outlined in Appendix 1b.

3.2. Mineral Equilibria Forward Modelling

Mineral equilibria forward models were calculated using the thermodynamic calculation program THERMOCALC v.340/345, with the internally-consistent thermodynamic

dataset ds62 of Holland and Powell (2011) and the latest *a–x* (activity-composition) models for solid solution minerals models (White *et al*., 2000; Holland & Powell, 2003; Holland & Powell, 2011; White *et al*., 2014a; White *et al*., 2014b; Green *et al*., 2016). Pressure–temperature *(P–T)* models for mafic samples were calculated using the model chemical system, MnNCFMASHTO ($MnO–Na_2O–CaO–FeO–MgO–Al_2O_3–SiO_2–H_2O–TiO_2–Fe_2O_3$) whereas the modelled metapelitic sample was calculated with the addition of K_2O given its bulk-rock composition comprises significantly more K_2O. Pressure–composition *(P–X)* models – where 'X' denotes a proportion of Fe_2O_3 – were calculated with MnO excluded for mafic samples since the contribution of MnO to the mafic mineral assemblages is negligible. *P–X* models can be found in Appendix 2g.

All equilibria were calculated individually. This requires the user to identify which equilibria relationships are stable and to understand how equilibria relationships change as a function of pressure, temperature and mineral composition. This approach relies solely on critical thinking as opposed to 'black-box' calculations. Without a detailed understanding of stable and metastable equilibria, it is entirely feasible to calculate thermodynamically invalid equilibria models. The bulk-rock composition used to construct *P–X* and *P–T* models for T06-20 was altered to account for compositional fractionation effects induced by large garnet porphyroblasts. Appendix 1c provides information regarding bulk-rock adjustments.

3.3. Zr-in-Rutile Thermometry

Zr-in-rutile thermometry after Watson *et al*. (2006) and Tomkins *et al*. (2007) was undertaken on 30–250 μm rutile grains (most commonly 50–110 μm) in quartz- and

zircon-bearing samples using a RESOlution LR 193 nm Excimer laser system coupled with an Agilent 7900x ICP–MS at Adelaide Microscopy. In-situ grains hosted as inclusions in garnet porphyroblasts were targeted, as well as grains liberated by mineral separation. Garnet-hosted grains were selected to ensure that subsequent temperature estimates would best approximate peak metamorphic conditions. The primary standard, NIST-610 and the secondary standard, GSD-1G were used in data processing, undertaken using *Iolite*. Due to the variability in grain-sizes, the spot size was adjusted between 13 μm and 51 μm. To identify if Zr concentrations were influenced by spot-size, the downhole fractionation effect pertaining to the secondary standard GSD-1G was monitored between spot sizes. The extended methadology is given in Appendix 1d. To conserve space, Zr-in-rutile results are contained in Appendix 2h. However, it is stressed that the thermometry method is complex and time intensive to apply, requiring a detailed understanding of rutile chemistry, diffusion response and data processing.

3.4. Garnet-Orthopyroxene Thermometry

The garnet-orthopyroxene thermometer (Harley, 1984) was applied to garnet-orthopyroxene-bearing samples using the thermodynamic dataset of Holland & Powell (1998). The extended methodology is contained in Appendix 1e and results are presented in Appendix 2i.

3.5. Mineral Abundance Contours

Modelled mineral modal proportions arising from thermodynamic models were interrogated using TCInvestigator (TCI); (Pearce *et al*., 2015). This code allows mineral equilibria forward models to be contoured with respect to mineral abundance.

4. RESULTS

4.1. Samples

Table 2: Sample descriptions.

Location	*Rock type*	*Sample*	*Description*	*UTM Coordinates (WGS 84)*
Yalumba Hill	Retrogressed Eclogite	T01-40	garnet + clinopyroxene + plagioclase + hornblende + quartz + ilmenite + rutile + titanite + apatite	199072, 9227224
	Retrogressed Eclogite	T06-09	garnet + clinopyroxene + plagioclase + hornblende + quartz + orthopyroxene + ilmenite + rutile	195240, 9225768
	Retrogressed Eclogite	T06-11	garnet + clinopyroxene + plagioclase + hornblende + quartz + ilmenite + rutile + orthopyroxene + titanite	195240, 9225768
Great Ruaha River	High-strain Metapelite	T06-20	garnet + kyanite + plagioclase + biotite + quartz + hornblende + rutile + staurolite + chlorite + apatite + muscovite	186492, 9208414
	High-strain Mafic Gneiss	T06-30	garnet + amphibole + plagioclase + quartz + titanite + ilmenite + scapolite + rutile + clinopyroxene	186225, 9208532

4.2. Petrography

T01-40 Retrogressed Eclogite

T01-40 retrogressed eclogite has an inferred peak assemblage of garnet, clinopyroxene, quartz and rutile. The retrograde assemblage comprises clinopyroxene, garnet, hornblende, plagioclase, quartz and ilmenite. Fine- to coarse-grained (0.5–2.5 mm) garnet hosts inclusions of quartz, plagioclase, rutile, titanite, ilmenite, apatite, hornblende and clinopyroxene (Fig. 5a), and plagioclase coronae separate garnet porphyroblasts from clinopyroxene present in the matrix. Clinopyroxene is fine- to coarse-grained (0.5–2 mm)

and overprinted by medium-grained, subhedral to anhedral hornblende. Plagioclase is present as intergrowths in clinopyroxene (Fig. 5b). Secondary garnet-plagioclase symplectites rim fine- to coarse-grained matrix ilmenite. Present in the matrix is fine-grained titanite and coarse-grained apatite (Appendix 2a).

T06-09 Retrogressed Eclogite

T06-09 consists of garnet porphyroblasts (1–4 mm) that host inclusions of quartz, rutile, ilmenite and minor clinopyroxene. Constituting the matrix is fine-grained (<1 mm) hornblende, fine- to coarse-grained (1–2 mm) ilmenite, quartz, plagioclase and secondary clinopyroxene and orthopyroxene (Fig. 5c). Clinopyroxene hosts intergrowths of plagioclase and quartz and is typically overprinted by hornblende and orthopyroxene at its margins. Peak assemblage: garnet, clinopyroxene, quartz, rutile. Retrograde assemblage: clinopyroxene, garnet, plagioclase, hornblende, quartz, ilmenite and orthopyroxene.

T06-11 Retrogressed Eclogite

Coarse-grained domains defined primarily by garnet are layered between comparatively fine-grained clinopyroxene-rich domains (Appendix 2a). Garnet porphyroblasts (<1–1.5 mm) contain quartz, ilmenite and rutile inclusions, and are separated from clinopyroxene by plagioclase coronae. Anhedral clinopyroxene hosts fine-grained (0.5 mm) intergrowths of plagioclase, and defines the matrix alongside plagioclase, quartz, ilmenite, orthopyroxene, hornblende and minor titanite. The peak and retrograde assemblages are identical to sample T06-09.

T06-20 Metapelite

T06-20 metapelite comprises the interpreted peak assemblage: kyanite, garnet, biotite, hornblende, quartz, plagioclase and rutile. The retrograde assemblage is defined by the addition of chlorite and muscovite. Poikiloblastic garnet porphyroblasts (8–10 mm) are enclosed by a well-developed fabric dominated by kyanite, hornblende, biotite and minor staurolite. Garnet hosts inclusions of staurolite, biotite, quartz, plagioclase and rutile. Staurolite inclusions are present in kyanite porphyroblasts (Fig. 5d) and subhedral to euhedral staurolite occurs with rutile at the margins of coarse-grained kyanite and garnet. Similarly, subhedral chlorite is associated with secondary kyanite at the margins of porphyroblastic kyanite (Fig. 5e). Biotite and hornblende overprint garnet and kyanite porphyroblasts, and fine-grained muscovite overprints secondary kyanite. Leucosomic centimetre-scale domains comprising equigranular plagioclase, quartz and minor apatite are evident in the matrix (Appendix 2a).

T06-30 Mafic Gneiss

T06-30 contains 2–10 mm fractured garnet porphyroblasts that are pervasively rimmed by 1–4 mm wide amphibole-plagioclase symplectites (Fig. 5f). Medium- to coarse-grained (0.5–2 mm) amphibole overprints relic clinopyroxene porphyroblasts and within clinopyroxene porphyroblasts, are poorly preserved plagioclase lamellae. Subhedral titanite is associated with amphibole and host inclusions of rutile.

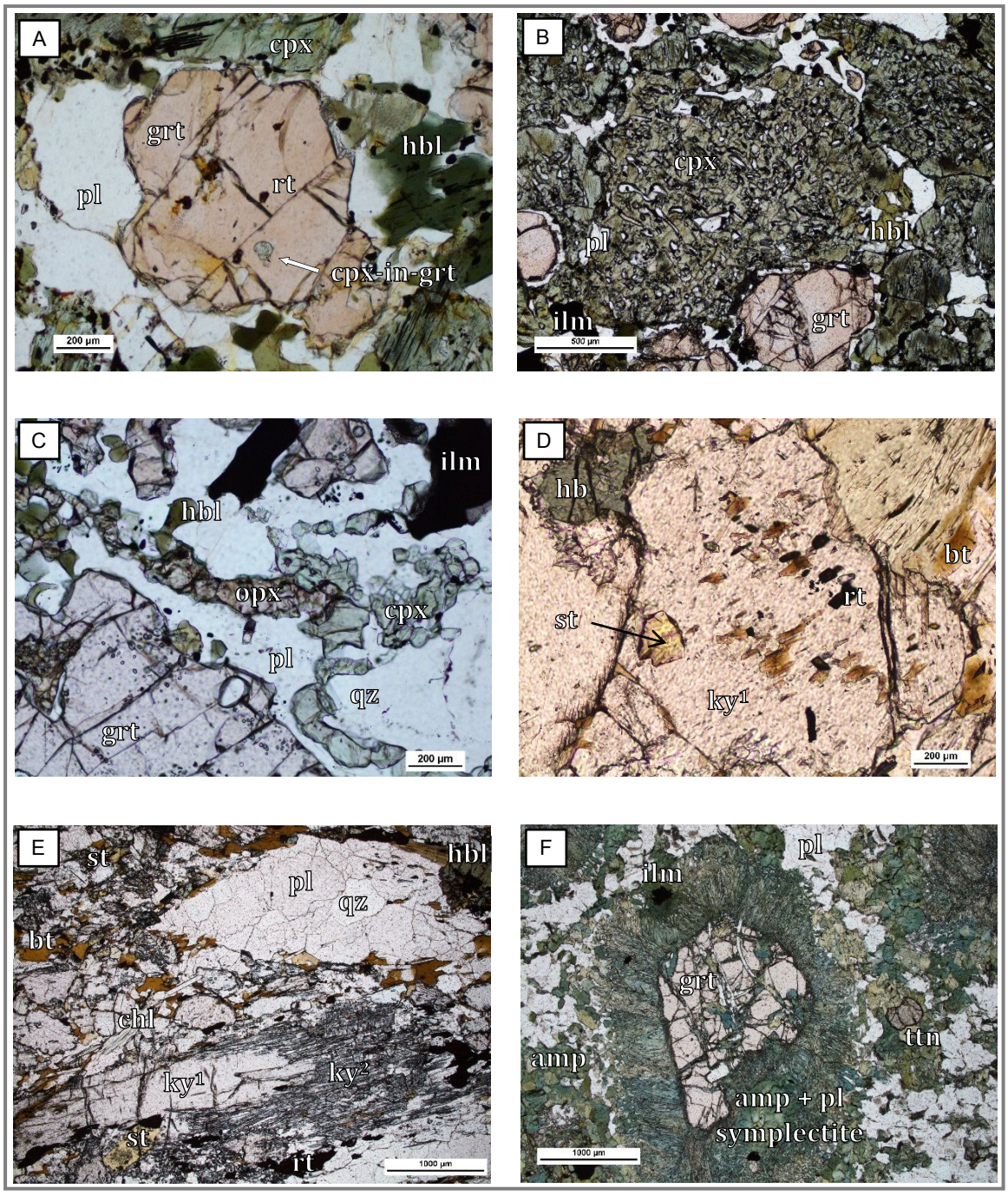

Fig. 5: Photomicrographs of petrological relationships. (A) T01-40: clinopyroxene and rutile inclusions within garnet. (B) T01-40: clinopyroxene with intergrowths of plagioclase. Hornblende overprints clinopyroxene at its edge and a plagioclase corona separates clinopyroxene from garnet. (C) T06-09: secondary orthopyroxene and associated clinopyroxene, separated from garnet by plagioclase. (D) T06-20: staurolite inclusion within kyanite. (E) T06-20: porphyroblastic kyanite replaced by kyanite needles. Staurolite, rutile and chlorite are associated with kyanite at its rim, and observed as part of the matrix are equigranular plagioclase and quartz leucosomic domains. (F) T06-30: fractured garnet porphyroblast is pseudomorphed by a symplectite of amphibole and plagioclase. Titanite and amphibole are present in the matrix. Abbreviations: amp(amphibole), bt(biotite), chl(chlorite), cpx(clinopyroxene), grt(garnet), hbl(hornblende), ilm(ilmenite), ky(kyanite), opx(orthopyroxene), pl(plagioclase), qz(quartz), rt(rutile), st(staurolite), ttn(titanite). Mineral abbreviations are consistent with those revised by Whitney and Evans (2010). Refer to Appendix 2a for extended petrographical images.

4.3. Mineral Chemistry

Garnet

Representative analyses for all minerals are presented in Appendix 2c and the relevant garnet end-member compositions are listed in Table 3. T01-40 garnet composition is predominantly almandine where $X_{(alm)}$ ($Fe^{2+}/Fe^{2+}+Mg+Ca+Mn$)) values range from 0.59 at the rim to 0.55 in the core (Fig. 6a, 7a). $X_{(sps)}$ ($Mn/(Fe^{2+}+Mg+Ca+Mn)$) enrichment is evident in the garnet core relative to the rim where values are 0.06 and 0.03, respectively (Fig. 6a, 7a). Similarly, T06-09 garnet (Fig. 6e) is almandine-rich, although all major elements are heterogeneously distributed across the garnet. Sample T69-6 metapelite – obtained from Möller (1995) – demonstrates core enrichment in $X_{(Fe)}$ ($Fe^{2+}/(Fe^{2+}+Mg)$) and $X_{(grs)}$ relative to garnet rims (Fig. 7c). T06-20 metapelite shows a garnet composition dominant in almandine (66–72%) where $X_{(alm)}$ increases from core to rim (Fig. 6d, 7d). Core enrichments in $X_{(Fe)}$ and $X_{(grs)}$ are observed in Figure 7d and $X_{(prp)}$ depletion in the core is evident. Rim to rim garnet end-member proportions for T06-30 are all similarly flat (Fig. 6a, 7b). Diffusional rim enrichment in $X_{(alm)}$, $X_{(sps)}$ and $X_{(grs)}$ ($Ca/(Fe^{2+}+Mg+Ca+Mn)$) is noticeable, while $X_{(prp)}$ ($Mg/(Fe^{2+}+Mg+Ca+Mn)$) shows rim depletion relative to the core. As with sample T01-40, the overall garnet composition is almandine-rich (57–65%).

Table 3: Mineral end-member proportions for garnet in selected samples. X(Fe) = the ratio: $Fe^{2+}/(Fe^{2+}+Mg)$. This ratio is defined in the *a–x* models used in THERMOCALC v.345.

Sample	*T01-40*		*T06-09*		*T06-20*		*T06-30*	
	Garnet (Core)	**Garnet (Rim)**	**Garnet (Core)**	**Garnet (Rim)**	**Garnet (Core)**	**Garnet (Rim)**	**Garnet (Core)**	**Garnet (Rim)**
X(Fe)	0.819	0.754	0.668	0.671	0.794	0.777	0.566	0.648
Almandine	0.588	0.553	0.497	0.507	0.664	0.717	0.440	0.492
Pyrope	0.130	0.180	0.247	0.248	0.172	0.206	0.338	0.267
Grossular	0.226	0.241	0.244	0.234	0.158	0.063	0.209	0.216
Spessartine	0.055	0.026	0.012	0.011	0.005	0.014	0.013	0.025

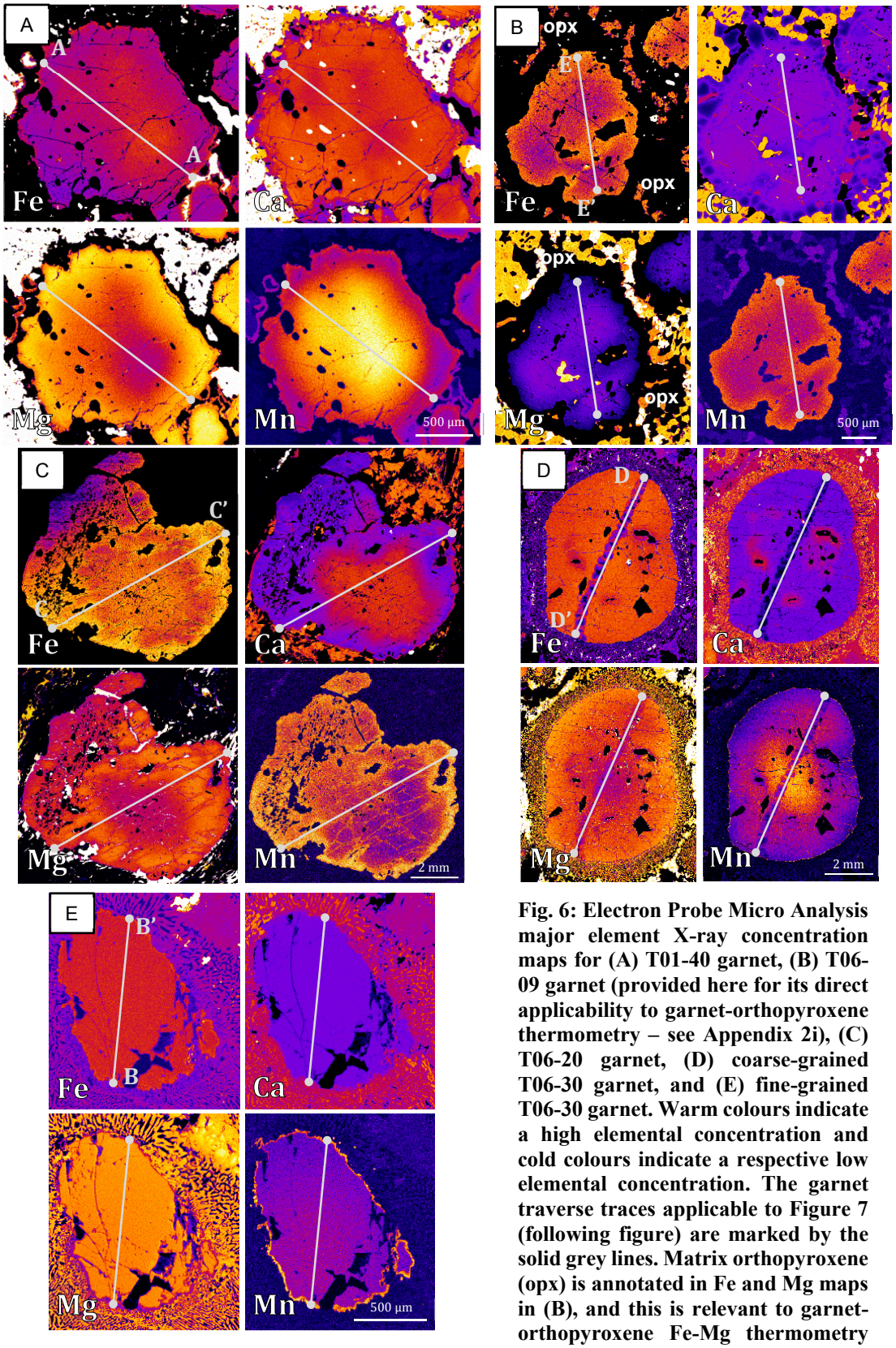

Fig. 6: Electron Probe Micro Analysis major element X-ray concentration maps for (A) T01-40 garnet, (B) T06-09 garnet (provided here for its direct applicability to garnet-orthopyroxene thermometry – see Appendix 2i), (C) T06-20 garnet, (D) coarse-grained T06-30 garnet, and (E) fine-grained T06-30 garnet. Warm colours indicate a high elemental concentration and cold colours indicate a respective low elemental concentration. The garnet traverse traces applicable to Figure 7 (following figure) are marked by the solid grey lines. Matrix orthopyroxene (opx) is annotated in Fe and Mg maps in (B), and this is relevant to garnet-orthopyroxene Fe-Mg thermometry (Appendix 2i).

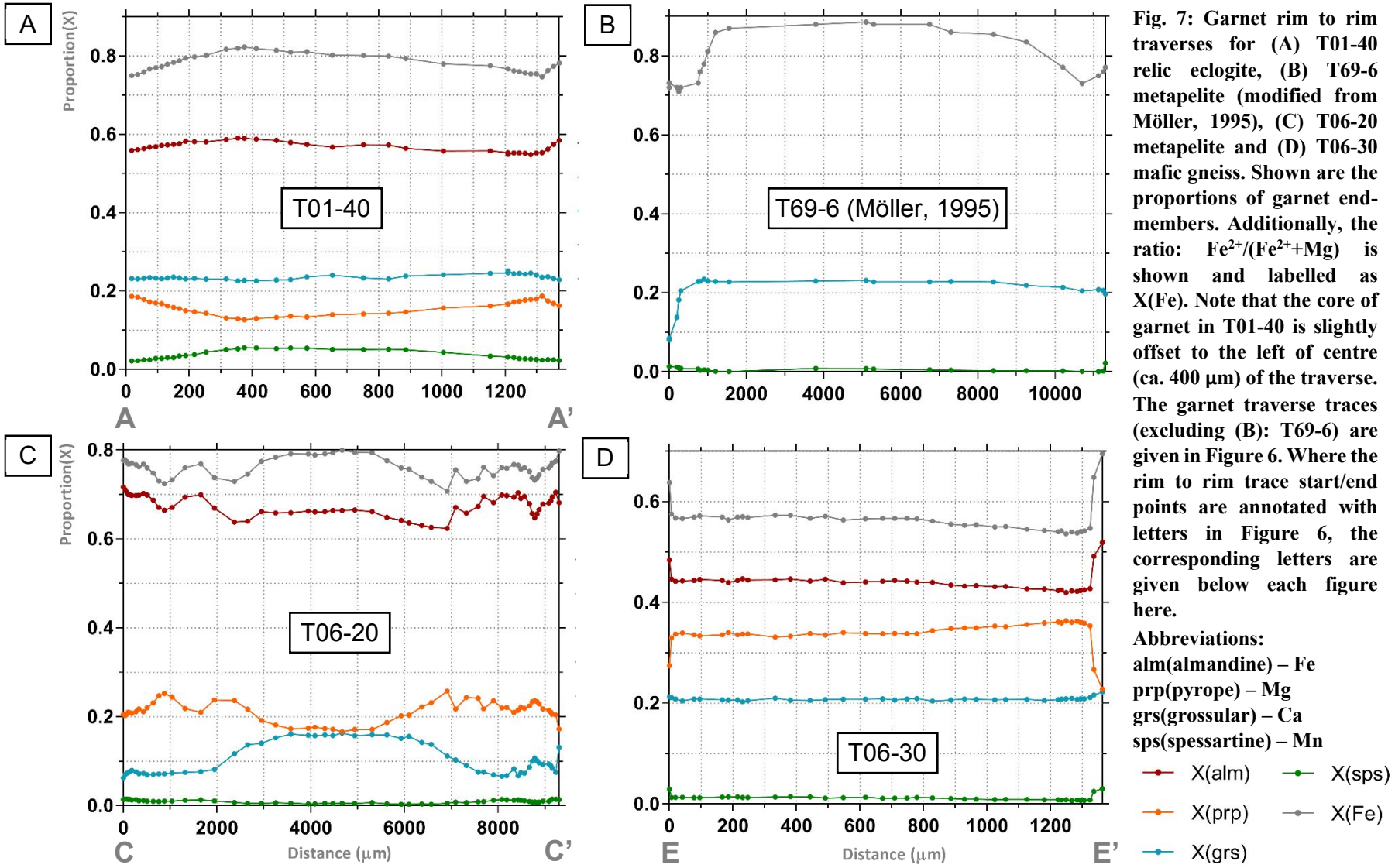

Fig. 7: Garnet rim to rim traverses for (A) T01-40 relic eclogite, (B) T69-6 metapelite (modified from Möller, 1995), (C) T06-20 metapelite and (D) T06-30 mafic gneiss. Shown are the proportions of garnet end-members. Additionally, the ratio: $Fe^{2+}/(Fe^{2+}+Mg)$ is shown and labelled as X(Fe). Note that the core of garnet in T01-40 is slightly offset to the left of centre (ca. 400 µm) of the traverse. The garnet traverse traces (excluding (B): T69-6) are given in Figure 6. Where the rim to rim trace start/end points are annotated with letters in Figure 6, the corresponding letters are given below each figure here.

Abbreviations:
alm(almandine) – Fe
prp(pyrope) – Mg
grs(grossular) – Ca
sps(spessartine) – Mn

Clinopyroxene

Representative clinopyroxene end-member compositions are shown in Table 4. Clinopyroxene in sample T01-40 is predominantly diopsidic in composition with $X_{(diop)}$ values ranging from 0.63–0.76 where the minimum values are derived from clinopyroxene included in garnet and the maximum from matrix clinopyroxene. $X_{(jad)}$ values decrease in matrix clinopyroxene with respect to clinopyroxene in garnet (from 0.10 to 0.02). Clinopyroxene in samples T06-09 and T06-11 is also diopsidic ($X_{(diop)}$ = 0.73–0.81) and in sample T06-09, $X_{(jad)}$ values are greater in included clinopyroxene (0.07) than in matrix clinopyroxene (0.02).

Table 4: Mineral end-member proportions for clinopyroxene in samples T01-40, T06-11 and T06-09. X(Fe) = the ratio: $Fe^{2+}/(Fe^{2+}+Mg)$. This ratio is defined in the *a–x* models used in THERMOCALC v.345.

Sample	*T01-40*		*T06-09*		*T06-11*
	Cpx^2 (matrix)	**Cpx^2 (incl. in Grt)**	**Cpx^2 (matrix)**	**Cpx^2 (matrix)**	**Cpx^2 (incl. in Grt)**
X(Fe)	0.197	0.289	0.140	0.237	0.206
Jadeite	0.024	0.100	0.036	0.017	0.066
Diopside	0.759	0.632	0.813	0.732	0.730
Hedenbergite	0.187	0.257	0.132	0.228	0.189
Aegirine	0.030	0.011	0.019	0.023	0.015

Plagioclase, Staurolite, Biotite, Chlorite & Amphibole

Representative analyses for plagioclase, staurolite, biotite, and chlorite in sample T06-20 are shown in Table 5. Matrix plagioclase is albite in composition (64%) and matrix biotite in T06-20 preserves an $X_{(Mg)}$ ($Mg/(Mg+Fe^{2+})$) value of 0.64, while chlorite, matrix staurolite and staurolite included in garnet preserve $X_{(Mg)}$ values of 0.668, 0.271 and 0.243, respectively. Amphibole in all samples is tschermakitic hornblende.

Table 5: Sample T06-20: mineral end-member proportions for plagioclase and X(Mg) values for plagioclase, biotite, chlorite and staurolite. X(Mg) is the ratio: Mg/(Mg +Fe^{2+}). This ratio is defined in the *a–x* models used in THERMOCALC v.340.

Sample	*T06-20*				
	Plagioclase	**Biotite**	**Chlorite**	**Staurolite**	**Staurolite (incl. in Ky)**
X(Mg)	-	0.638	0.668	0.271	0.243
Albite	0.638	-	-	-	-
Anorthite	0.359	-	-	-	-
Sanidine	0.002	-	-	-	-

4.4. Rare-Earth Element Distributions in Garnet

LA–ICP–MS garnet rare-earth element results are presented in Appendix 2e. Representative results are shown in Figure 8. Sample T01-40 garnet (ca. 1600 μm in diameter) shows elevated concentrations of both heavy-rare-earth elements (HREEs) and light-rare-earth elements (LREEs) in its core, with a progressive depletion in all elements toward the garnet rim. A central peak in yttrium is evident and is consistent with the trends exhibited by other HREEs. Garnet rims show prominent yttrium-rich annuli whereby the core-side slope is shallow relative to the outer slope. In sample T06-20 garnet (ca. 8500 μm in diameter), the core is depleted in both HREEs and LREEs relative to the garnet rim. These trends are most pronounced in yttrium and gadolinium. Like T01-40, prominent yttrium-rich annuli are apparent toward the garnet rims. T06-30 garnet (ca. 1200 μm in diameter) preserves a relatively flat LREE pattern whereas the HREEs exhibit a decreasing progression from one edge of the garnet to the other. HREEs in T06-30 garnet (ca. 7100 μm in diameter) are enriched in the core and show a depleting trend toward the garnet rim. As with the smaller T06-30 garnet, the LREE trend in this garnet is consistently flat from rim to rim.

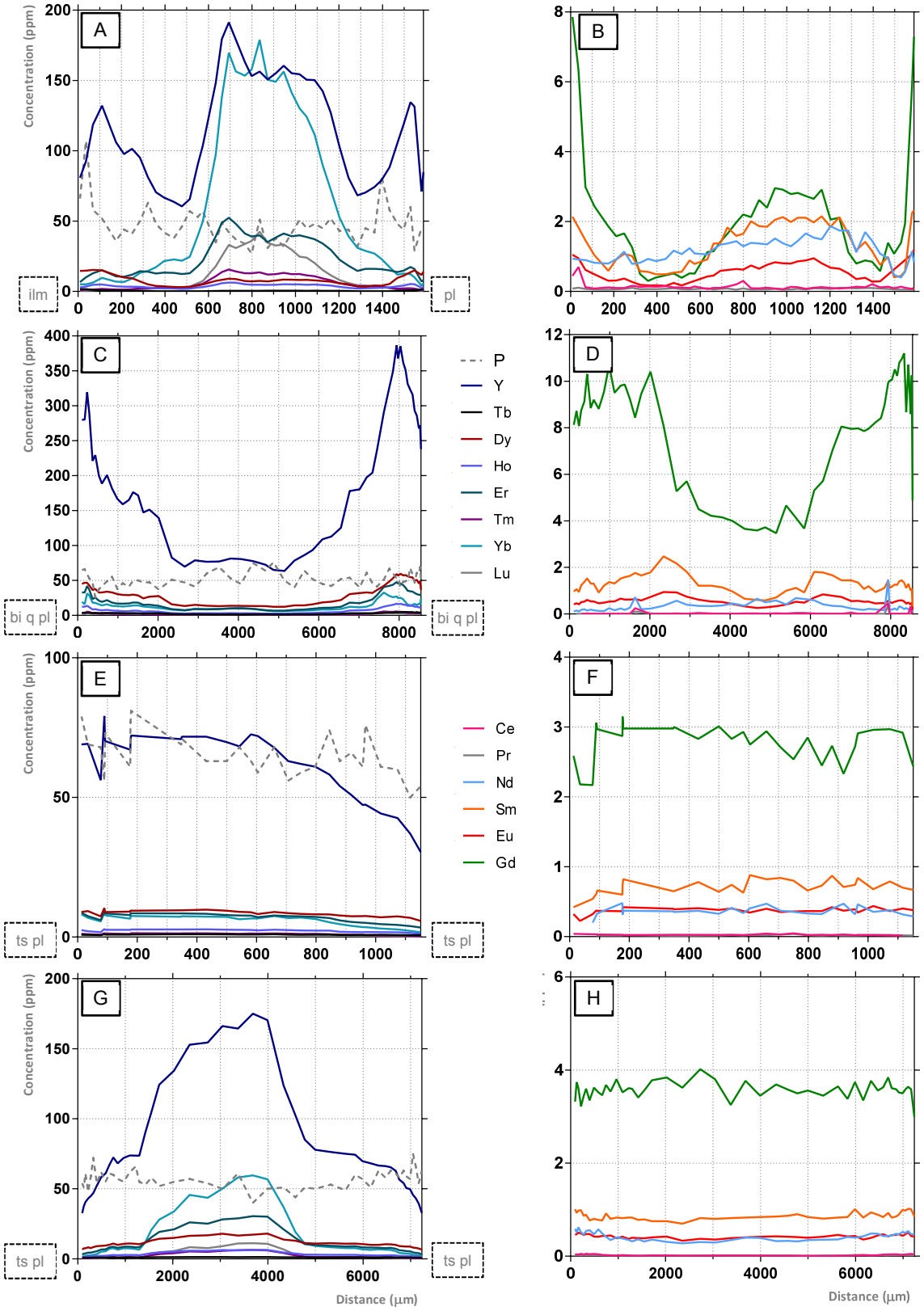

Fig. 8: LA–ICP–MS rare-earth element rim to rim traverses for (A-B) T01-40 garnet, (C-D) T06-20 garnet, (E-F) T06-30 garnet and (G-H) T06-30 coarse-grained garnet. (A, C, E, G) show rim to rim traverses for a selection of heavy REEs and (B, D, F, H) show the same for light REEs. Phosphorus is shown in (A, C, E, G) for reference (marked by the grey dashed line). The abbreviations at either side of (A, C, E, G) signify the matrix minerals adjacent to each garnet.

4.5. Rutile U–Pb Geochronology

Rutile U–Pb age data is presented in Appendix 2f. Reflected light petrographic images of in-situ rutile grains are shown in Figure 9. U–Pb rutile dating on metapelitic samples T06-20, T06-21, T06-21A and T06-27 was made challenging by five primary factors: (1) the small size of the rutile grains with respect to the ablation spot size, (2) the presence of common lead (^{208}Pb) as inferred by high ^{208}Pb counts, (3) the presence of ^{232}Th, which convolutes the interpretation of the amount of common lead, (4) evident lead loss and (5) low ^{238}U counts. Of the 61 rutile grains in garnet (of which all are inferred to be in equilibrium with prograde or peak assemblages given they are armoured within garnet), 7 of these analyses were omitted due to very low ^{238}U concentrations and 2 of these also exhibited markedly high ^{208}Pb concentrations (Fig. 10a). The remaining 54 analyses (Fig. 10b) all showed varying ^{208}Pb signatures. Two additional Tera-Wasserburg concordia plots were constructed (Fig. 11a, b); the first with the Andersen (2002) ^{208}Pb correction method and the second with the ^{208}Pb correction method outlined by Chew *et al*. (2014). The failure of these to adequately correct for ^{208}Pb (Fig. 11) may be attributed to the presence of ^{208}Pb, high ^{232}Th counts relative to the primary analytical standard, and lead loss (section 5.1). Consequently, an upper intercept age of 1985 ± 23 Ma based on the most concordant analyses is derived (>90% concordance, n = 9); these having been uncorrected for in ^{208}Pb (Fig. 10c).

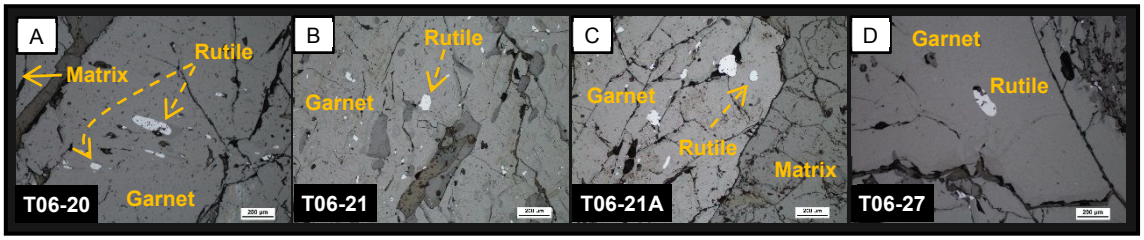

Fig. 9: Reflected light petrographic microscope images of armoured rutile grains in garnet for (A) sample T06-20, (B) sample T06-21, (C) sample T06-21A and (D) sample T06-27 – all of which were used in U–Pb rutile analysis. Rutile grains are proximal to garnet rims.

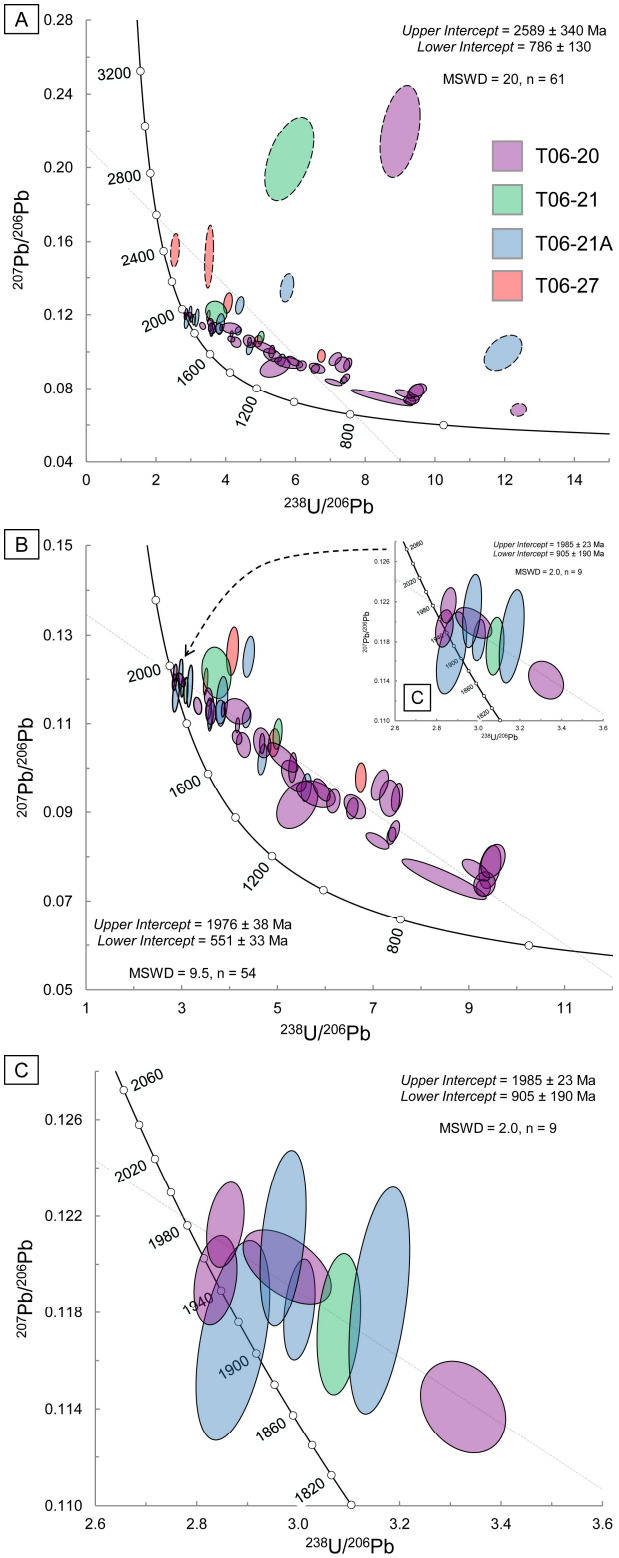

Fig. 10: (A-C) U-Pb Rutile Tera-Wasserburg concordia plots for samples T06-20, T06-21, T06-21A and T06-27. 2σ error ellipses are coloured based on the given sample, where red = T06-20, green = T06-21, blue = T06-21A and purple = T06-27. (A) Concordia for all analyses among all samples (n = 64). Ellipses bordered by a dashed line are those that have been excluded. (B) Concordia excluding inadequate analyses (n = 54, see text) where the analyses contributing to the calculation of the upper intercept (n = 9) are shown in inset. The lower intercept value in (B) quoted as 551 ± 33 Ma, although largely unimportant as it is poorly constrained, provides the most reasonable lower intercept age relative to all other concordia. (C) Enlarged inset figure from (B) showing the analyses contributing to the upper intercept age (1985 ± 23 Ma).

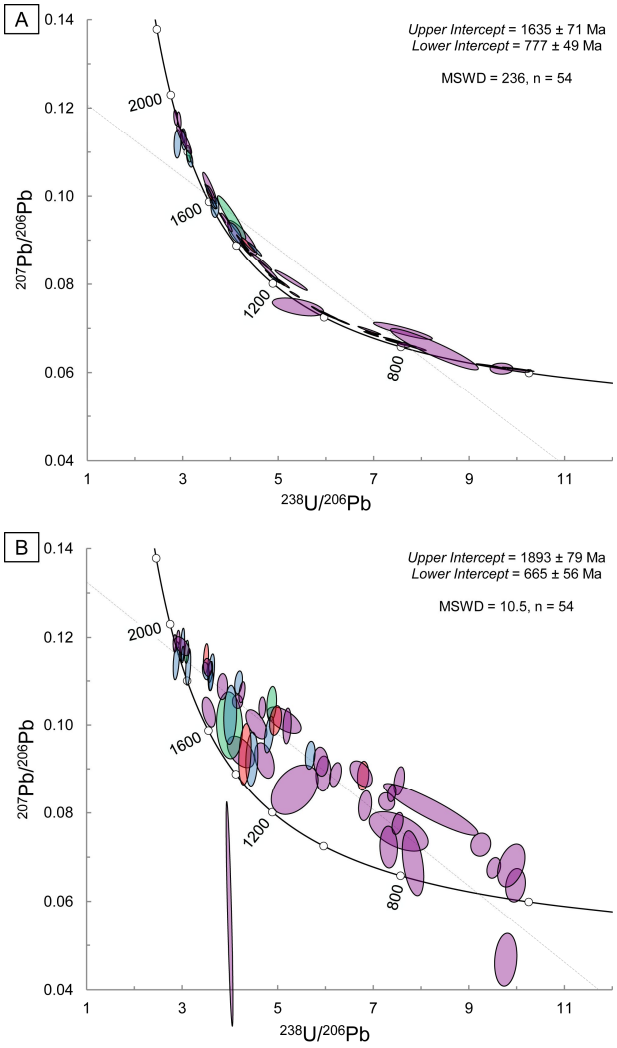

Fig. 11: (A-B) U-Pb Rutile Tera-Wasserburg concordia plots for samples T06-20, T06-21, T06-21A and T06-27. 2σ error ellipses are coloured based on the given sample, where red = T06-20, green = T06-21, blue = T06-21A and purple = T06-27. (A) Concordia excluding inadequate analyses (n = 54) – the same analyses as those in Figure 11b – where these analyses have been subject to a ^{208}Pb correction as outlined by Andersen (2002). (D) Concordia excluding inadequate analyses (n = 54) – the same analyses as those in Figure 11b – where these analyses have been subject to a ^{208}Pb correction as outlined by Chew *et al*., (2014). These figures are explicitly given to illustrate how the data in Figure 11b is altered with the implementation of two different ^{208}Pb correction methods.

4.6. Mineral Equilibria Forward Modelling

Pressure–temperature *(P–T)* pseudosections were calculated for mafic samples T01-40, T06-09 and T06-11, and for metapelitic sample T06-20.

Garnet porphyroblasts in sample T06-20 are very coarse-grained (8–10 mm). Thus, it is reasonable to suspect that garnet core compositions were sufficiently chemically isolated from the bulk-rock composition and did not form part of the peak metamorphic equilibrium bulk composition (Stüwe, 1997). To address this, garnet core compositions were subtracted from the bulk-rock composition to create a matrix-dominated composition prior to calculating the *P–T* pseudosection. Additionally, bulk-rock compositions for all samples were subjected to a Ca concentration correction to account for the presence of apatite in the samples. This adjustment reflects the inability of equilibria models to compute phosphorus-bearing systems.

To account for the two most ambiguous variables relating to a bulk-rock composition, the oxidation state (Fe_2O_3) and the amount of H_2O (Johnson & White, 2011), several equilibria model calculations were undertaken prior to *P–T* modelling. Pressure–composition *(P–X)* pseudosections, where 'X' represents the oxidation state, were calculated for samples T01-40, T06-11 and T06-20 at a constant temperature, in order to constrain the oxidation state of each rock. The oxidation state of T06-09 was constrained through the derivation of Fe^{2+} and Fe^{3+} cation values from wt% oxide values, obtained from electron probe micro analyses of Fe^{3+}-bearing minerals (Droop, 1987). These additional forward modelling results are presented in Appendix 2g. To estimate the H_2O content in mafic samples, the percent of Cl and F in hornblende was subtracted from

whole-rock geochemistry loss of ignition (LOI) values. This method assumes all volatiles reside in hornblende which is a reasonable approximation given hornblende is the only major hydrous mineral in these samples. Additional hydrous minerals such as biotite, staurolite and muscovite are present in sample T06-20. Thus, H_2O content was determined by applying the same method as for the mafic samples, but with the addition of these minerals.

Retrogressed Eclogites: T01-40, T06-09 & T06-11

The Yalumba Hill retrogressed eclogite samples T01-40, T06-09 and T06-11 all contain the inferred peak assemblage: garnet + omphacite + rutile + quartz. There exists some ambiguity regarding the presence of either H_2O or melt at peak metamorphic conditions (addressed in section 5.3). For simplicity's sake, results will be reported with reference to the melt-bearing variant of the peak assemblage. In samples T01-40 and T06-11, the modelled peak assemblage is bound at lower pressure by the appearance of plagioclase, and in sample T06-09, by the appearance of hornblende (Fig. 12, 14, 16; Table 6). These bounds define minimum peak pressure conditions of ca. 15 kbar (T01-40), ca. 18 kbar (T06-09) and ca. 17.5 kbar (T06-11); (Fig. 12, 14, 16; Table 6). In all samples, the peak field extends to higher, unconstrained pressures within the modelled domain.

Peak temperature conditions are constrained using the Zr-in-rutile thermometer; derived strictly from rutile in sample T01-40 (Appendix 2h). Zr-in-rutile thermometry yielded average peak temperatures of 755 °C at 15 kbar for T01-40, 768 °C at 18 kbar for T06-09 and 765 °C at 17.5 kbar for T06-11 (Fig. 12, 14, 16; Table 6). Garnet $X_{(Fe)}$ values in samples T01-40 and T06-09 suggest respective peak temperatures of 775 °C and 790 °C.

The retrograde evolution of the retrogressed eclogites is marked by (i) the appearance of diopside and plagioclase, likely after omphacite (section 5.2), (ii) the appearance of both hornblende and ilmenite, and (iii) the appearance of orthopyroxene in samples T06-09 and T06-11, culminating in a retrograde assemblage consisting of garnet + diopside + hornblende + orthopyroxene + plagioclase + quartz + ilmenite (Fig. 14, 16). Retrograde pressure conditions are constrained at ca. 7–7.5 kbar for T06-11 on the basis of 1–2% orthopyroxene modal proportion contours (Fig. 16, 17c). T06-11 remains unconstrained with respect to its retrograde temperature. Sample T06-09 reached retrograde pressure conditions of ca. 6–9 kbar, corresponding to temperatures of 700–740 °C (derived using the garnet-orthopyroxene Fe–Mg exchange thermometer); (see Appendix 2i); (Fig. 14). It was not possible to compute garnet-orthopyroxene-derived temperature estimates for sample T06-11 due to the retrogressed state of orthopyroxene. A 10% hornblende modal contour in the retrograde field, garnet + diopside + hornblende + plagioclase + quartz + ilmenite is used to mark the retrograde *P–T* conditions for T01-40 (Fig. 12, 13c). These span ca. 8.8–10 kbar and 810–820 °C.

Treating all retrogressed eclogites collectively, a near-isothermal *P–T* path from peak conditions of ca. 15–18 kbar and ca. 755–768 °C to retrograde conditions of ca. 6.5–7 kbar and ca. 800 °C likely passed through the up-temperature titanite-present field as shown by the correlation between current and modelled titanite modal proportions in sample T06-11 (Fig. 16; Table 7).

Modelled mineral modal proportions for all retrogressed eclogites are given in Figures 13, 15 and 17. In all samples, the peak modal proportions of garnet and clinopyroxene are

not preserved, however, peak estimates were derived for samples T01-40 and T06-09 through the summation of mineral modal proportions in both garnet-plagioclase and clinopyroxene-plagioclase reaction textures (Fig. 5b; Appendix 1f, h).

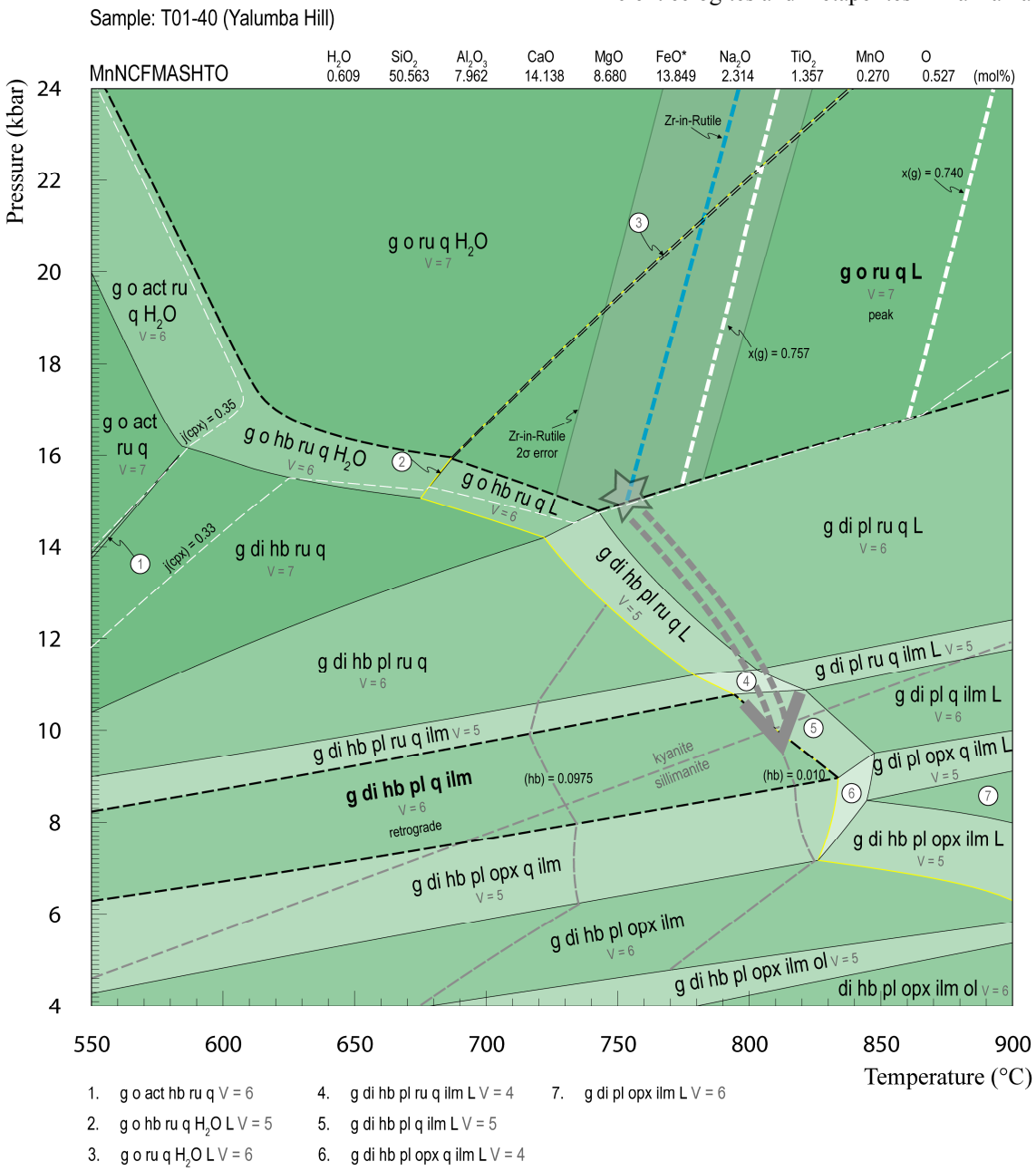

Fig. 12: Calculated *P–T* pseudosection for retrogressed eclogite T01-40, from Yalumba Hill. The inferred peak fields and retrograde field are bordered by bold, dashed black lines and the solidus is represented as a solid yellow line. Values for j(cpx), where j signifies the mount of Na on the clinopyroxene M2 site (as defined in THERMOCALC v.345), are contoured with dashed white lines. Shown with a dashed blue line is the location of the Zr-in-rutile thermometer, constrained from rutile in this sample, and marked with a bold dashed white line for comparison is the location of a garnet near-rim X(Fe) value of 0.757 (labelled as x(g) in diagram) from T01-40 garnet. The location of X(Fe) = 0.740 is also provided to illustrate how such values change with *P-T*. The grey field encompassing the Zr-in-rutile contour denotes the 2σ error accompanying the temperature estimates. A post-peak *P-T* path is illustrated with a grey dashed arrow and terminates in the retrograde field where hornblende mode = 0.10 (grey dashed line). V signifies the variance for each mineral assemblage where V = (components – phases) + 2 and the bulk-rock composition is given in mol%, and here, FeO* = FeO + (2 x 'O'). The full range of modelled mineral modal proportions relevant to this pseudosection are provided in Figure 13. The modelled system used: MnNCFMASHTO is shown above the diagram. Abbreviations: act(actinolite), cpx(clinopyroxene), di(diopside), g(garnet), hb(hornblende), ilm(ilmenite), L(liquid), o(omphacite), ol(olivine), opx(orthopyroxene), pl(plagioclase), q(quartz), ru(rutile).

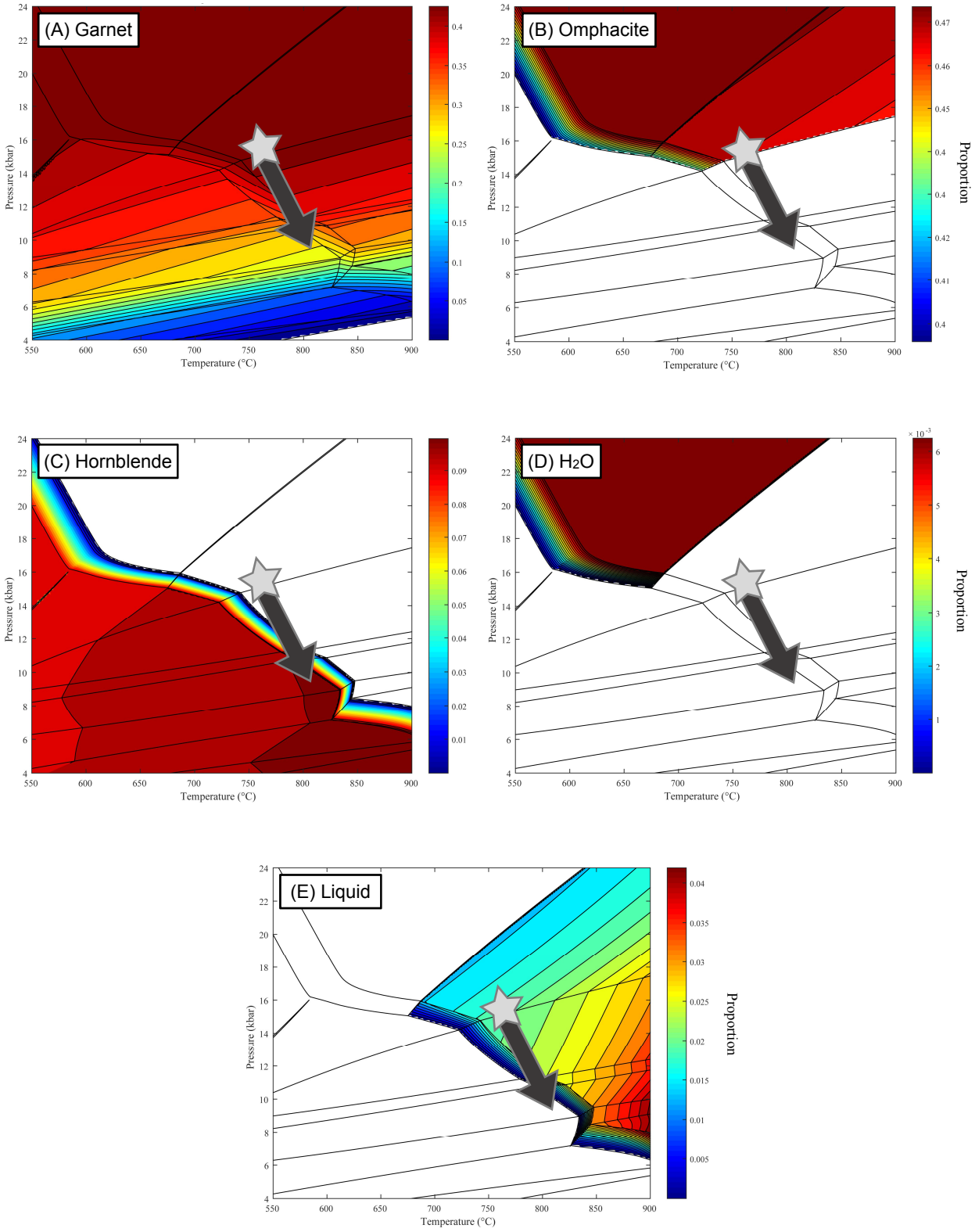

Fig. 13: Sample T01-40: TCI modal proportion outputs for (A) garnet, (B) omphacite, (C) hornblende, (D) H_2O and (E) liquid. Labelled on the vertical axis is pressure, and on the horizontal is temperature. For each phase, 20 contours are drawn across the fields that the given phase occupies. The white region in each diagram represents the fields where the given phase is not stabilised. The light grey star represents the approximate peak conditions for sample T01-40 and the dark grey arrow illustrates the post-peak *P–T* trajectory.

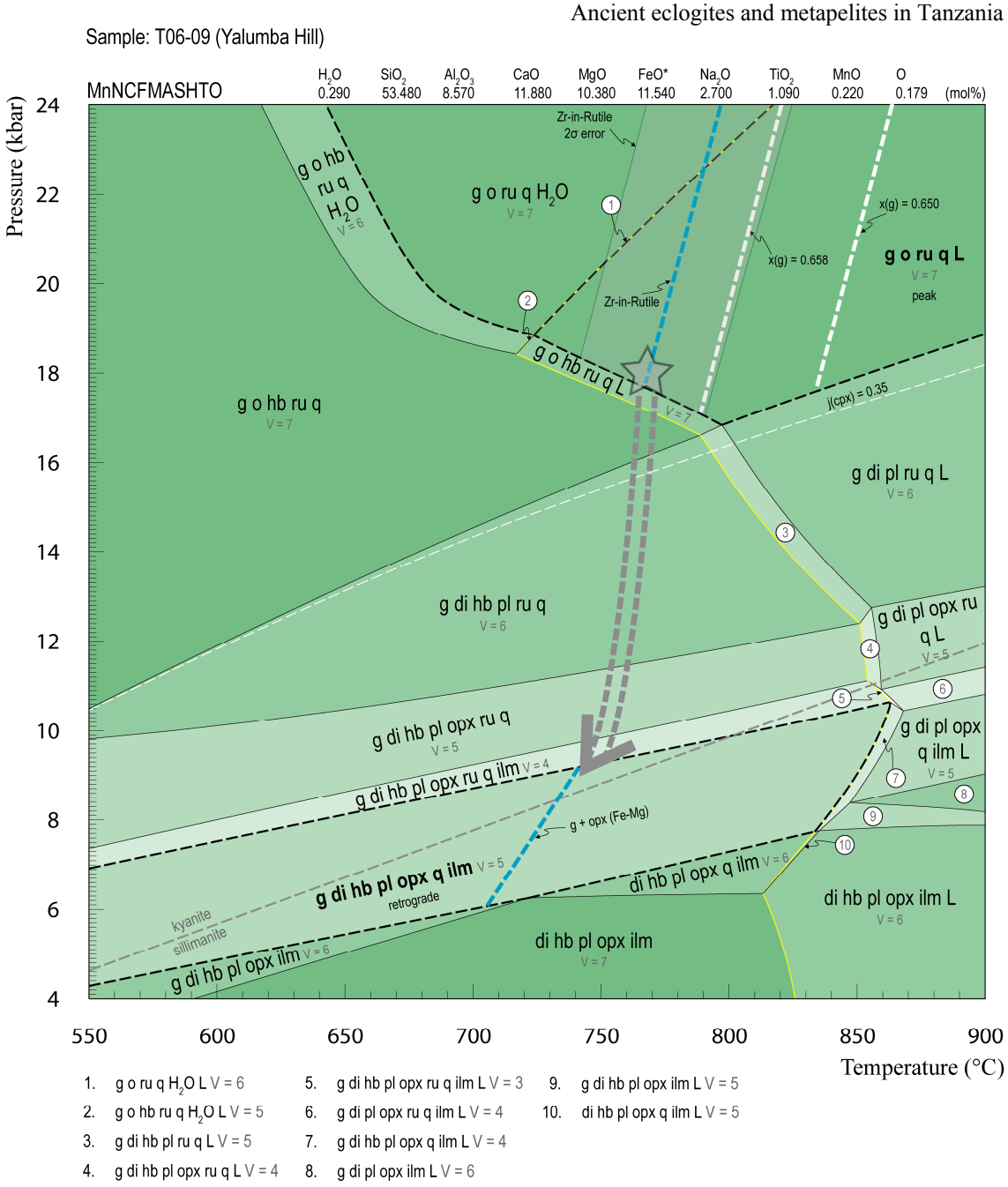

Fig. 14: Calculated *P–T* pseudosection for retrogressed eclogite T06-09, from Yalumba Hill. The inferred peak fields and retrograde field are bordered by bold, dashed black lines and the solidus is represented as a solid yellow line. The white dashed line represents j(cpx) = 0.35 and the bold dashed white line in the peak field is the location of a garnet core X(Fe) value where X(Fe) = 0.658 (labelled as x(g) in diagram) from T06-09 garnet. Additionally, the location of the garnet-orthopyroxene Fe–Mg exchange thermometer is given by the dashed blue line in the retrograde field. A post-peak *P-T* path is illustrated with a grey dashed arrow and terminates in accordance with the location of the garnet-orthopyroxene Fe–Mg exchange thermometer in the retrograde field. The pseudosection is modelled in the MnNCFMASHTO system and the bulk-rock composition is given in mol%. Note: FeO* = FeO + (2 x 'O'). Modelled mineral modal proportions relevant to the minerals in this pseudosection are provided in Figure 15. Abbreviations: cpx(clinopyroxene), di(diopside), ep(epidote), g(garnet), hb(hornblende), ilm(ilmenite), L(liquid), o(omphacite), opx(orthopyroxene), pl(plagioclase), q(quartz), ru(rutile).

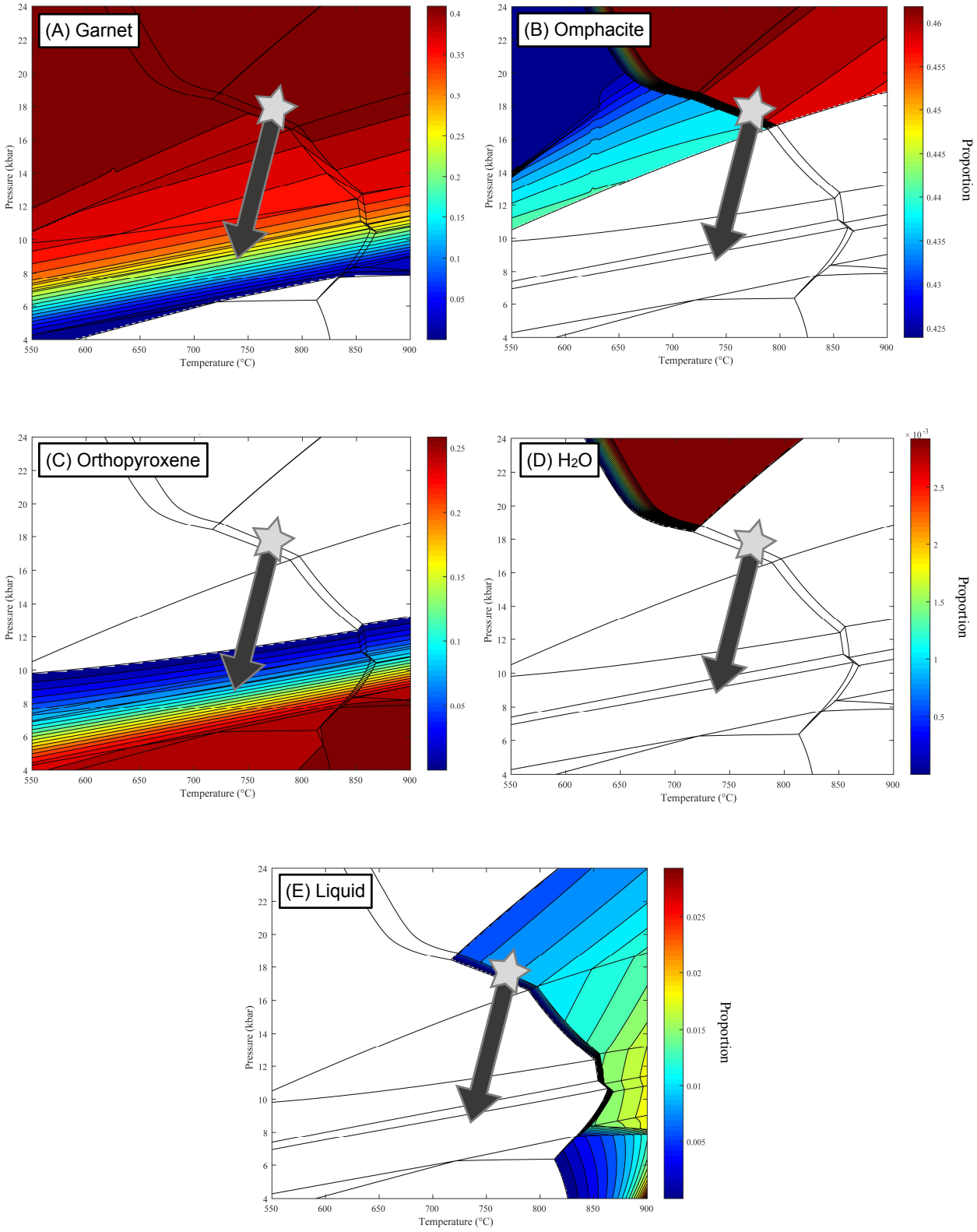

Fig. 15: Sample T06-09: TCI modal proportion outputs for (A) garnet, (B) omphacite, (C) orthopyroxene, (D) H_2O and (E) liquid. Labelled on the vertical axis is pressure, and on the horizontal is temperature. For each phase, 20 contours are drawn across the fields that the given phase occupies. The white region in each diagram represents the fields where a given phase is not stabilised. The light grey star represents the approximate peak conditions for sample T06-09 and the dark grey arrow illustrates the post-peak *P–T* trajectory.

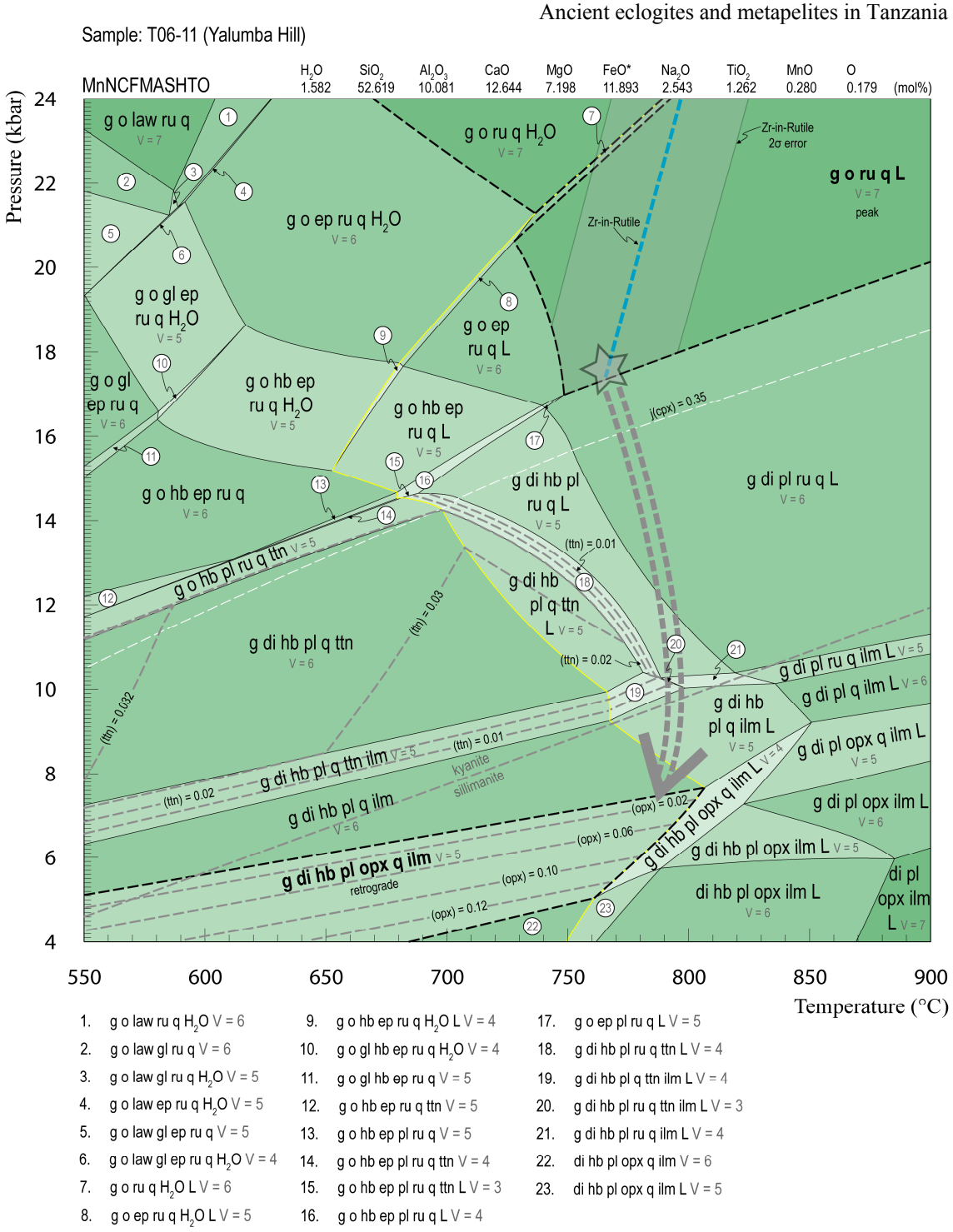

Fig. 16: Calculated *P–T* pseudosection for retrogressed eclogite T06-11, from Yalumba Hill. The inferred peak fields and retrograde field are bordered by bold, dashed black lines and the solidus is represented as a solid yellow line. The white dashed line represents j(cpx) = 0.35. A post-peak *P-T* path is illustrated with a grey dashed arrow. The trajectory of the *P–T* path is constrained using 0.01–0.02 titanite modal proportion contours (grey dashed lines) and the termination of the path is based on orthopyroxene modal proportions of 0.01–0.02 (grey dashed lines). The pseudosection is modelled in the MnNCFMASHTO system and the bulk-rock composition, quoted in mol%, is given above the diagram. Note: FeO* = FeO + (2 x 'O'). Modelled mineral modal proportions relevant to the minerals in this pseudosection are provided in Figure 17. Abbreviations: cpx(clinopyroxene), di(diopside), ep(epidote), g(garnet), gl(glaucophane), hb(hornblende), ilm(ilmenite), L(liquid), law(lawsonite), o(omphacite), opx(orthopyroxene), pl(plagioclase), q(quartz), ru(rutile), ttn(titanite).

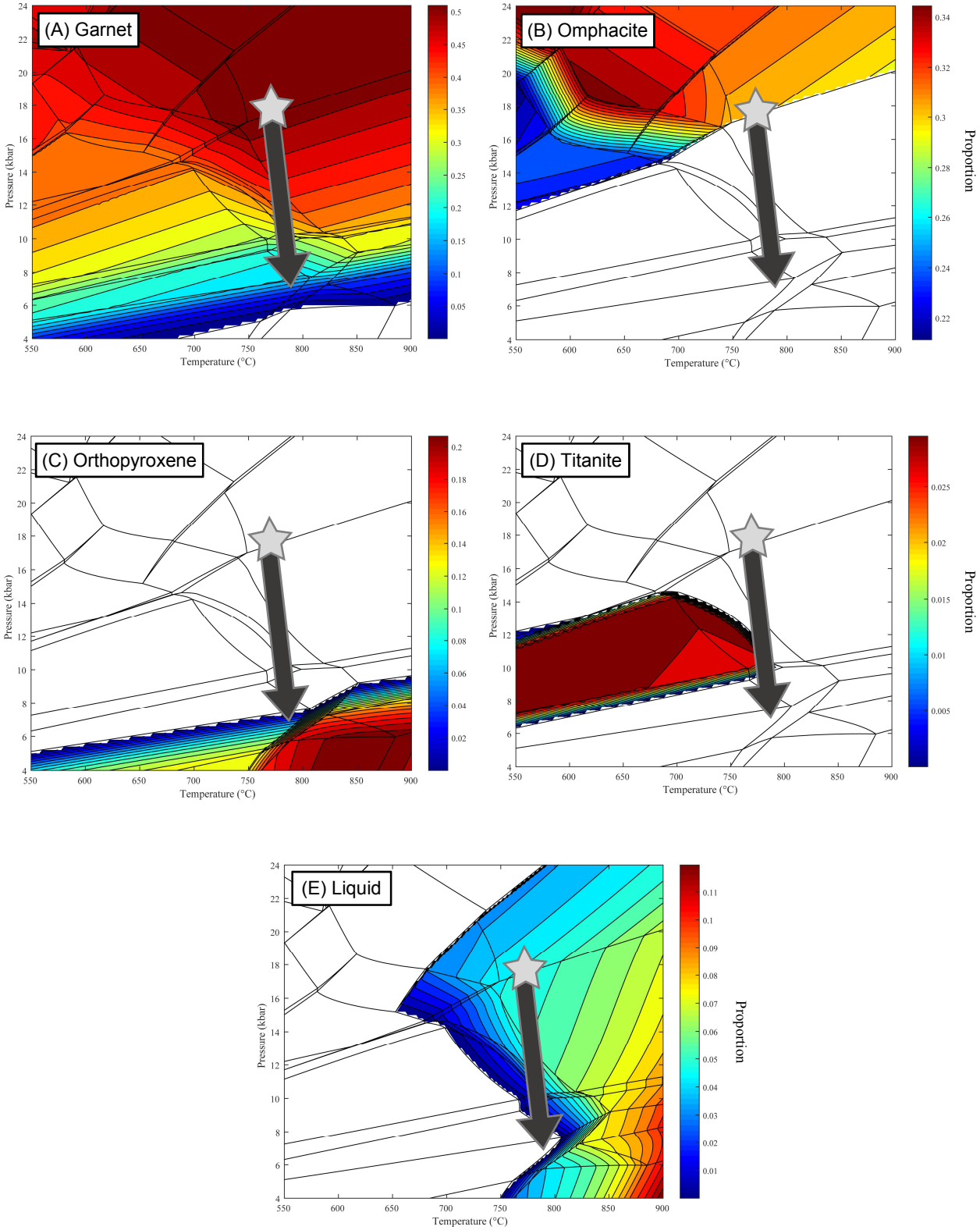

Fig. 17: Sample T06-11: TCI modal proportion outputs for (A) garnet, (B) omphacite, (C) orthopyroxene, (D) titanite, and (E) liquid. Labelled on the vertical axis is pressure, and on the horizontal is temperature. With the exception of titanite (where 10 contours are drawn), 20 contours are drawn over the fields that each phase occupies. The white region in each diagram represents the fields where a given phase is not stabilised. Titanite is included for its role in the determination of the post-peak *P–T* trajectory (grey arrow) for the retrogressed eclogites of Yalumba Hill (see text; Fig. 16).

Metapelitic High-Strain Domain: T06-20

The inferred peak assemblage for T06-20 metapelite comprises kyanite, garnet, biotite, hornblende, quartz, plagioclase and rutile; it is modelled to occur in supra-solidus *P–T* space with limits of 7.3–9.9 kbar and 670–735 °C (Fig. 18). To lower pressure, the peak field limit is marked by the kyanite-sillimanite transition and to higher pressure, the inclusion of muscovite. The disappearance of staurolite serves as the lower temperature constraint and the loss of hornblende marks the higher temperature constraint. The peak temperature is further resolved through the acquisition of Zr-in-rutile average temperature estimates in the inferred peak field, spanning from 718 °C at 8.1 kbar to 722 °C at 9 kbar. The 2σ error inherent in the Zr-in-rutile temperature estimates occupies an area of the peak field that mutually comprises both garnet and hornblende modal proportions (7% and 2%, respectively) which correspond to their respective proportions in the rock (Fig. 18, 19a, b; Table 7). Thus, the peak field is further constrained at 7.3–8.3 kbar and 683–700 °C (Fig. 18).

Though not constrained as well as the peak metamorphic conditions, the retrograde evolution of sample T06-20 is characterised by a near-isobaric *P–T* path that extends into the assemblage comprising garnet, hornblende, kyanite, staurolite, plagioclase, biotite, muscovite, rutile and quartz. The trajectory of the inferred *P–T* path is consistent with increasing modal proportions of hornblende, decreasing proportions of biotite, low proportions of muscovite, increasing proportions of kyanite, and the absence of ilmenite – all of which are inferred from petrological observations (Fig. 18, 19b-e). The proportions of hornblende, kyanite and biotite were selected as retrograde constraints given their sensitivity to *P–T* change in the inferred retrograde field (Fig. 19b-d).

Absent in the modelled retrograde assemblage is chlorite, identified petrographically as a minor post-peak phase in the rock (Fig. 5e). The possible reason for its absence is considered in section 5.3.

Sample: T06-20 (Great Ruaha River)

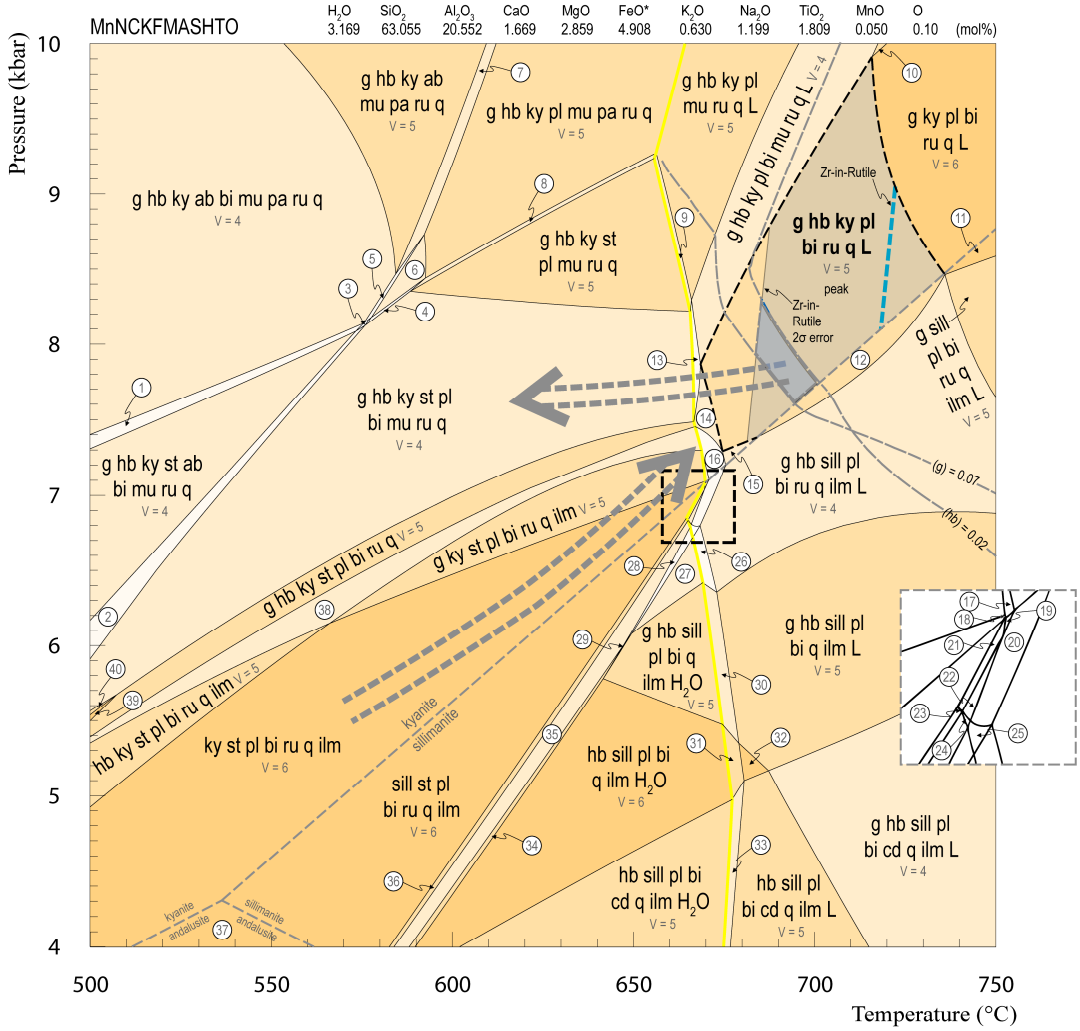

1.	g hb ky st ab bi mu pa ru q V = 3	11.	g sill pl bi ru q L V = 6	21.	sill st pl bi ru q ilm L V = 5	31.	hb sill pl bi q ilm H_2O L V = 5
2.	g hb ky st pl ab bi mu ru q V = 3	12.	g hb sill pl bi ru q L V = 5	22.	hb sill st pl bi ru q ilm L V = 4	32.	hb sill pl bi q ilm L V = 6
3.	g hb ky st pl ab bi mu pa ru q V = 2	13.	g hb ky st pl bi mu ru q L V = 3	23.	sill st pl bi ru q ilm H_2O L V = 4	33.	hb sill pl bi cd q ilm H_2O L V = 4
4.	g hb ky st pl bi mu pa ru q V = 3	14.	g hb ky st pl bi ru q L V = 4	24.	hb sill st pl bi ru q ilm H_2O L V = 3	34.	hb sill st pl bi q ilm H_2O V = 5
5.	g hb ky pl ab bi mu pa ru q V = 3	15.	g hb ky pl bi ru q ilm L V = 4	25.	g hb sill st pl bi ru q ilm H_2O L V = 2	35.	hb sill st pl bi ru q ilm H_2O V = 4
6.	g hb ky pl bi mu pa ru q V = 4	16.	g hb ky st pl bi ru q ilm L V = 3	26.	g hb sill pl bi ru q ilm H_2O L V = 3	36.	sill st pl bi ru q ilm H_2O V = 5
7.	g hb ky pl ab mu pa ru q V = 4	17.	g ky st pl bi ru q ilm L V = 4	27.	g hb sill pl bi ru q ilm H_2O V = 4	37.	and st pl bi ru q ilm V = 6
8.	g hb ky st pl mu pa ru q V = 4	18.	ky st pl bi ru q ilm L V = 5	28.	g hb sill st pl bi ru q ilm H_2O V = 3	38.	g hb ky st pl bi ru q ilm V = 4
9.	g hb ky st pl mu ru q L V = 4	19.	g sill st pl bi ru q ilm L V = 4	29.	g hb sill st pl bi q ilm H_2O V = 4	39.	hb ky st pl bi ru q V = 6
10.	g ky pl bi mu ru q L V = 5	20.	g hb sill st pl bi ru q ilm L V = 3	30.	g hb sill pl bi q ilm H_2O L V = 4	40.	hb ky st pl bi mu ru q V = 5

Fig. 18: Calculated *P–T* pseudosection for metapelite T06-20, from the Great Ruaha River. The inferred peak field is bordered by a bold, dashed black line and the solidus is represented as a yellow line. Zr-in-rutile derived temperature estimates are shown with a dashed blue contour and the grey field encompassing the Zr-in-rutile contour denotes the associated 2σ error. The blue region within the peak field bounded by (i) a garnet mode contour of 0.07 (grey dashed line), (ii) a hornblende mode contour of 0.02 (grey dashed line), (iii) the 2σ lower limit on the Zr-in-rutile thermometer and (iv) the kyanite-sillimanite transition, marks the peak *P–T* window recorded by this rock (see Figure 19 for modal proportions). The near-isobaric post-peak *P–T* trajectory is shown with a grey dashed arrow and is inferred based on hornblende and biotite modal proportions in the retrograde field (see Figure 19; text). A generalised prograde *P–T* path is also shown (see section 5.3). Annotated on the diagram with a grey line is the aluminosilicate transition. The square window with the black border is the location of the inset figure; supplied to capture small fields with respect to the main *P–T* window. V signifies the variance for each mineral assemblage where V = (components – phases) + 2. In the bulk-rock composition, FeO* = FeO + (2 x 'O'). The modelled system used: MnNCKFMASHTO. Abbreviations: ab(albite), and(andalusite), bi(biotite), cd(cordierite), g(garnet), hb(hornblende), ilm(ilmenite), ky(kyanite), L(liquid), mu(muscovite), pa(paragonite), pl(plagioclase), q(quartz), ru(rutile), sill(sillimanite), st(staurolite).

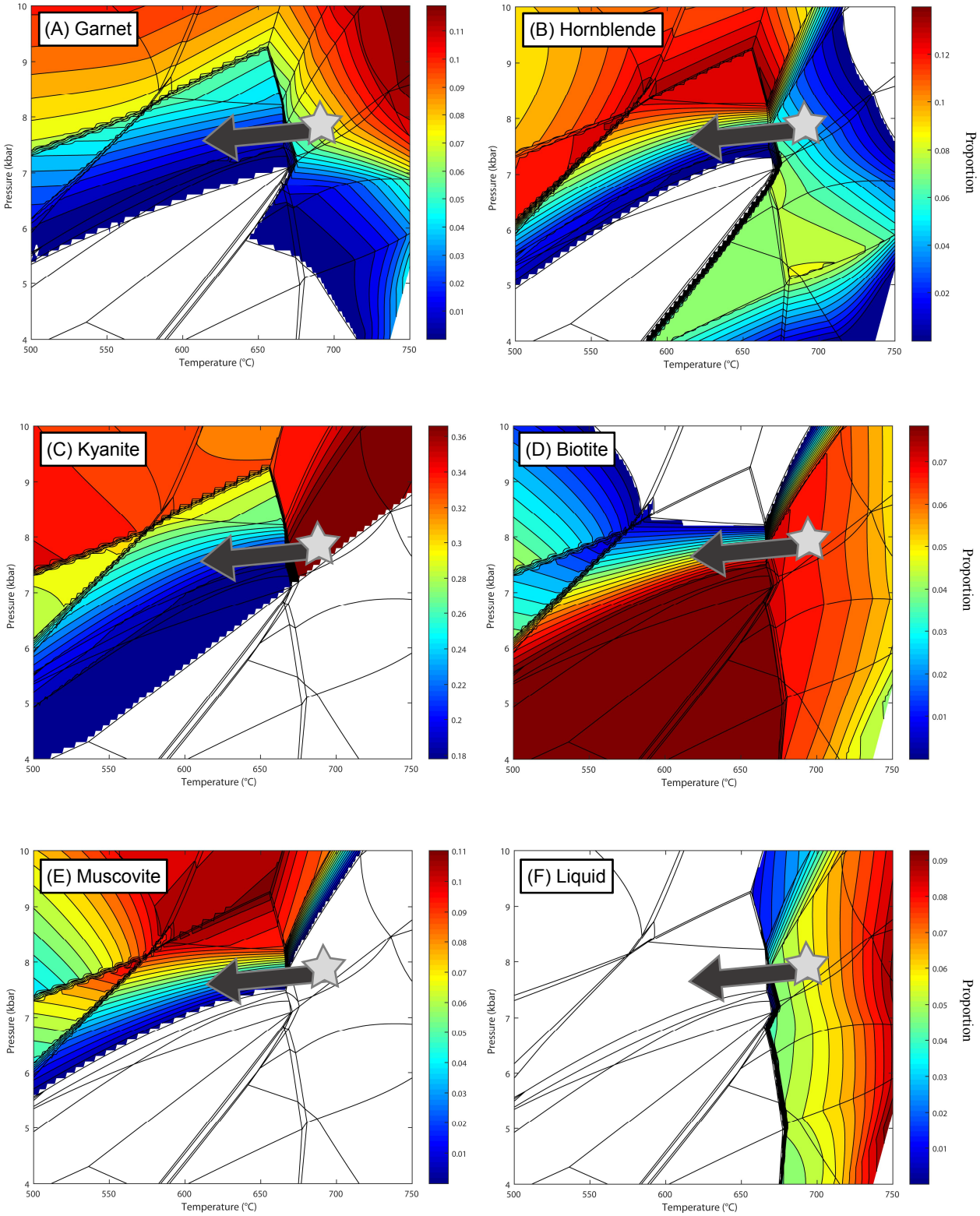

Fig. 19: Sample T06-20: TCI modal proportion outputs for (A) garnet, (B) hornblende, (C) kyanite, (D) biotite, (E) muscovite and (F) liquid. Labelled on the vertical axis is pressure, and on the horizontal is temperature. For each phase, 20 contours are drawn across the fields that the given phase occupies. The white region in each diagram represents the fields where a given phase is not stabilised. Modal proportion contours of (A) garnet and (B) hornblende are especially relevant to the determination of the peak *P–T* conditions for this sample. Useful in constraining the post-peak evolution (grey arrow) are modal contours of (B) hornblende, (C) kyanite, (D) biotite and (E) muscovite (see text; Fig. 18).

Table 6: Summary of *P–T* results for the modelled samples in this study. Outlined are the peak and retrograde *P–T* conditions and the respective determining constraints. Abbreviations are consistent with those described in Figures 12, 14, 16 and 18.

P-T Model	*Peak Pressure (kbar)*	*Pressure Constraints*	*Peak Temperature (°C)*	*Temperature Constraints*	*Retrograde Pressure (kbar)*	*Pressure Constraints*	*Retrograde Temperature (°C)*	*Temperature Constraints*
T01-40	15 (minimum)	pl-in (down pressure)	755 775	Zr-in-rutile X(Fe)-in-garnet	8.8–10	ru-out (down pressure) (hb) = 0.10	810–820	(hb) = 0.10
T06-09	18 (minimum)	hb-in (down pressure)	768 790	Zr-in-rutile (derived from T01-40) X(Fe)-in-garnet	6–9	opx-in (down pressure)	700–720	gt-opx (Fe–Mg)
T06-11	17.5 (minimum)	pl-in (down pressure)	765	Zr-in-rutile (derived from T01-40)	7–7.5	opx-in (down pressure) (opx) = 0.01, 0.02	-	-
T06-20	8.3 7.3	(hb) = 0.02, Zr-in-rutile* (g) = 0.07, ky-sill	683 700	(g) = 0.02, Zr-in-rutile* (hb) = 0.02, ky-sill	-	-	-	-

Table 7: Mineral modal proportion estimates (quoted in volume%) used to constrain *P–T* conditions for all modelled samples. Estimates are derived from both thin-section and MLA images (see Appendix 1f). Reintegrated peak mineral abundances are provided for samples T01-40 and T06-09 and the corresponding methodology is provided in Appendix 1f, h. Peak mineral modes are not provided for sample T06-11 due to partial post-peak retrogression in this sample and the presence of a pervasive fine-grained mineral fabric. The abundance of garnet shown for sample T06-20 is representative of the garnet rims as cores were excluded for calculation purposes (see Appendix 1c). Mineral abbreviations are consistent with those outlined in the petrography section.

Sample	*Peak*								*Retrograde*														
	grt	omp	qz	rt	pl	hbl	ky	bt	grt	di	qz	rt	pl	hbl	opx	ilm	ttn	ap	ky	bt	mu	chl	st
T01-40	41	51	5	3					20	34	6	<1	25	10		2	<1	<1					
T06-11									18	52	6	<1	15	5	1	3	<1						
T06-09	33	62	4	1					9.5	22.5	3	<1	53	8	1	3							
T06-20	7.5		32	1	28	2	20	8	7.5		32	1	28	2				<1	20	8	<1	<1	1

5. DISCUSSION

5.1. Timing of Metamorphism: High-Strain Metapelites

Geochronological constraints on the peak metamorphic event associated with the formation of the high-strain metapelitic domains in the Usagaran Orogen are sparse in the literature. This forms the primary reason to undertake U–Pb rutile geochronology on the metapelites in this study.

Rutile grains armoured inside garnet rims in metapelitic samples were selected for in-situ LA–ICP–MS U–Pb analysis. Rutile grains at garnet rims were selected due to the preservation of major element growth zonation in T06-20 garnet (Fig. 6e), indicating that garnet rims formed during peak metamorphism.

The retained analyses (n = 54) from the original dataset (n = 61) all showed evidence of lead loss, the presence of ^{232}Th, and a common lead (^{208}Pb) contamination signature (Fig. 10b). Dunkl and von Eynatten (2009) showed that it is possible for rutile to incorporate non-trivial quantities of ^{232}Th, and the analysed rutiles in this study are no exception (Appendix 2f). The two approaches used to correct for ^{208}Pb – the Andersen (2002) correction method, and the correction method outlined by Chew *et al*. (2014) – were unsuccessful (Fig. 11). Both methods assume a single common lead accumulation event at a user-specified time, and further, the Andersen Routine method assumes all ^{208}Pb is non-radiogenic (see Appendix 1b for detailed descriptions). The failure of these methods to correct for ^{208}Pb is attributed to a system whereby radiogenic lead has been progressively lost (this challenges the assumption that lead uptake occurred at a set moment in time), ^{232}Th is present (this challenges the assumption that all ^{208}Pb is non-

radiogenic), and there are low ^{238}U concentrations (it is reasonable to suggest that analyses exhibiting a ^{208}Pb signature only do so because of their deficiency in ^{238}U). In light of the above inferences, the uncorrected U–Pb rutile data (Fig. 10b, c) is reasoned to be more useful than the corrected data. Consequently, an upper intercept age of 1985 ± 23 Ma (Fig. 10c) is interpreted to date the timing of peak metamorphism for the high-strain metapelitic domains enclosing the retrogressed eclogites. Although this age is constrained using a limited number of analyses (n = 9), it falls within error of a published age of 1999.1 ± 1.1 Ma from the retrogressed eclogite sample T01-40 – this study (Collins *et al*., 2004). The upper intercept age is also within error of a U–Pb monazite age of 1999.5 ± 1.4 Ma (Möller *et al*., 1995) from a metapelitic sample from the same high-strain zone that wraps the eclogite-bearing domains. The overlap in ages suggests that peak metamorphism associated with the formation of the Usagaran metapelites and mafic rocks was coeval.

A lower intercept age for the uncorrected rutile data is constrained at 551 ± 33 Ma. This age falls close to the 655–610 Ma age range associated with the development of the East-African Orogen (Möller *et al*., 2000; Muhongo *et al*., 2001; Sommer *et al*., 2003; Fritz *et al*., 2013), and also lies within error of a lower intercept U–Pb rutile age of 501 ± 26 Ma (Möller *et al*., 1995).

5.2. Eclogite-Facies Metamorphism: The Evidence

Möller (1995) argued on the basis of a single omphacite inclusion in garnet that the mafic domains preserved at Yalumba Hill represent relic eclogite-facies rocks. Not only was this argument based on the occurrence of just one inclusion, it is also unclear whether the

supposed inclusion was truly armoured within garnet. Because of this ambiguity, and because such a claim has significant implications for the *P–T* status of these ancient rocks, it is considered worthwhile to investigate the case for eclogite-facies metamorphism in the Usagaran Orogen.

The retrogressed eclogite samples preserve well-developed diopside-plagioclase symplectite textures (Fig. 5b; Appendix 2a). These define subhedral to euhedral crystallographic habits, suggesting they have replaced a pre-existing mineral. Petrological evidence of this sort has long been used as a qualitative justification for prior eclogite-facies conditions (Eskola, 1921; Vogel, 1966; Jamtveit, 1987; Peacock & Goodge, 1995; Lombardo & Rolfo, 2000; Chu *et al*., 2016; Loose & Schenk, 2018) and moreover, it is widely accepted that such textures develop during the post-peak isochemical decompression after omphacite (Vogel, 1966; Abbott & Greenwood, 2001; Anderson & Moecher, 2007). Given the assumption of a closed chemical system (i.e. the redistribution of the entire sodium reservoir residing in omphacite at peak conditions into diopside and plagioclase symplectite), the reintegration of a former omphacite composition is often accomplished through the sole consideration of symplectic diopside and plagioclase compositions. It is therefore interpreted that such textures present in the relic eclogites reflect the former presence of omphacite at peak metamorphic conditions. This supports the former establishment of eclogite-facies conditions characterised by the peak assemblage: garnet + omphacite + rutile + quartz, in all samples.

The assumption that post-peak decompression after omphacite to produce diopside-plagioclase intergrowths is isochemical is not without uncertainty (Mysen & Griffin,

1973; Heinrich, 1982). In the Usagaran retrogressed eclogites, sodium-bearing tschermakitic amphibole overprints matrix and symplectic diopside (Fig. 5b), thereby casting uncertainty on the possibility that decompression in this case was isochemical in nature. Thus, the reintegration of a former peak omphacite composition cannot be accomplished on the basis of current symplectic diopside and plagioclase compositions alone. To partially address this, a comparatively macroscale approach was implemented for sample T01-40 that considers the whole-rock sodium content in the reintegration procedure as opposed the potentially unrepresentative sodium concentrations of diopside and plagioclase.

The composition of a former clinopyroxene was determined by assuming that the total concentration of Na_2O in the bulk-rock geochemistry for sample T01-40 had previously resided in a precursor clinopyroxene phase at peak metamorphic conditions (see Appendix 1h for extended methadology). Clinopyroxene was estimated to contain 4.48 wt% Na_2O based on the bulk-rock sodium oxide concentration and reintegrated peak mineral modal proportions. Using the estimated clinopyroxene sodium oxide component in T01-40, coupled with EPMA-derived clinopyroxene oxide compositions (Appendix 2k), 15 reintegrated omphacitic compositions were derived, as shown by respective $X_{(jad)}$ values for the compositions ranging from 0.3 to 0.315 – these markedly higher than the $X_{(jad)}$ values in present clinopyroxene in sample T01-40 (Table 4). Conclusions such as these provide quantitative evidence for the occurrence of former omphacite.

5.3. Pressure–Temperature Evolution of the Usagaran Belt

Retrogressed Eclogites: T01-40, T06-09 & T06-11

The interpretation that the eclogites share the peak assemblage garnet + omphacite + rutile + quartz is based upon petrological evidence and information revealed from mineral chemistries. The preservation of diopside-plagioclase symplectite textures (Fig. 5b) – and the compositional reintegration to a former omphacitic clinopyroxene composition (section 5.2) – support the former presence of peak omphacite, inclusions of rutile in garnet (Fig. 5a) support the presence of peak rutile, and the preservation of garnet growth zonation (Fig. 6a) supports the presence of peak garnet. The peak assemblage is successfully stabilised in all mineral equilibria models with the addition of either H_2O or melt (Fig. 12, 14, 16). The stabilisation of free H_2O in the subsolidus region of the modelled space may reflect either (i) the legitimate presence of free H_2O or – in part – ii) the lack of mineral *a–x* models that incorporate mineral-bound H_2O into nominally anhydrous minerals such as omphacite (Green *et al*., 2016). Implicit in the latter is the assumption that H_2O was structurally bound in former peak omphacite. Several studies have addressed omphacite's importance as a carrier of H_2O at high-pressure conditions (Smyth *et al*., 1991; Katayama & Nakashima, 2003; Bromiley & Kepler, 2004; Sheng & Gong, 2017). The observation that hornblende overprints symplectic diopside (Fig. 5b; Appendix 2a) demonstrates that H_2O was derived from a former phase, potentially supporting a peak metamorphic regime characterised by the residence of a proportion of H_2O in omphacite.

Temperature estimates derived from Zr-in-rutile, however, plot in the melt-bearing variant of the modelled peak assemblage (Fig. 12, 14, 16). Thus, the interpretation that

melt was present at peak conditions, as opposed to H_2O, is favoured. The absence of petrographical evidence for partial melting in all retrogressed eclogite samples (section 4.2; Fig. 5a-c) may be explained by the low predicted melt fractions in the regions of modelled *P–T* space where peak conditions are inferred (section 4.6; Fig. 12, 14, 16). Melt volume fractions are ca. 2% in T01-40 (Fig.13e), ca. 1% in T06-09 (Fig. 15e) and ca. 5% in T06-11 (Fig. 17e). These melt fractions are unlikely to constitute any significant petrological expression in the samples.

The eclogites experienced minimum peak *P–T* conditions of ca. 755 °C and 15 kbar (T01-40), ca. 768 °C and 18 kbar (T06-09), and ca. 765 °C and 17.5 kbar (T06-11); calculated from mineral equilibria forward modelling and Zr-in-rutile thermometry. The calculated peak metamorphic conditions correspond to respective minimum geothermal gradients of 500 °C/GPa, 430 °C/GPa and 440 °C/GPa, equating to an average geotherm of 460 °C/GPa. Thus, the results demonstrated here support a geodynamic regime characterised by subduction (Brown, 2001, 2006, 2014). The collective retrograde evolution of the eclogites is defined by near-isothermal post-peak decompression through granulite-facies conditions of ca. 6.5–7 kbar and ca. 800 °C. The application of the garnet-orthopyroxene thermometer in sample T06-09 to constrain retrograde temperatures assumes garnet rims and matrix orthopyroxene were in equilibrium. Given the preservation of secondary orthopyroxene adjacent to garnet (Fig. 5c; Appendix 2a), and the clear compositional resetting at garnet rims (Fig. 6e), the use of the orthopyroxene thermometer is considered reasonable. However, it may be possible that orthopyroxene – given its comparatively fine-grained textural nature – yields minimum temperatures for its growth. This may

explain why the post-peak *P–T* path for T06-09 extends to cooler temperatures than those inferred from mineral modes from samples T01-40 and T06-11.

The calculated *P–T* conditions broadly agree with published conventional thermobarometric results of 18 kbar and 750 °C (peak) and 9–10 kbar and 665–780 °C (retrograde; Möller *et al*., 1995). Mineral equilibria forward modelling predicts the establishment of slightly higher peak temperatures than those derived by Möller *et al*. (1995) and suggests the decompression history of the eclogites extends to lower pressures.

Metapelitic High-Strain Domain: T06-20

The generalised prograde *P–T* history attributed to T06-20 metapelite is one that likely passed through the comparatively low-pressure assemblage: kyanite, garnet, biotite, staurolite, plagioclase, rutile and ilmenite (Fig. 18), given the absence of hornblende inclusions within garnet and the preservation of biotite, staurolite, plagioclase and rutile inclusions within garnet and kyanite (section 4.2; Fig. 5d, e). T06-20 contains the inferred peak assemblage kyanite + garnet + biotite + hornblende + quartz + plagioclase + rutile. The garnet core composition in T06-20 garnet was removed from the bulk-rock composition prior to mineral equilibria modelling. The prominent growth zonation preserved in coarse-grained T06-20 garnet (Fig. 6d, 7d) supports a former chemical system where the garnet core was not in equilibrium with the remaining rock volume (Stüwe, 1997; Marmo *et al*., 2002).

The high-strain metapelite T06-20 reached peak *P–T* conditions of 7.3–8.3 kbar and 683–700 °C (Fig. 18; Table 7), consistent with upper amphibolite-facies conditions. The inferred peak *P–T* region in the modelled peak field (Fig. 18) comprises melt in proportions of 5–6% (Fig. 19e). As with the relic eclogite samples, the presence of such a low melt fraction at peak conditions is unlikely to have any effect on the preserved bulk-rock composition (White & Powell, 2002; Rosenberg & Handy, 2005). A near-isobaric post-peak *P–T* path extends into the field marked by the addition of staurolite and muscovite, and the loss of melt (Fig. 18). Petrological observations such as secondary muscovite in low proportions (Fig. 5e), late staurolite (Fig. 5e), the absence of ilmenite, and increasing kyanite are all consistent with the inferred retrograde evolution. Although chlorite has been petrographically interpreted as a minor phase (<1% proportion), its absence in the *P–T* pseudosection is possibly a result of the low quantity of bulk-rock H_2O used in the calculations (Fig. 18).

A hornblende- and staurolite-absent metapelite collected from the same area yielded interpreted peak *P–T* conditions of 11.7–12.5 kbar and 610–670 °C based on mineral composition thermobarometry (Brick, 2011). Insofar as T06-20 metapelite and this sample can be considered broadly equivalent, despite their petrographical differences, the results demonstrated in this study (through a more robust method) indicate that the high-strain fabrics reached lower peak *P–T* conditions than previously thought (Möller *et al*., 1995; Brick, 2011).

5.4. Geodynamics of the Usagaran Belt

The tectonometamorphic evolution of the Usagaran Belt is complex, as demonstrated by its proposed structural evolution (Reddy *et al*., 2003; Collins *et al*., 2004). However, in describing its evolution, a simplification has been consistently suggested – this is that the retrogressed eclogites and the comparatively high-strain domains shared a mutual tectonometamorphic history. The *P–T* results obtained in this study are inconsistent with this model.

Mineral equilibria forward modelling suggests that the eclogites preserved at Yalumba Hill reached eclogite-facies conditions of 15–18 kbar and 755–768 °C, along low geothermal gradients consistent with a subduction regime. The high-pressure conditions were transient and were immediately followed by isothermal decompression. This notion is supported by geochronological evidence from Collins *et al*., (2004) consistent with the establishment of peak metamorphic conditions at ca. 2000 Ma, and subsequent low-pressure conditions at ca. 1991 Ma.

The rapid exhumation of the eclogite-facies rocks as outlined by Collins *et al*. (2004), is supported by the preservation of growth zonation in T01-40 garnet (Fig. 6a). Considering the size of garnets in T01-40, prograde compositional zonation would be erased if the rocks resided at similar temperatures corresponding to those at peak conditions (Caddick *et al*., 2010). In support of this are the high temperatures derived from Zr-in-rutile thermometry (Appendix 2h). Cherniak *et al*. (2007) showed that rutile grains ≤ 100 μm in diameter will not retain their Zr concentrations at high temperatures of ca. 760 °C if the cooling rate is ≥ ca. 100 °C/Ma. Given that almost all analysed rutile grains in T01-

40 were less than 100 μm in diameter, this effectively limits the duration of high-temperature conditions to ca. 500,000 years.

In further support of a rapid post-peak decompression and cooling history for the eclogite-facies rocks, the light and heavy rare-earth element (REE) distributions in T01-40 garnet show evidence for the preservation of growth zonation, strongly resembling Rayleigh fractionation during garnet growth (Fig. 8a, b; Otamendi *et al*., 2002. The preservation of REE growth zonation is suggestive of a post-peak *P–T* history operating on sufficiently short timescales to ensure the compositional gradients in garnet were not thermally relaxed (e.g. Tucker *et al*., 2015).

In contrast to the retrogressed eclogites, mineral equilibria forward modelling combined with evidence from well-preserved petrological relationships suggests the protoliths to the metapelitic high-strain domains reached upper amphibolite-facies conditions of 7.3–8.3 kbar and 683–700 °C during a barrovian-style prograde evolution. There is no evidence that the high-strain metapelites experienced high-pressure conditions.

The Isimani retrogressed eclogites experienced rapid near-isothermal decompression from high-pressure conditions. The interpretation that the eclogite-facies rocks experienced a short-lived peak to post-peak *P–T* history is only conceivable in a tectonic system that promotes rapid exhumation. Although Reddy *et al*., (2003) argued that transpression was responsible for the exhumation of the entire Isimani Suite, the lineation geometries preserved in the high-strain Isimani domains are shallowly plunging on gently to moderately dipping foliations; a structural feature that is also common in extensional

or transtentional systems (Dewey, 2002). To account for the rapid exhumation history of the eclogite-facies rocks and the contrasting *P–T* histories recorded by the eclogites and the high-strain gneisses, an exhumation model is proposed that appeals to extrusion-based tectonics, rather than contraction.

It is envisaged that the margin of the Tanzania Craton was subducted during the Palaeoproterozoic. This is supported by εNd data and Lu–Hf in zircon indicating that the ca. 2000 Ma Usagaran eclogitic domains are comparatively evolved (Lau, 2009; Brick, 2011). Following transient high-pressure peak metamorphism, the eclogites were exhumed to pressures of 6.5–7 kbar and were tectonically intercalated with the upper amphibolite-facies high-strain Isimani gneisses at mid-crustal depths by ca. 1991 ± 2 Ma (Fig. 20; Collins *et al*., 2004).

Most workers agree that thrust-related processes will not exhume rocks from mantle depths (Hacker & Gerya, 2013). An alternative is buoyancy-driven exhumation that acts on its own or is augmented by upper plate extension (e.g. Burov *et al*., 2001; Anderson *et al*., 1991). This mechanism for the exhumation of the eclogite-facies rocks is best described by the process of 'eduction' (Fig. 21; Andersen *et al*., 1991; Duretz *et al*., 2012; Petersen & Buck, 2015) – the buoyancy-driven motion of subducted material following slab breakoff. Such a mechanism has been interrogated using 2-D numerical thermomechanical models (Duretz *et al*., 2012; Duretz & Gerya, 2013; Petersen & Buck, 2015). Petersen and Buck (2015) demonstrate that eduction may arise spontaneously from a prior collisional regime and can exhume continental material within a time-span of 5 Myr. Following slab breakoff, the comparatively rigid, shallower material is buoyantly

exhumed (Hacker & Gerya, 2013). The buoyant rise of material creates an effective wedge whose upper surface expresses kinematic indicators consistent with an extensional detachment, and whose lower surface is kinematically a thrust. The buoyancy differential of the exhuming high-pressure rocks decreases, thereby promoting their increasing propensity to become structurally coupled to the enclosing, lower pressure rocks. The structural coupling described in the model is recorded at the point where the *P–T* histories of the contrasting Usagaran rock packages become broadly coincident (Fig. 20, 21). This point is established at pressures of 6.5–7 kbar, corresponding to depths of ca. 23–25 km, with the slightly higher temperatures recorded by the retrogressed eclogites conceivably reflecting the residual heat from their higher temperature evolution.

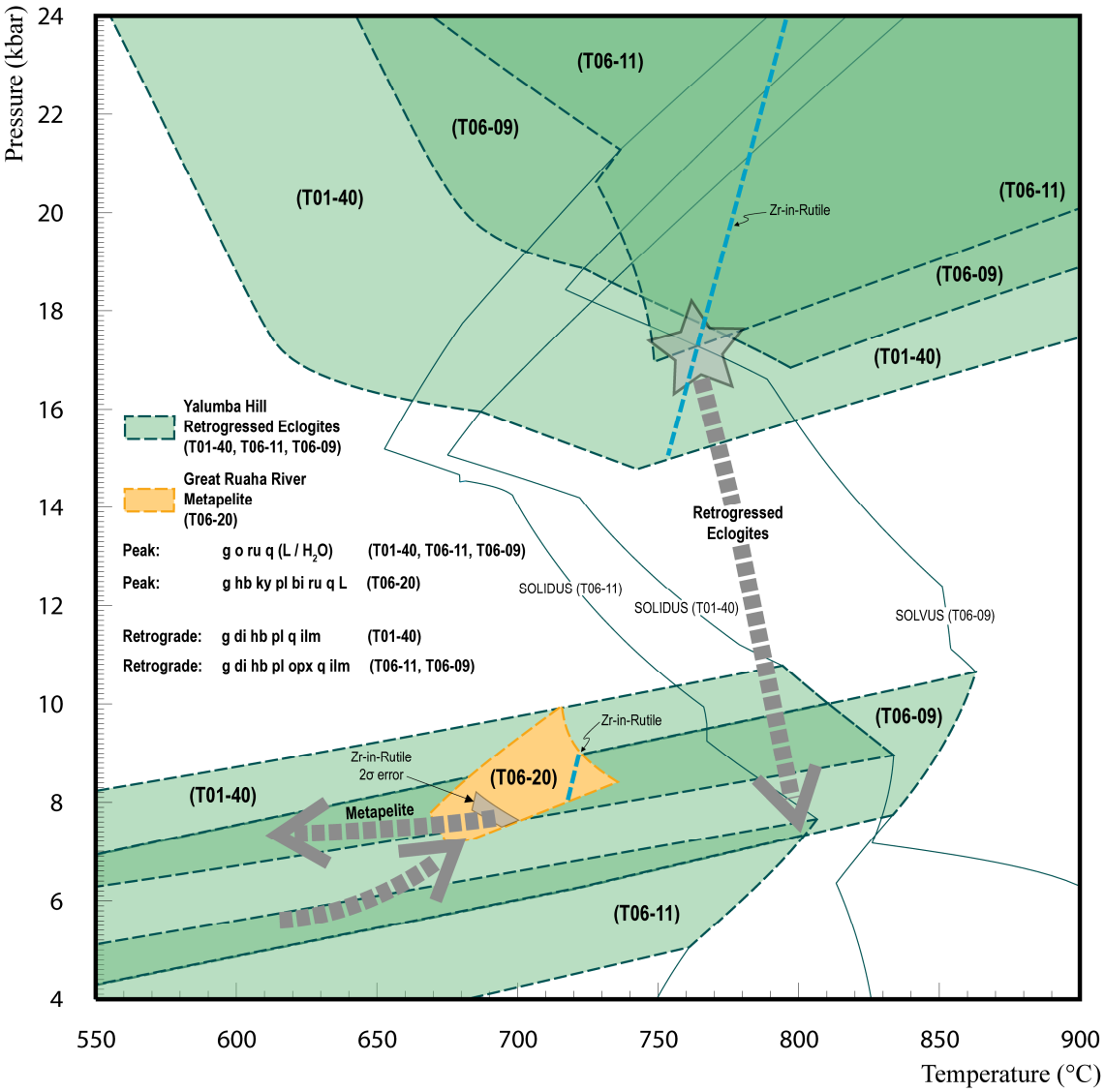

Fig. 20: Summary *P–T* pseudosection for all modelled samples in this study. Overlapping green fields, bordered by green dashed lines, mark the peak and retrograde fields for the three Yalumba Hill retrogressed eclogites (T01-40, T06-09, T06-11; see Figures 12, 14, 16). The yellow field bordered by the orange line represents the peak field for the Great Ruaha River metapelite (T06-20) and the grey region within this field marks the constrained peak *P–T* window for this sample (based on further constraints – see text; Figure 18). The solidus for each Yalumba Hill sample is represented with thin, solid green lines. The primary temperature constraint for all samples, the Zr-in-rutile thermometer, is shown as an annotated dashed blue line. Two schematic *P–T* paths are drawn: one depicting the peak to retrograde *P–T* evolution of the retrogressed eclogites, the other depicting the evolution of the high-strain metapelite, from generalised prograde conditions, through peak conditions, to post-peak metamorphic conditions. The eclogite *P–T* path is inferred based on the juxtaposition of the respective *P–T* pseudosections for the three samples (Figure 12, 14, 16), and its trajectory is further constrained based on both titanite and orthopyroxene modal proportions in sample T06-11 (see text; Figure 16, 17; Table. 7). For metapelite T06-20, the same *P-T* trajectory as seen in Figure 18 is given here, albeit with size adjustments to reflect the changed scale. The termination of the retrogressed eclogite post-peak *P–T* path, coinciding reasonably well with the peak metamorphic window experienced by the metapelite, is supportive of a subduction geodynamic regime characterised by the structural juxtaposition of the eclogite-facies rocks with the Ruaha River high-strain domains during the ongoing, rapid exhumation of the eclogites.

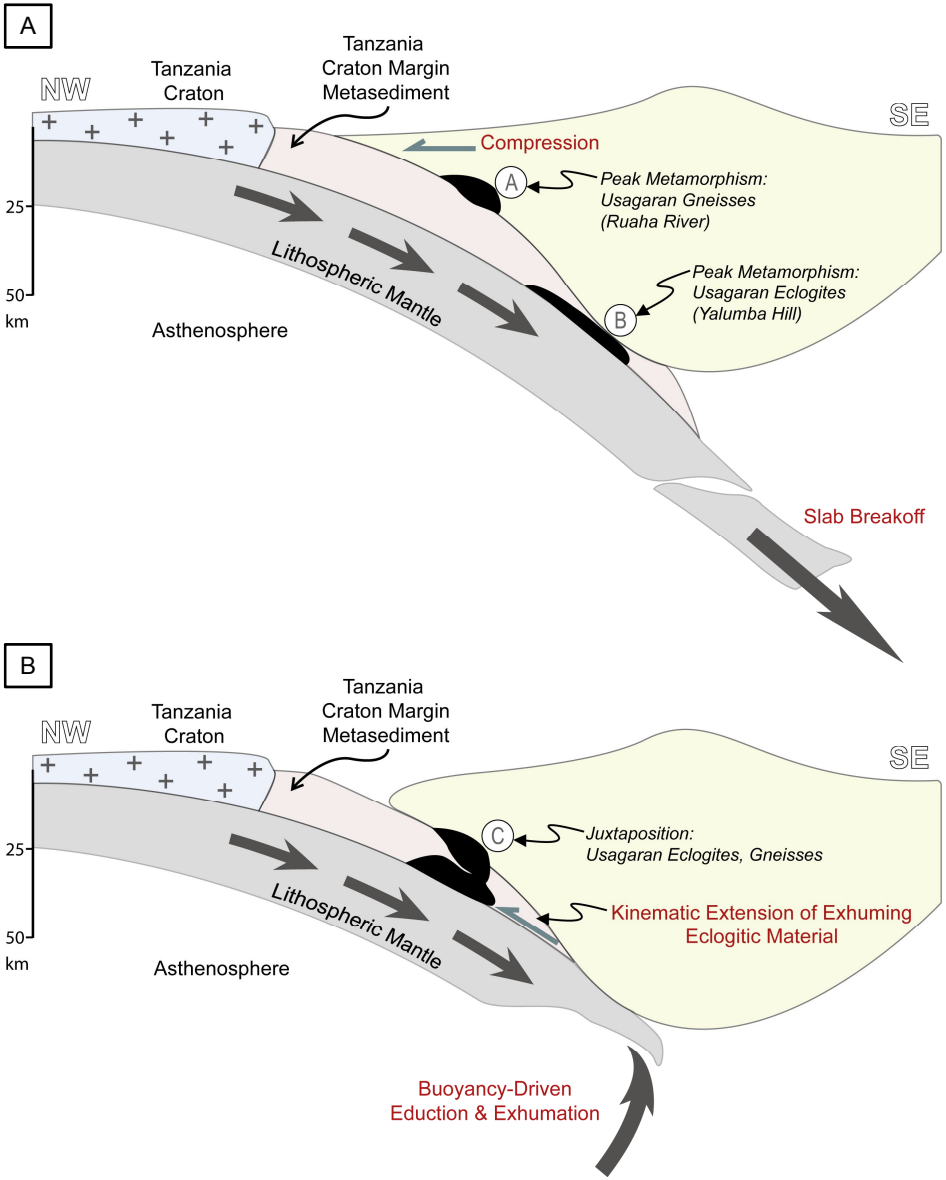

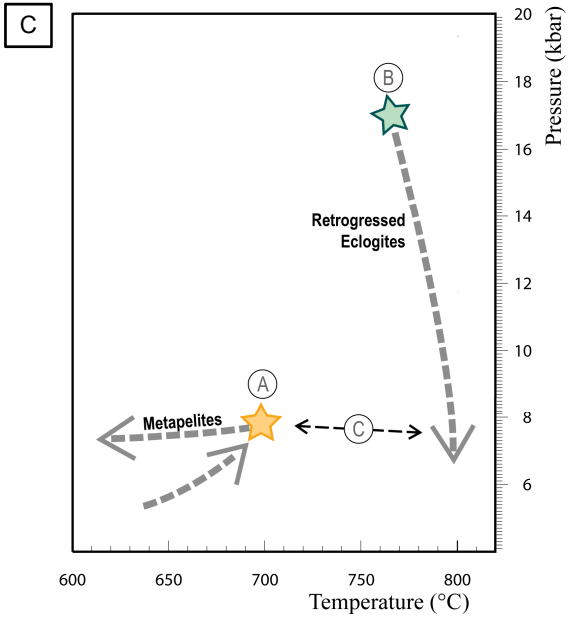

Fig. 21: Schematic illustration of the proposed geodynamic regime for the Usagaran Belt in the Palaeoproterozoic. (A) Schematic cross-section of a continental margin inferred to be apparent in Tanzania in the Palaeoproterozoic. The margin of the Tanzania Craton, comprising primarily sedimentary material and some mafic material, was subducted – the orientation of subduction to the south–east. Peak metamorphism of the eclogites and high-strain gneissic domains was established. Additionally, slab breakoff was initiated at deeper crustal levels. (B) The tectonic regime became dominated by buoyancy-driven eduction (Andersen *et al.*, 1991; Petersen & Buck, 2015) where rapid exhumation of the eclogite-facies rocks was induced. The result: formation of a mélange-like rock package at mid-crustal levels. (C) Simplified illustration of the post-peak *P–T* paths for the eclogite-facies rocks and upper-amphibolite metapelites. The annotated letters relate these *P–T* paths directly to (A) and (B).

It is worth considering the regional relationship between the Usagaran eclogite-facies rocks and the granulite-facies rocks preserved in northern Malawi (Fig. 22; Ring *et al.*, 1997). Cordierite-garnet granulites (ca. 1988 Ma) formed at 5–5.5 kbar and 750–850 °C (Ring *et al.*, 1997). The agreement in the timing of metamorphism between the eclogites of the Usagaran Belt and low-pressure granulites in northern Malawi suggests they may comprise parts of a Palaeoproterozoic paired metamorphic belt system (Brown, 2006).

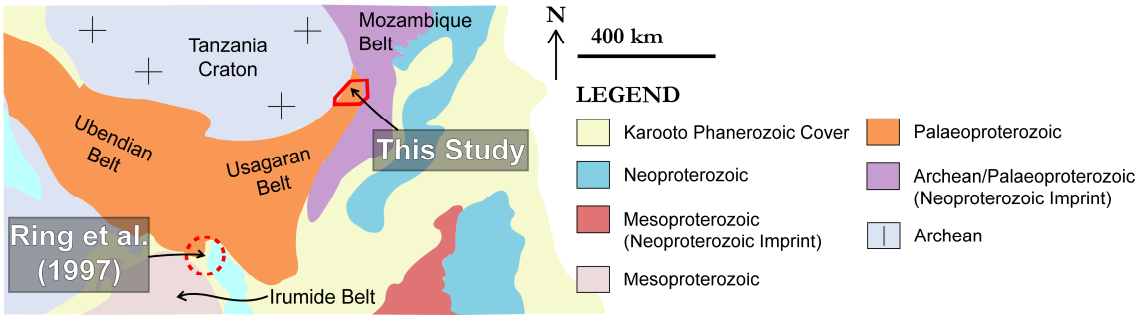

Fig. 22: (A) Modified geological map of central Tanzania (see Figure 3a) emphasising the regional relationship between the Tanzania Craton, the Mozambique Belt (East-African Orogen), the Ubendian and Usagaran Belts, and the Irumide Belt. The region within the dashed red circle represents the location of the high geothermal gradient granulites studied by Ring *et al.* (1997).

As Brown (2006) showed, the preservation of paired metamorphic belts in the geological record marks the emergence of true modern-style subduction-related tectonics on Earth. Furthermore, the demonstration that the Usagaran eclogite-facies rocks experienced a cool geothermal gradient of 460 °C/GPa during burial and subsequent rapid decompression during exhumation supports a geodynamic expression of subduction that is comparable to the modern Earth. Thus, it is conceivable that subduction processes akin to those occurring in the modern Earth were underway by the mid-Palaeoproterozoic.

6. CONCLUSIONS

Rocks comprising the Palaeoproterozoic Isimani Suite in the Usagaran Orogen of central Tanzania were not exhumed as a single, coherent rock package. Ca. 2000 Ma eclogite-facies rocks are envisaged to have been exhumed in two stages: (1) Following ca. 15–18 kbar peak metamorphism, the eclogite-facies rocks were rapidly exhumed through inferred buoyancy-driven tectonics to mid-crustal levels. Based on the retention of high Zr concentrations in <100 μm rutile grains, ca. 11 kbar of exhumation may have occurred within 1 Ma. (2) The exhumed eclogites were subsequently entrained within a comparatively high-strain gneissic matrix that reached peak metamorphic pressures of ca. 7–8 kbar at ca. 1985 ± 23 Ma. The low thermal gradients and apparently rapid exhumation recorded by the Usagaran eclogite-facies rocks, coupled with contemporaneous high thermal gradient metamorphism for the regionally adjacent rocks of northern Malawi, have the hallmarks of a modern-style paired metamorphic system. This suggests that modern-style, subduction-driven geodynamic systems were well established by the mid-Palaeoproterozoic.

ACKNOWLEDGEMENTS

My supervisors, Martin Hand and Renée Tamblyn, are thanked beyond measure for their ongoing support, guidance and enthusiasm. Not only do I appreciate their commitment to the project, I am grateful for their devotion to teach the principles of science – among many other things. Thank you to Laura Morrissey for her invaluable assistance in navigating through the overwhelming world of THERMOCALC, and for the same reason, David Kelsey is also thanked; particularly for his ever-lasting patience. I express thanks to Alec Walsh for his willingness to teach, and for his insights into science and ethics. Sarah Gilbert and Ben Wade are thanked tremendously for their assistance with the analytical equipment at Adelaide Microscopy. The generous support provided from Sarah Gilbert concerning the use of *Iolite* is greatly appreciated. Lastly, thanks are extended to Mitchell Bockmann for his advice on processing geochronological data, and for his continual support throughout the year.

REFERENCES

ABBOTT, R. N., & GREENWOOD, J. P. (2001). Retrograde metamorphism of eclogite in the southern Appalachian Mountains, U.S.A.-A case involving seamount subduction? *Journal of Metamorphic Geology*, 19(4), 433-443. doi:10.1046/j.0263-4929.2001.00321.x

ANDERSEN, T. B. (1991). Subduction and eduction of continental crust: major mechanisms during continent-continent collision and orogenic extensional collapse, a model based on the south Norwegian Caledonides. *Terra Nova*, 3(3), 303-310. doi:10.1111/j.1365-3121.1991.tb00148.x

ANDERSON, E. D., & MOECHER, D. P. (2007). Omphacite breakdown reactions and relation to eclogite exhumation rates. *Contributions to Mineralogy and Petrology, 154*(3), 253-277. doi:10.1007/s00410-007-0192-x

ANDERSON, T. (2002). Correction of common lead in U–Pb analyses that do not report 204Pb. *Chemical Geology*, 192(1-2), 59-79. doi:10.1016/S0009-2541(02)00195-X

BALDWIN, J. A., BOWRING, S. A., WILLIAMS, M. L., & WILLIAMS, I. S. (2004). Eclogites of the Snowbird tectonic zone: petrological and U-Pb geochronological evidence for Paleoproterozoic high-pressure metamorphism in the western Canadian Shield. *Contributions to Mineralogy and Petrology, 147*(5), 528-548. doi:10.1007/s00410-004-0572-4

BALDWIN, J. A., POWELL, R., WILLIAMS, M. L., & GONCALVES, P. (2007). Formation of eclogite, and reaction during exhumation to mid-crustal levels, Snowbird tectonic zone, western Canadian Shield. *Journal of Metamorphic Geology, 25*(9), 953-974. doi:10.1111/j.1525-1314.2007.00737.x

BONIFACE, N., SCHENK, V., & APPEL, P. (2012). Paleoproterozoic eclogites of MORB-type chemistry and three Proterozoic orogenic cycles in the Ubendian Belt (Tanzania): Evidence from monazite and zircon geochronology, and geochemistry. *Precambrian Research, 192-195*, 16-33. doi:10.1016/j.precamres.2011.10.007

BOUSQUET, R. (2008). Metamorphic heterogeneities within a single HP unit: Overprint effect or metamorphic mix? *Lithos*, 103(1-2), 46-69. doi:10.1016/j.lithos.2007.09.010

BRICK, R. A. (2011). *Palaeoproterozoic eclogite formation in Tanzania: a structural, geochronological, thermochronological and metamorphic study of the Usagaran and Ubende orogenic belts.* (Doctorate), University of Adelaide, Australia.

BROMILEY, G. D., & KEPPLER, H. (2004). An experimental investigation of hydroxyl solubility in jadeite and Na-rich clinopyroxenes. *Contributions to Mineralogy and Petrology, 147*(2), 189-200. doi:10.1007/s00410-003-0551-1

BROWN, M. (2006). Duality of thermal regimes is the distinctive characteristic of plate tectonics since the Neoarchean. *Geology, 34*(11), 961-964. doi:10.1130/g22853a.1

BROWN, M. (2007). Metamorphic Conditions in Orogenic Belts: A Record of Secular Change. *International Geology Review, 49*(3), 193-234. doi:10.2747/0020-6814.49.3.193

BROWN, M. (2014). The contribution of metamorphic petrology to understanding lithosphere evolution and geodynamics. *Geoscience Frontiers*, 5(4), 553-569. doi:10.1016/j.gsf.2014.02.005

BROWN, M., & JOHNSON, T. (2018). Secular change in metamorphism and the onset of global plate tectonics. *American Mineralogist*, 103(2), 181-196. doi:10.2138/am-2018-6166

BUROV, E., JOLIVET, L., LE POURHIET, L., & POLIAKOV, A. (2001). A thermomechanical model of exhumation of high pressure (HP) and ultra-high pressure (UHP) metamorphic rocks in Alpine-type collision belts. *Tectonophysics*, 342(1-2), 113-136. doi:10.1016/S0040-1951(01)00158-5

CADDICK, M. J., KONOPÁSEK, J., & THOMPSON, A. B. (2010). Preservation of Garnet Growth Zoning and the Duration of Prograde Metamorphism. *Journal of Petrology*, 51(11), 2327-2347. doi:10.1093/petrology/egq059

CAWOOD, P. A., KRÖNER, A., & PISAREVSKY, S. (2006). Precambrian plate tectonics: Criteria and evidence. *GSA Today, 16*(7), 4-11. doi:10.1130/gsat01607.1

CHERNIAK, D. J., MANCHESTER, J., & WATSON, E. B. (2007). Zr and Hf diffusion in rutile. *Earth and Planetary Science Letters*, 261(1-2), 267-279. doi:10.1016/j.epsl.2007.06.027

CHEW, D. M., PETRUS, J. A., & KAMBER, B. S. (2014). U–Pb LA–ICPMS dating using accessory mineral standards with variable common Pb. *Chemical Geology, 363*, 185-199. doi:10.1016/j.chemgeo.2013.11.006

CHOPIN, C. (2003). Ultrahigh-pressure metamorphism: tracing continental crust into the mantle. *Earth and Planetary Science Letters, 212*(1-2), 1-14. doi:10.1016/s0012-821x(03)00261-9

CHOPIN, C., & SCHERTL, H.-P. (1999). The UHP Unit in the Dora-Maira Massif, Western Alps. *International Geology Review, 41*(9), 765-780. doi:10.1080/00206819909465168

CHU, X., AGUE, J. J., AXLER, J. A., & TIAN, M. (2016). Taconian retrograde eclogite from northwest Connecticut, USA, and its petrotectonic implications. *Lithos, 240-243*, 276-294. doi:10.1016/j.lithos.2015.10.011

COLLINS, A. S., REDDY, S. M., BUCHAN, C., & MRUMA, A. (2004). Temporal constraints on Palaeoproterozoic eclogite formation and exhumation (Usagaran Orogen, Tanzania). *Earth and Planetary Science Letters, 224*(1-2), 175-192. doi:10.1016/j.epsl.2004.04.027

CONDIE, K. C., ASTER, R. C., & VAN HUNEN, J. (2016). A great thermal divergence in the mantle beginning 2.5 Ga: Geochemical constraints from greenstone basalts and komatiites. *Geoscience Frontiers, 7*(4), 543-553. doi:10.1016/j.gsf.2016.01.006

CUTHBERT, S. J., CARSWELL, D. A., KROGH-RAVNA, E. J., & WAIN, A. (2000). Eclogites and eclogites in the Western Gneiss Region, Norwegian Caledonides. *Lithos, 52*(1-4), 165-195. doi:10.1016/S0024-4937(99)00090-0

DEWEY, J. F. (2010). Transtension in Arcs and Orogens. *International Geology Review*, 44(5), 402-439. doi:10.2747/0020-6814.44.5.402

DROOP, G. T. R. (1987). A general equation for estimating Fe3+ concentrations in ferromagnesian silicates and oxides from microprobe analyses, using stoichiometric criteria. *Mineralogical Society*, 51(361), 431-435. doi:10.1180/minmag.1987.051.361.10

DUNKL, I., & VON EYNATTEN, H. (2009). Anchizonal-hydrothermal growth and (U-Th)/He dating of rutile crystals in the sediments of Hawasina window, Oman. *Geochimica et Cosmochimica Acta, 73*(13), A314.

DURETZ, T., & GERYA, T. V. (2013). Slab detachment during continental collision: Influence of crustal rheology and interaction with lithospheric delamination. *Tectonophysics*, 602, 124-140. doi:10.1016/j.tecto.2012.12.024

DURETZ, T., GERYA, T. V., KAUS, B. J. P., & ANDERSEN, T. B. (2012). Thermomechanical modeling of slab eduction. Journal of Geophysical Research: Solid Earth, 117(B8), n/a-n/a. doi:10.1029/2012jb009137

ESKOLA, P. (1921). On the eclogites of Norway. *Videnskapsselskapets Skrifter, I Mat Naturv Klasse, 8*, 1-118.

FRITZ, H., ABDELSALAM, M., ALI, K. A., BINGEN, B., COLLINS, A. S., FOWLER, A. R., . . . VIOLA, G. (2013). Orogen styles in the East African Orogen: A review of the Neoproterozoic to Cambrian tectonic evolution. *Journal of African Earth Sciences, 86*, 65-106. doi:10.1016/j.jafrearsci.2013.06.004

FRITZ, H., TENCZER, V., HAUZENBERGER, C. A., WALLBRECHER, E., HOINKES, G., MUHONGO, S., & MOGESSIE, A. (2005). Central Tanzanian tectonic map: A step forward to decipher Proterozoic structural events in the East African Orogen. *Tectonics*, 24(6), 1-26. doi:10.1029/2005tc001796

GOODGE, G. W., FANNING, C. M., & BENNETT, V. C. (2001). U–Pb evidence of 1.7 Ga crustal tectonism during the Nimrod Orogeny in the Transantarctic Mountains, Antarctica: implications for Proterozoic plate reconstructions. *Precambrian Research, 112*(3-4), 261-288. doi:10.1016/S0301-9268(01)00193-0

GREEN, E. C. R., WHITE, R. W., DIENER, J. F. A., POWELL, R., HOLLAND, T. J. B., & PALIN, R. M. (2016). Activity-composition relations for the calculation of partial melting equilibria in metabasic rocks. *Journal of Metamorphic Geology, 34*(9), 845-869. doi:10.1111/jmg.12211

HACKER, B. R. (1996). Eclogite formation and the Rheology, Buoyancy, Seismicity, and H2O Content of Oceanic Crust. *American Geophysical Union*, 337-346. doi:10.1029/GM096p0337

HACKER, B. R., & GERYA, T. V. (2013). Paradigms, new and old, for ultrahigh-pressure tectonism. *Tectonophysics*, 603, 79-88. doi:10.1016/j.tecto.2013.05.026

HAMILTON, W. B. (1998). Archean Tectonics and Magmatism. *International Geology Review, 40*(1), 1-39. doi:10.1080/00206819809465196

HAMILTON, W. B. (2011). Plate tectonics began in Neoproterozoic time, and plumes from deep mantle have never operated. *Lithos, 123*(1-4), 1-20. doi:10.1016/j.lithos.2010.12.007

HARLEY, S. L. (1984). An experimental study of the partitioning of Fe and Mg between garnet and orthopyroxene. *Contributions to Mineralogy and Petrology*, 86(4), 359-373. doi:10.1007/BF01187140

HEINRICH, C. A. (1982). Kyanite-Eclogite to Amphibolite Facies Evolution of Hydrous Mafic and Pelitic Rocks, Adula Nappe, Central Alps. *Contributions to Mineralogy and Petrology*, 81(1), 30-38. doi:10.1007/BF00371156

HELLSTROM, J., PATON, C., WOODHEAD, J. D., & HERGT, J. (2008). Iolite: Software for spatially resolved LA–(QUAD and MC)–ICP–MS Analysis. *Mineralogical Association of Canada, Short Course Series*, 40, 343-348.

HERMS, P. (2002). Fluids in a 2 Ga old subduction zone – deduced from eclogite-facies rocks of the Usagaran belt, Tanzania. *European Journal of Mineralogy, 14*(2), 361-373. doi:10.1127/0935-1221/2002/0014-0361

HOLLAND, T. J. B., & POWELL, R. (2003). Activity–composition relations for phases in petrological calculations: an asymmetric multicomponent formulation. *Contributions to Mineralogy and Petrology, 145*, 492-501. doi:10.1007/s00410-003-0464-z

HOLLAND, T. J. B., & POWELL, R. (2011). An improved and extended internally consistent thermodynamic dataset for phases of petrological interest, involving a new equation of state for solids. *Journal of Metamorphic Geology, 29*(3), 333-383. doi:10.1111/j.1525-1314.2010.00923.x

JAMTVEIT, B. (1987). Metamorphic evolution of the Eiksunddal eclogite complex. Western Norway, and some tectonic implications. *Contributions to Mineralogy and Petrology*, 95(1), 82-99. doi:10.1007/BF00518032

JANÁK, M., CORNELL, D., FROITZHEIM, N., DE HOOG, J. C. M., BROSKA, I., VRABEC, M., & HURAI, V. (2009). Eclogite-hosting metapelites from the Pohorje Mountains (Eastern Alps): P-T evolution, zircon geochronology and tectonic implications. *European Journal of Mineralogy, 21*(6), 1191-1212. doi:10.1127/0935-1221/2009/0021-1966

JOCHUM, K. P., WEIS, U., STOLL, B., KUZMIN, D., YANG, Q., RACZEK, I., . . . ENZWEILER, J. (2011). Determination of Reference Values for NIST SRM 610-617 Glasses Following ISO Guidelines. *Geostandards and Geoanalytical Research, 35*(4), 397-429. doi:10.1111/j.1751-908X.2011.00120.x

JOCHUM, K. P., WILSON, S. A., ABOUCHAMI, W., AMINI, M., CHMELEFF, J., EISENHAUER, A., . . . WOODHEAD, J. D. (2010). GSD-1G and MPI-DING Reference Glasses for In Situ and Bulk Isotopic Determination. *Geostandards and Geoanalytical Research, 35*(2), 193-226. doi:10.1111/j.1751-908X.2010.00114.x

JOHNSON, T. E., & WHITE, R. W. (2011). Phase equilibrium constraints on conditions of granulite-facies metamorphism at Scourie, NW Scotland. *Journal of the Geological Society, 168*(1), 147-158. doi:10.1144/0016-76492010-069

KATAYAMA, I., & NAKASHIMA, S. (2003). Hydroxyl in clinopyroxene from the deep subducted crust: Evidence for H_2O transport into the mantle. *American Mineralogist, 88*(1), 229-234. doi:10.2138/am-2003-0126

KRÖNER, A., WILDE, S. A., ZHAO, G. C., O'BRIEN, P. J., SUN, M., LIU, D. Y., . . . GUO, J. H. (2006). Zircon geochronology and metamorphic evolution of mafic dykes in the Hengshan Complex of northern China: Evidence for late Palaeoproterozoic extension and subsequent high-pressure metamorphism in the North China Craton. *Precambrian Research, 146*(1-2), 45-67. doi:10.1016/j.precamres.2006.01.008

LAU, W. K. (2009). *Geochemical and Sm-Nd isotopic composition of Palaeoproterozoic eclogite and associated rocks in the Usagaran Orogenic Belt, Tanzania.* (Honours), University of Adelaide, Australia.

LI, X., ZHANG, L., WEI, C., & SLABUNOV, A. I. (2015). Metamorphic PT path and zircon U–Pb dating of Archean eclogite association in Gridino complex, Belomorian province, Russia. *Precambrian Research, 268*, 74-96. doi:10.1016/j.precamres.2015.07.009

LI, X., ZHANG, L., WEI, C., SLABUNOV, A. I., & BADER, T. (2017). Neoarchean-Paleoproterozoic granulite-facies metamorphism in Uzkaya Salma eclogite-bearing mélange, Belomorian Province (Russia). *Precambrian Research, 294*, 257-283. doi:10.1016/j.precamres.2017.03.031

LIU, J., JAHN, B., DONG, S., LI, H., & OBERHANSLI, R. (2003). Neoproterozoic Granitoid Did Not Record Ultrahigh-Pressure Metamorphism from the Southern Dabieshan of China. *The Journal of Geology*, 111(719-732). doi:10.1086/378336

LIU, J., YEA, K., MARUYAMA, S., CONG, B., & FAN, H. (2001). Mineral Inclusions in Zircon from Gneisses in the Ultrahigh-Pressure Zone of the Dabie Mountains, China. *The Journal of Geology*, 109(4), 523-535. doi:10.1086/320796

LOMBARDO, B., & ROLFO, F. (2000). Two contrasting eclogite types in the Himalayas: implications for the Himalayan orogeny. *Journal of Geodynamics, 30*(1-2), 37-60. doi:10.1016/S0264-3707(99)00026-5

LOOSE, D., & SCHENK, V. (2018). 2.09 Ga old eclogites in the Eburnian-Transamazonian orogen of southern Cameroon: Significance for Palaeoproterozoic plate tectonics. *Precambrian Research, 304*, 1-11. doi:10.1016/j.precamres.2017.10.018

LUVIZOTTO, G. L., ZACK, T., MEYER, H. P., LUDWIG, T., TRIEBOLD, S., KRONZ, A., . . . VON EYNATTEN, H. (2009). Rutile crystals as potential trace element and isotope mineral standards for microanalysis. *Chemical Geology, 261*(3-4), 346-369. doi:10.1016/j.chemgeo.2008.04.012

MABOKO, M. A. H. (2000). Nd and Sr isotopic investigation of the Archean–Proterozoic boundary in north eastern Tanzania: constraints on the nature of Neoproterozoic tectonism in the Mozambique Belt. *Precambrian Research, 102*(1-2), 87-98. doi:10.1016/S0301-9268(00)00060-7

MARMO, B. A., CLARKE, G. L., & POWELL, R. (2002). Fractionation of bulk rock composition due to porphyroblast growth: effects on eclogite facies mineral equilibria, Pam Peninsula, New Caledonia. *Journal of Metamorphic Geology*, 20(1), 151-165. doi:10.1046/j.0263-4929.2001.00346.x

MEYRE, C., DE CAPITANI, C., ZACK, T., & FREY, M. (1999). Petrology of High-Pressure Metapelites from the Adula Nappe (Central Alps, Switzerland). *Journal of Petrology, 40*(1), 199-213. doi:10.1093/petroj/40.1.199

MINTS, M. V., BELOUSOVA, E. A., KONILOV, A. N., NATAPOV, L. M., SHCHIPANSKY, A. A., GRIFFIN, W. L., . . . KAULINA, T. V. (2010). Mesoarchean subduction processes: 2.87 Ga eclogites from the Kola Peninsula, Russia. *Geology, 38*(8), 739-742. doi:10.1130/g31219.1

MÖLLER, A. (1995). *Eclogites and migmatitic gneisses in the Usagaran domain* (Doctorate), Universität Kiel, Mainz, Germany.

MÖLLER, A., APPEL, P., MEZGER, K., & SCHENK, V. (1995). Evidence for a 2Ga subduction zone: Eclogites in the Usagaran belt of Tanzania. *Geology, 23*(12), 1067-1070. doi:10.1130/0091-7613(1995)023

MÖLLER, A., MEZGER, K., & SCHENK, V. (1998). Crustal Age Domains and the Evolution of the Continental Crust in the Mozambique Belt of Tanzania: Combined Sm–Nd, Rb–Sr, and Pb–Pb Isotopic Evidence. *Journal of Petrology, 39*(4), 749-783. doi:10.1093/petroj/39.4.749

MÖLLER, A., MEZGER, K., & SCHENK, V. (2000). U–Pb dating of metamorphic minerals: Pan-African metamorphism and prolonged slow cooling of high pressure granulites in Tanzania, East Africa. *Precambrian Research, 104*(3-4), 123-146. doi:10.1016/S0301-9268(00)00086-3

MOYEN, J. F., STEVENS, G., & KISTERS, A. (2006). Record of mid-Archaean subduction from metamorphism in the Barberton terrain, South Africa. *Nature, 442*(7102), 559-562. doi:10.1038/nature04972

MRUMA, A. (1989). *Stratigraphy, Metamorphism and Tectonic Evolution of the Early Proterozoic Usagaran Belt, Tanzania*. University of Oulu, Finland.

MUHONGO, S., KRÖNER, A., & NEMCHIN, A. A. (2001). Single Zircon Evaporation and SHRIMP Ages for Granulite-Facies Rocks in the Mozambique Belt of Tanzania *The Journal of Geology, 109*(2), 171-189. doi: 10.1086/319240

MÜLLER, S., DZIGGEL, A., KOLB, J., & SINDERN, S. (2018). Mineral textural evolution and PT-path of relict eclogite-facies rocks in the Paleoproterozoic Nagssugtoqidian Orogen, South-East Greenland. *Lithos, 296-299*, 212-232. doi:10.1016/j.lithos.2017.11.008

MYSEN, B., & GRIFFIN, W. L. (1973). Pyroxene stoichiometry and the breakdown of omphacite. *American Mineralogist, 58*(1-2), 60-63.

NUTMAN, A. P., FRIEND, C. R. L., & BENNETT, V. C. (2002). Evidence for 3650-3600 Ma assembly of the northern end of the Itsaq Gneiss Complex, Greenland: Implication for early Archaean tectonics. *Tectonics, 21*(1), 5-1-5-28. doi:10.1029/2000tc001203

NUTMAN, A. P., KALSBEEK, F., & FRIEND, C. R. L. (2008). The Nagssugtoqidian Orogen in south-east Greenland: Evidence for Paleoproterozoic collision and plate assembly. *American Journal of Science, 308*, 529-572. doi:10.2475/04.2008.06

O'BRIEN, P. J., & RÖTZLER, J. (2003). High-pressure granulites: formation, recovery of peak conditions and implications for tectonics. *Journal of Metamorphic Geology, 21*(1), 3-20. doi:10.1046/j.1525-1314.2003.00420.x

OTAMENDI, J. E., DE LA ROSA, J. D., PATINO DOUCE, A. E., & CASTRO, A. (2002). Rayleigh fractionation of heavy rare earths and yttrium during metamorphic garnet growth. *Geological Society of America*, 30(2), 159-162. doi:10.1130/0091-7613(2002)030<0159:RFOHRE>2.0.CO;2

PALMERI, R., CHMIELOWSKI, R., SANDRONI, S., TALARICO, F., & RICCI, C. A. (2009). Petrology of the eclogites from western Tasmania: Insights into the Cambro-Ordovician evolution of the paleo-Pacific margin of Gondwana. *Lithos*, 109(3-4), 223-239. doi:10.1016/j.lithos.2008.06.016

PAPE, J., MEZGER, K., & ROBYR, M. (2016). A systematic evaluation of the Zr-in-rutile thermometer in ultra-high temperature (UHT) rocks. *Contributions to Mineralogy and Petrology*, 171(5). doi:10.1007/s00410-016-1254-8

PATON, C., HELLSTROM, J., PAUL, B., WOODHEAD, J., & HERGT, J. (2011). Iolite: Freeware for the visualisation and processing of mass spectrometric data. *Journal of Analytical Atomic Spectrometry, 26*(12), 2508. doi:10.1039/c1ja10172b

PATON, C., WOODHEAD, J. D., HELLSTROM, J. C., HERGT, J. M., GREIG, A., & MAAS, R. (2010). Improved laser ablation U-Pb zircon geochronology through robust downhole fractionation correction. *Geochemistry, Geophysics, Geosystems*, 11(3). doi:10.1029/2009gc002618

PEACOCK, S. M., & GOODGE, G. W. (1995). Eclogite-facies metamorphism preserved in tectonic blocks from a lower crustal shear zone, central Transantarctic Mountains, Antarctica. *Lithos, 36*(1), 1-13. doi:10.1016/0024-4937(95)00006-2

PEARCE, M. A., WHITE, A. J. R., & GAZLEY, M. F. (2015). TCInvestigator: automated calculation of mineral mode and composition contours for thermocalc pseudosections. *Journal of Metamorphic Geology, 33*(4), 413-425. doi:10.1111/jmg.12126

PETERSEN, K. D., & BUCK, W. R. (2015). Eduction, extension, and exhumation of ultrahigh-pressure rocks in metamorphic core complexes due to subduction initiation. *Geochemistry, Geophysics, Geosystems*, 16(8), 2564-2581. doi:10.1002/2015gc005847

PETRUS, J. A., & KAMBER, B. S. (2012). VizualAge: A Novel Approach to Laser Ablation ICP-MS U-Pb Geochronology Data Reduction. *Geostandards and Geoanalytical Research, 36*(3), 247-270. doi:10.1111/j.1751-908X.2012.00158.x

PULLEN, A., KAPP, P., GEHRELS, G. E., DING, L., & ZHANG, Q. (2011). Metamorphic rocks in central Tibet: Lateral variations and implications for crustal structure. *Geological Society of America Bulletin*, 123(3-4), 585-600. doi:10.1130/b30154.1

REDDY, S. M., COLLINS, A. S., & MRUMA, A. (2003). Complex high-strain deformation in the Usagaran Orogen, Tanzania: structural setting of Palaeoproterozoic eclogites. *Tectonophysics, 375*(1-4), 101-123. doi:10.1016/s0040-1951(03)00335-4

REDDY, S. M., COLLINS, A. S., BUCHAN, C., & MRUMA, A. H. (2004). Heterogeneous excess argon and Neoproterozoic heating in the Usagaran Orogen, Tanzania, revealed by single grain 40Ar/39Ar thermochronology. *Journal of African Earth Sciences, 39*(3-5), 165-176. doi:10.1016/j.jafrearsci.2004.07.052

RING, U., KRÖNER, A., & TOULKERIDIS, T. (1997). Palaeoproterozoic granulite-facies metamorphism and granitoid intrusions in the Ubendian-Usagaran Orogen of northern Malawi, east-central Africa. *Precambrian Research, 85*(1-2), 27-51.

ROSENBERG, C. L., & HANDY, M. R. (2005). Experimental deformation of partially melted granite revisited: implications for the continental crust. *Journal of Metamorphic Geology, 23*(1), 19-28. doi:10.1111/j.1525-1314.2005.00555.x

SHENG, Y.-M., & GONG, B. (2017). Hydrous species in eclogitic omphacite: Implication for metamorphic dehydration during exhumation. *Journal of Asian Earth Sciences, 145*, 123-129. doi:10.1016/j.jseaes.2016.12.020

SHIREY, S. B., & RICHARDSON, S. H. (2011). Start of the Wilson Cycle at 3 Ga Shown by Diamonds from Subcontinental Mantle. *Science, 333*, 434-436. doi:10.1126/science.1206275

SKLYAROV, E. V., THEUNISSEN, K., MELNIKOV, A. I., KLERKX, J., GLADKOCHUB, D. P., & MRUMA, A. (1998). Paleoproterozoic eclogites and garnet pyroxenites of the Ubende belt (Tanzania). *Swiss Bulletin of Mineralogy and Petrology, 78*, 257-271. doi:10.5169/seals-59287

SKUBLOV, S. G., BEREZIN, A. V., MARIN, Y. B., RIZVANOVA, N. G., BOGOMOLOV, E. S., SERGEEVA, N. A., . . . GUSEVA, V. F. (2010). Complex isotopic-geochemical (Sm-Nd, U-Pb) study of Salma eclogites. *Doklady Earth Sciences, 434*(2), 1396-1400. doi:10.1134/s1028334x10100247

SMITHIES, R. H., CHAMPION, D. C., VAN KRANENDONK, M. J., HOWARD, H. M., & HICKMAN, A. H. (2005). Modern-style subduction processes in the Mesoarchaean: Geochemical evidence from the 3.12 Ga Whundo intra-oceanic arc. *Earth and Planetary Science Letters, 231*(3-4), 221-237. doi:10.1016/j.epsl.2004.12.026

SMYTH, J. R., BELL, D. R., & ROSSMAN, G. R. (1991). Incorporation of hydroxyl in upper-mantle clinopyroxenes *Nature, 351*(6329), 732-735.

SOMMER, H., KRÖNER, A., HAUZENBERGER, C. A., MUHONGO, S., & WINGATE, M., T,D. (2003). Metamorphic petrology and zircon geochronology of high-grade rocks from the central Mozambique Belt of Tanzania: crustal recycling of Archean and Palaeoproterozoic material during the Pan-African orogeny. *Journal of Metamorphic Geology, 21*(9), 915-934. doi:10.1046/j.1525-1314.2003.00491.x

STACEY, J. S., & KRAMERS, J. D. (1975). Approximation of terrestrial lead isotope evolution by a two-stage model. *Earth and Planetary Science Letters*, 26(2), 207-221. doi:10.1016/0012-821X(75)90088-6

STERN, R. J. (2005). Evidence from ophiolites, blueschists, and ultrahigh-pressure metamorphic terranes that the modern episode of subduction tectonics began in Neoproterozoic time. *Geology, 33*(7), 557. doi:10.1130/g21365.1

STERN, R. J. (2007). When and how did plate tectonics begin? Theoretical and empirical considerations. *Chinese Science Bulletin, 52*(5), 578-591. doi:10.1007/s11434-007-0073-8

STERN, R. J., LEYBOURNE, M. I., & TSUJIMORI, T. (2016). Kimberlites and the start of plate tectonics. *Geology, 44*(10), 799-802. doi:10.1130/g38024.1

STIPSKA, P., PITRA, P., & POWELL, R. (2006). Separate or shared metamorphic histories of eclogites and surrounding rocks? An example from the Bohemian Massif. *Journal of Metamorphic Geology, 24*(3), 219-240. doi:10.1111/j.1525-1314.2006.00634.x

STÜWE, K. (1997). Effective bulk composition changes due to cooling: a model predicting complexities in retrograde reaction textures. *Contributions to Mineralogy and Petrology*, 129(1), 43-52. doi:10.1007/s004100050322

TOMKINS, H. S., POWELL, R., & ELLIS, D. J. (2007). The pressure dependence of the zirconium-in-rutile thermometer. *Journal of Metamorphic Geology, 25*(6), 703-713. doi:10.1111/j.1525-1314.2007.00724.x

TUCKER, N. M., HAND, M., KELSEY, D. E., & DUTCH, R. A. (2015). A duality of timescales: Short-lived ultrahigh temperature metamorphism preserving a long-lived monazite growth history in the Grenvillian Musgrave–Albany–Fraser Orogen. *Precambrian Research*, 264, 204-234. doi:10.1016/j.precamres.2015.04.015

VAN KRANENDONK, M. J., HUGH SMITHIES, R., HICKMAN, A. H., & CHAMPION, D. C. (2007). Review: secular tectonic evolution of Archean continental crust: interplay between horizontal and vertical processes in the formation of the Pilbara Craton, Australia. *Terra Nova, 19*(1), 1-38. doi:10.1111/j.1365-3121.2006.00723.x

VOGEL, D. E. (1966). Nature and Chemistry of the formation of clinopyroxene-plagioclase symplectite from omphacite. *Neues Jahrb Mineral Monatsh, 6*, 185-189.

VOLODICHEV, O. I., SLABUNOV, A. I., BIBIKOVA, E. V., KONILOV, A. N., & KUZENKO, T. I. (2004). Archean eclogites in the Belomorian mobile belt, baltic shield. *Petrology, 12*(6), 540-560.

WALSH, A. K., KELSEY, D. E., KIRKLAND, C. L., HAND, M., SMITHIES, R. H., CLARK, C., & HOWARD, H. M. (2015). P–T–t evolution of a large, long-lived, ultrahigh-temperature Grenvillian belt in central Australia. *Gondwana Research*, 28(2), 531-564. doi:10.1016/j.gr.2014.05.012

WATSON, E. B., WARK, D. A., & THOMAS, J. B. (2006). Crystallization thermometers for zircon and rutile. *Contributions to Mineralogy and Petrology, 151*(4), 413-433. doi:10.1007/s00410-006-0068-5

WELLER, O. M., & ST-ONGE, M. R. (2017). Record of modern-style plate tectonics in the Palaeoproterozoic Trans-Hudson orogen. *Nature Geoscience, 10*(4), 305-311. doi:10.1038/ngeo2904

WHITE, R. W., & POWELL, R. (2002). Melt loss and the preservation of granulite facies mineral assemblages. *Journal of Metamorphic Geology*, 20(7), 621-632. doi:10.1046/j.1525-1314.2002.00206_20_7.x

WHITE, R. W., POWELL, R., & JOHNSON, T. E. (2014b). The effect of Mn on mineral stability in metapelites revisited: new a-x relations for manganese-bearing minerals. *Journal of Metamorphic Geology, 32*(8), 809-828. doi:10.1111/jmg.12095

WHITE, R. W., POWELL, R., HOLLAND, T. J. B., & WORLEY, B. A. (2000). The effect of TiO2 and Fe2O3 on metapelitic assemblages at greenschist and amphibolite facies conditions: mineral equilibria calculations in the system K2O–FeO–MgO–Al2O3–SiO2–H2O–TiO2–Fe2O3. *Journal of Metamorphic Geology, 18*(5), 497-511. doi:10.1046/j.1525-1314.2000.00269.x

WHITE, R. W., POWELL, R., HOLLAND, T. J. B., JOHNSON, T. E., & GREEN, E. C. R. (2014a). New mineral activity-composition relations for thermodynamic calculations in metapelitic systems. *Journal of Metamorphic Geology, 32*(3), 261-286. doi:10.1111/jmg.12071

WHITNEY, D. L., & EVANS, B. W. (2010). Abbreviations for names of rock-forming minerals. *American Mineralogist, 95*(1), 185-187. doi:10.2138/am.2010.3371

WOODHEAD, J. D., HELLSTROM, J., PATON, C., HERGT, J. M., GREIG, A., & MASS, R. (2008). A guide to depth profiling and imaging applications of ICP-MS. *Mineralogical Association of Canada, Short Course Series, 40*, 135-145.

YEA, K., YAO, Y., KATAYAMA, I., CONG, B., WANG, Q., & MARUYAMA, S. (2000). Sulu ultrahigh-pressure terrane of East China: new implications from coesite and omphacite inclusions in zircon of granitic gneiss. *Lithos, 52*(1-4), 157-164. doi:10.1016/S0024-4937(99)00089-4

YU, H. L., ZHANG, L. F., WEI, C. J., LI, X. L., & GUO, J. H. (2017). Age and P-T conditions of the Gridino-type eclogite in the Belomorian Province, Russia. *Journal of Metamorphic Geology, 35*(8), 855-869. doi:10.1111/jmg.12258

ZACK, T., STOCKLI, D. F., LUVIZOTTO, G. L., BARTH, M. G., BELOUSOVA, E. A., WOLFE, M. R., & HINTON, R. W. (2011). In situ U–Pb rutile dating by LA-ICP-MS: 208Pb correction and prospects for geological applications. *Contributions to Mineralogy and Petrology, 162*, 515-530. doi:10.1007/s00410-011-0609-4

ZHAO, G. C., CAWOOD, P. A., WILDE, S. A., & LU, L. (2001). High-Pressure Granulites (Retrograded Eclogites) from the Hengshan Complex, North China Craton: Petrology and Tectonic Implications. *Journal of Petrology, 42*(6), 1141-1170. doi:10.1093/petrology/42.6.1141

APPENDIX 1a: Mineral Composition Measurement Methods

Electron Probe Micro Analyses (EPMA)

Elemental X-ray maps and mineral composition elemental analyses were obtained using a CAMECA SXFive electron microprobe at Adelaide Microscopy. Elemental X-ray maps were created for garnet porphyroblasts and clinopyroxene-plagioclase intergrowth textures. X-ray maps were obtained for Al, Ca, Ce, Fe, K, Mg, Mn, Na, P, S, Si, Ti, Y and Zr using both Energy Dispersive Spectrometers (EDS) and Wavelength Dispersive Spectrometers (WDS). All maps were created with a beam current of 200 nA and an accelerating voltage of 15 kV. Mineral composition spot analyses for CaO, MgO, TiO_2, SiO_2, Al_2O_3, FeO, MnO, Cr_2O_3, K_2O, P_2O_5, Na_2O, BaO, V_2O_3, ZnO, Cl and F were employed using a beam current of 20 nA, a beam size of 2 μm and an accelerating voltage of 15 kV in WDS. Appendices 2c and d summarise all data pertaining to EPMA.

LA–ICP–MS Rare-Earth Element Distributions

Rare-earth element abundances were measured along garnet spot traverses using a RESOlution LR 193 nm Excimer laser system coupled with an Agilent 7900x ICP–MS at Adelaide Microscopy. The largest garnets were selected for analysis to increase the likelihood of measuring any preserved garnet zonation. As with Rutile U–Pb rutile geochronology, data processing was performed using *Iolite*. The primary and secondary standards were NIST-612 and GSD-1G, respectively (Jochum *et al*., 2010; Jochum *et al*., 2011). Rare-earth element data is presented in Appendix 2e.

EPMA-derived elemental X-ray maps of garnet in thin-section samples T01-40, T06-20 and T06-30 were used in preparation for LA–ICP–MS analysis to identify zoning

domains in garnet porphyroblasts. The density of analyses across garnet porphyroblasts must be varied as a function of how the garnets are zoned to ensure all zonation domains are represented in the data. In sample T06-20, a garnet with a diameter of 8–10 mm was chosen for analysis. The diameter of this garnet is comparable to that of garnet in metapelitic sample T69-6 at Yalumba Hill, previously studied by Möller *et al*., (1995). To facilitate a direct comparison in garnet rare-earth element profiles between samples T01-40 and T06-30, garnet was selected in sample T06-30 that compares well in diameter to T01-40 garnet. T06-30 thin-section samples comprised large garnet porphyroblasts (8–10 mm) and therefore were inadequate to use for analysis. Instead, rock blocks containing 2–3 mm garnets were mounted in epoxy resin, polished and used for LA–ICP–MS analysis. One 8–10 mm garnet porphyroblast in thin-section sample T06-30 was additionally analysed for the sake of completeness. A laser repetition rate of 5 Hz, an energy of 115 mJ and an operating voltage of 25 kV were applied during LA–ICP–MS analysis. The total acquisition time for each analysis was 70 seconds, encompassing 30 seconds of background measurement and a further 40 seconds of ablation. Spot sizes implemented were 29 μm (T01-40), 43 μm (T06-20) and both 29 and 19 μm (T06-30), and spots were programmed as transects along garnet porphyroblasts. The use of the smaller 19 μm spot size in T06-30 was for the purpose of better resolving the fine zonation signature present at garnet rims, identified through Electron Probe Micro Analysis. The majority of the traverse for garnet T06-30 was undertaken with a spot size of 29 μm. To show that rare-earth element concentrations were not affected by variable spot sizes, the secondary standard GSD-1G was used at three different spot-sizes (19 μm, 29 μm and 51 μm). The following figure details the concentrations of selected rare-earth elements as a function of the variable spot sizes in GSD-1G (n = 18).

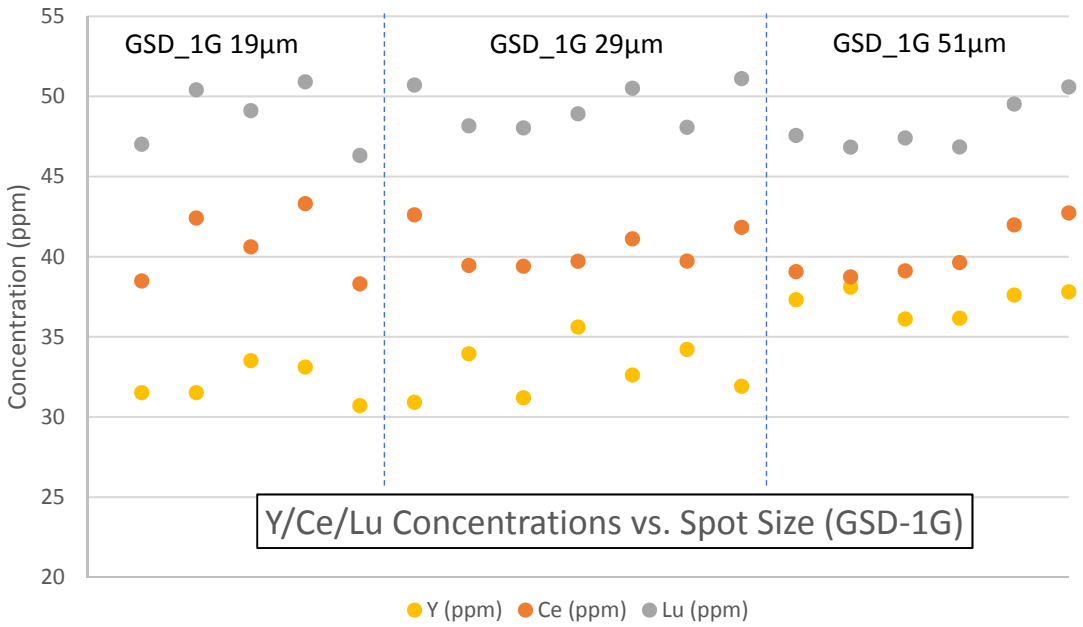

The standards, NIST-612 (Y = 38.3 ± 1.4 ppm, Zr = 37.9 ± 1.2 ppm, La = 36 ± 0.7 ppm, Ce = 38.4 ± 0.7, Pr = 37.9 ± 1 ppm, Nd = 35.5 ± 0.7 ppm, Sm = 37.7 ± 0.8 ppm, Eu = 35.6 ± 0.8 ppm, Gd = 37.3 ± 0.9 ppm, Tb = 37.6 ± 1.1 ppm, Dy = 35.5 ± 0.7 ppm, Ho = 38.3 ± 0.8 ppm, Er = 38 ± 0.9 ppm, Tm = 36.8 ± 0.6 pm, Yb = 39.2 ± 0.9 ppm, Lu = 37 ± 0.9 ppm, Hf = 36.7 ± 1.2 ppm, Pb = 38.6 ± 0.2 ppm, Th = 37.8 ± 0.08 ppm and U = 37.4 ± 0.08 ppm); (Jochum *et al*., 2011) and GSD-1G (Y = 42 ± 2 ppm, Zr = 42 ± 2 ppm, La = 3.1 ± 0.4 ppm, Ce = 41.4 ± 0.4, Pr = 45 ± 1 ppm, Nd = 44.7 ± 0.5 ppm, Sm = 47.8 ± 0.5 ppm, Eu = 41 ± 2 ppm, Gd = 50.7 ± 0.5 ppm, Tb = 47 ± 2 ppm, Dy = 51.2 ± 0.5 ppm, Ho = 49 ± 2 ppm, Er = 40.1 ± 0.4 ppm, Tm = 49 ± 2 pm, Yb = 50.9 ± 0.5 ppm, Lu = 51.5 ± 0.5 ppm, Hf = 39 ± 2 ppm, Pb = 50 ± 2 ppm, Th = 41 ± 2 ppm and U = 41 ± 2 ppm); (Jochum *et al*., 2011) were used to correct for downhole fractionation effects and instrument drift. The trace element concentrations pertaining to the standards, NIST-612 and GSD-1G in this study were highly comparable to the reference values listed above. The data reduction scheme, Trace_Elements_IS in *Iolite* was implemented. The

Trace_Elements_IS DRS requires the user to first specify an internal element standard – typically an element that the mineral of interest is rich and homogenous in. In this case, Al was used for all samples where Al(T01-40) = 11.37 wt%, Al(T06-20) = 11.36 wt% and Al(T06-30) = 11.28 wt%. These values were derived from Electron Probe Micro Analyses of the garnets of interest (Appendix 2c). The procedure of 'bracketing', whereby signals are shortened or lengthened to minimise noise, was strictly undertaken. Here, signals were altered that showed evidence of rutile and zircon inclusions in garnet (i.e. ^{47}Ti, ^{90}Zr, ^{175}Lu and ^{178}Hf peaks).

APPENDIX 1b: Extended LA–ICP–MS Rutile U–Pb Geochronology Methods

Elongated 50–200 μm rutile grains in thin-section samples T06-20, T06-21, T06-21A and T06-27 were imaged with a petrographic microscope in both plane-polarised light and reflected light to identify their textural relationships. Those that were armoured within garnet porphyroblasts were prioritised in an effort to acquire ages most representative of peak metamorphism. A 51 μm spot size was utilised for each analysis; the beam operating with a repetition rate of 5 Hz, and energy of 135 mJ and an operating voltage of 25 kV. Background counts were acquired for 30 seconds prior to 40 seconds of ablation time.

Downhole fractionation and instrument drift were corrected for using the primary standard, R10 (^{207}Pb/^{235}U = 1085.1 to 1096.2 Ma and ^{206}Pb/^{238}U = 1086.3–1096.6 Ma); (Luvizotto *et al*., 2009) from Gjerstad, Norway and the secondary standard, R19 (weighted mean ^{206}Pb/^{238}U TIMS age = 489.5 ± 0.9 Ma); (Zack *et al*., 2011) from Blumberg, South Australia. In this study, R10 yielded an average ^{207}Pb/^{235}U age of 1087.9 ± 13.2 Ma and an average ^{206}Pb/^{238}U age of 1092.54 ± 10.7 Ma (n = 10, 2σ errors). R19

yielded an average $^{207}Pb/^{235}U$ age of 469.3 ± 45.3 Ma and an average $^{206}Pb/^{238}U$ age of 507.9 ± 18.4 Ma (n = 10, 2σ errors).

Internal standards, R10 and R19 were both utilized in the processing of the data, which was undertaken using the data processing software, *Iolite*. Raw data is converted into processed data (i.e. data having been corrected for downhole fractionation, instrument drift, baseline subtraction and mass bias) through the application of a data reduction scheme (DRS) in *Iolite*. Three data reduction schemes were used in *Iolite*: the U–Pb Geochronology DRS (Paton *et al*., 2010), the VizualAge DRS (Petrus & Kamber, 2012) and the VizualAge UcomPbine DRS (Chew *et al*., 2014). The U–Pb Geochronology DRS was used initially to derive a set of $^{207}Pb/^{235}U$, $^{206}Pb/^{238}U$ and $^{206}Pb/^{207}Pb$ ratios and corresponding ages for both the samples and internal standards. The output channels, ^{47}Ti, ^{29}Si, ^{57}Fe, ^{208}Pb, ^{238}U (counts per second), $^{206}Pb/^{238}U$ and $^{207}Pb/^{235}U$ (ratios), which were derived after application of the DRS, were monitored for any heterogeneity. Because analysed rutile grains were included within garnet, ^{29}Si and ^{57}Fe signals were incorporated to identify any garnet contamination present in the analysis. Analyses that showed a decreasing ^{47}Ti signal with ablation time also showed a coupled increase in both ^{29}Si and ^{57}Fe. $^{206}Pb/^{238}U$ and $^{207}Pb/^{235}U$ ratios were largely flat and conformable among the totality of the analyses, however, some analyses showed scattered and variable ratios, attributable to low ^{238}U counts. Signals of this nature were 'bracketed' – that is, abnormal signals were typically shortened. Specifically, signals were shortened to remove spikes in ^{29}Si and ^{57}Fe and to conserve ^{47}Ti. Signals were also shortened to minimise scatter in $^{206}Pb/^{238}U$ and $^{207}Pb/^{235}U$ ratios. All data processing was undertaken with a strict provision to avoid data manipulation. The same U–Pb Geochronology DRS was

implemented multiple times following the 'bracketing' of the data-set. The VizualAge DRS was subsequently implemented on all samples because of its usefulness in applying a common Pb correction using both the Andersen Routine (Andersen, 2002) and the Stacey and Kramers (1975) Pb evolution model. Calculated $^{206}Pb/^{207}Pb$ ratios are used in an iterative calculation to estimate common lead corrected ages. In this case, ^{208}Pb is used as the proxy for common lead since rutile lacks meaningful concentrations of ^{232}Th. Thus, all ^{208}Pb is inferred to be non-radiogenic. The VizualAge UcomPbine DRS was also used to apply a correction for common lead. This DRS differs from the VizualAge DRS in that the programmer must input initial common $^{208}Pb/^{206}Pb$ and $^{207}Pb/^{206}Pb$ ratios. The Stacey and Kramers (1975) Pb evolution model was incorporated in deriving these common Pb ratios. For reasonable application of the model one must estimate an age, inferred to represent the primary event responsible for common Pb incorporation into the system. The data processed both with and without the common Pb corrections were compared using Tera-Wasserberg Concordia plots.

APPENDIX 1c: Extended Mineral Equilibria Forward Modelling Methods

Performing Calculations in THERMOCALC

THERMOCALC is a thermodynamic calculation program that comprises two input systems: a *dataset* describing the thermodynamic variables for each phase, and a set of *activity-composition models* describing the distribution of elements on mineralogical sites for various phases that exhibit solid solution behaviour. The calculation of phase diagrams in THERMOCALC is based upon the solutions to non-linear equilibrium relationships – where these relationships represent balanced chemical reactions between end-members of phases. Equilibrium mineral assemblages are constrained from a given

bulk-rock composition and are mapped as a function of pressure and temperature (*P–T*), pressure and composition (*P–X*), and/or temperature and composition (*T–X*). Fe_2O_3 (oxidation state) is an uncertain variable pertaining to the bulk-rock composition (Johnson & White, 2011) and is typically constrained through the construction of *T–Mo* and *P–Mo* phase diagrams. If Electron Probe Micro Analysis data has been acquired, the oxidation state may also be more accurately constrained through the analysis of Fe^{3+}/Fe^{2+} ratios in minerals containing non-trivial cation proportions of Fe^{3+}. The user is required to first specify the equilibrium mineral assemblage and to then manually calculate equilibria relationships. The equilibrium mineral assemblage may be broadly defined by performing an initial Gibbs free energy minimisation calculation where either pressure, temperature or composition is held constant. Equilibria relationships are calculated as lines (where the modal proportion of one phase equals zero) and points (where the modal proportion of two phases equals zero). To successfully determine where new phases appear in *P–T–X* space, the user must make inferences based upon the rock's petrographical features and composition. Valid 'starting guesses' (i.e. compositional variables for phases) are frequently updated to ensure calculations are successfully completed in different areas of *P–T–X* space. Ultimately, a semi-quantitative graphical model is produced, comprising the stable mineral assemblages, field boundaries and points in a given *P–T–X* domain.

Method for Garnet Core Composition Removal from Bulk-Rock Composition

Sample T06-20: to ensure that the bulk-rock composition inputted into THERMOCALC best approximates the composition that constitutes the majority of the sample in terms of equilibrium volume, the average composition of garnet cores was removed from the original bulk-rock geochemistry. The following steps detail the procedure:

1. Mineral Liberation Analysis (MLA) mapping was undertaken with an FEI Quanta MLA–600 scanning electron microscope to help identify different minerals and mineral textures within the sample.
2. Using the image processing software *Photoshop*, the proportion of garnet in the sample was estimated through the process of 'pixel counting' – this process entails the use of the *histogram* feature where all the pixels in a given image are plotted as a function of each colour intensity level. Pixels contributing to garnet in the image were simply divided by the total number of pixels in the image to obtain the proportion of garnet in the sample.
3. Elemental X-ray maps in Ca and Mg for a single garnet porphyroblast were obtained using the CAMECA SXFive electron microprobe at Adelaide Microscopy. These maps were used in *Photoshop* to determine the number of pixels contributing to the garnet core. Normalising to the number of pixels in the entire garnet porphyroblast, the proportion of garnet core relative to the entire garnet was calculated.
4. Electron probe micro analyses across the length of the garnet core were averaged to obtain a representative garnet core composition in oxide wt%.
5. Mineral end-member proportions for all solid solution minerals in the sample – calculated from mineral composition analyses – were used to determine the density of all minerals in the sample. The density values for individual minerals were adjusted to reflect the density contribution of each mineral based on their modal proportions in the sample. An average rock density was calculated from the adjusted densities of all minerals.

6. The following calculation was implemented to give the final garnet core composition:

$$Garnet\ Core\ Composition\ (wt\%)$$

$$\times$$

$$\left(Garnet\ Core\ Modal\ Proportion \times \left(\frac{Garnet\ Density}{Sample\ Density}\right)\right)$$

7. The calculated garnet core composition was subtracted from the original bulk-rock composition and was subsequently inputted into THERMOCALC.

APPENDIX 1d: Extended LA–ICP–MS Zr-in-Rutile Thermometry Methods

Temperature estimates were calculated based on Zr concentrations (in ppm) following Tomkins *et al*. (2007):

$$T(°C) = \frac{83.9 + 0.410P}{0.1428 - Rln\emptyset} - 273 \quad where\ \emptyset = Zr\ (ppm), P = pressure\ (kbar) \qquad (1)$$

Rutile grains (ca. 50–100 μm) from sample T01-40 that were mounted in epoxy resin and polished, were first separated using both washing and magnetic separation techniques. The mounted rutile grains were subsequently imaged using a back-scattered electron (BSE) detector coupled with an FEI Quanta MLA–600 scanning electron microscope to identity any evidence of zirconium exsolution. The instrument maintained a beam operating voltage of 25 kV, a working distance of 10 mm and BSE photographs were imaged at a 400–X magnification. Although not the case in this study, zirconium concentrations in rutile that do exhibit zirconium exsolution can be corrected for by following the methods outlined by Pape *et al*., (2016). The remainder of rutile grains were analysed in-situ in samples T01-40 and T06-20. Those rutile grains that were included within garnet porphyroblasts were targeted to acquire temperatures best representative of

peak metamorphic conditions. The LA–ICP–MS instrument conditions used are as follows: 5 Hz laser repetition rate, 115 mJ operating energy and an operating voltage of 25 kV. The total acquisition time for each analysis was 70 seconds, encompassing 30 seconds of background measurement and a further 40 seconds of ablation. The primary standard used to account for downhole fractionation effects and instrument drift was NIST-610 (Zr = 448 ± 9 ppm, Ti = 452 ± 10 ppm); (Jochum *et al*., 2011). As with garnet rare-earth element analysis, GSD-1G was used as the secondary standard to monitor the accuracy of NIST-610. For GSD-1G trace element values, see Appendix 1b. In this study, NIST-610 yielded a Zr concentration of 448 ± 4.1 ppm (n = 14, 2σ errors) and GSD-1G, a Zr concentration of 39.7 ± 0.6 ppm (n = 35, 2σ errors).

Once again, data was processed using *Iolite* using the Trace_Element_IS DRS, following very similar procedures to those summarised in Appendix 1b. The internal element standard used for the unknowns in both samples was Ti (56.20 wt%) where the concentration value was derived from Electron Probe Micro Analyses of rutile. The most influential signal channels utilised in the data processing were ^{47}Ti, ^{90}Zr, ^{93}Nb and ^{29}Si (ppm). A large proportion of the signals were severely shortened, especially in sample T06-20, due to extraordinary variability in ^{29}Si with ablation time – a feature consistent with garnet contamination. This is problematic because garnets in sample T06-20 contain large quantities of Zr (Appendix 2e). A range of spot sizes (13 μm, 19 μm, 29 μm, 43 μm and 51 μm) were used in the analysis of rutile grains of variable size in both T01-40 and T06-20. To show that absolute Zr concentrations were not affected by the variable spot sizes, rather, the precision was affected, the following plot was constructed detailing Zr concentration as a function of different sized spots in the standard, GSD-1G (n = 35):

Zr-in-rutile temperature estimates for samples T01-40 and T06-20 were ascribed uncertainties of ca. 3.5% and ca. 4.4%, respectively. Uncertainties were calculated through the quadrature summation of relative errors inherent in the calculations following the methods of Walsh *et al*. (2015). Considered in the calculation: (i) the error associated with the pressure (± 1 kbar), (ii) the error implicit in the measurement of Zr concentrations (± 1.7% for T01-40 and ± 3.2% for T06-20), and (iii) the error accompanying the analytical calibration of the Zr-in-rutile thermometer (± 3%). Provided in Appendix 2h are the Zr-in-rutile results in their totality, including error calculations.

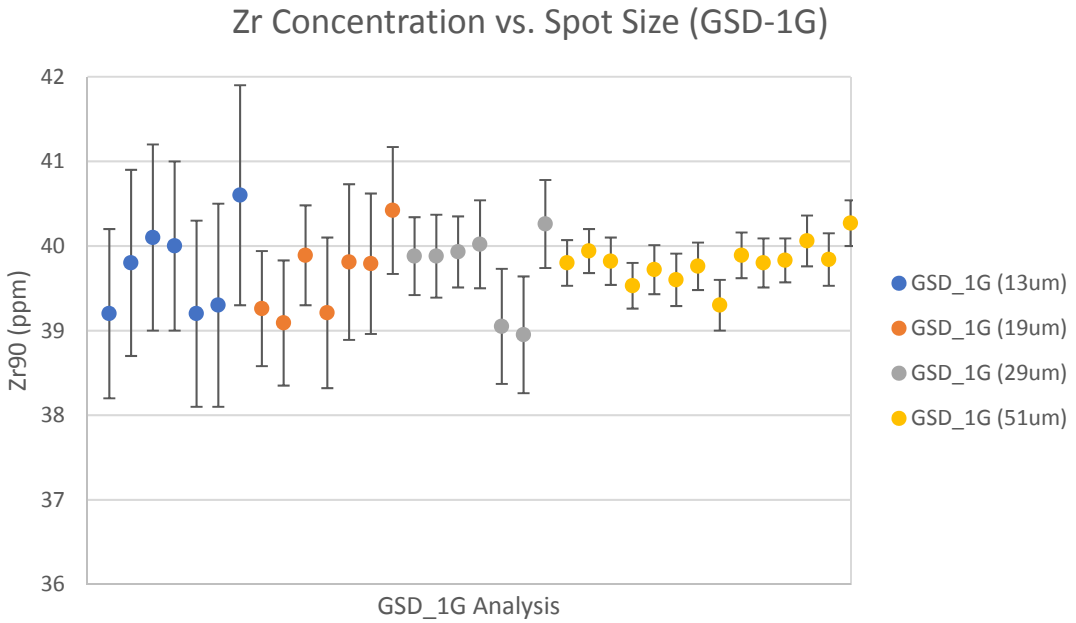

APPENDIX 1e: Extended Garnet-Orthopyroxene Thermometry Methods

The thermometer relies on the partitioning of Fe^{2+} and Mg^{2+} between coexisting garnet and orthopyroxene as described by the following exchange reaction:

$$(2)almandine + (3)enstatite = (2)pyrope + (3)ferrosilite \quad (2)$$

Temperature estimates were derived from the thermodynamic calculation program, THERMOCALC v.321. Mineral end-member activities were calculated from Electron

Probe Micro Analyses using the program, *A–X* (© Roger Powell and Tim Holland). Average garnet rim compositions and average matrix orthopyroxene compositions were selected for calculation purposes.

APPENDIX 1f: Modal Proportion Estimation Methods

Modal proportions for all minerals in samples T01-40, T06-20 and T06-30 were calculated using (i) Mineral Liberation Analysis (MLA) undertaken with an FEI Quanta MLA–600 scanning electron microscope, and (ii) the process of 'pixel counting' undertaken with *Photoshop*. Each thin-section sample was first imaged in plane-polarised light using a Nikon Eclipse LV100 Petrographic Microscope. From each image, areas were selected (typically equating to around a third of the total thin-section area) that were inferred to be representative of the entire sample. MLA maps were created from the representative areas for each sample, thereby providing a method by which to distinguish each mineral based on its assigned colour. MLA maps for each sample were loaded into *Photoshop* where 'pixel counting' was implemented to derive the relative proportions of each mineral. Samples T06-11 and T06-09 were not analysed using MLA. Consequently, the modal proportions of the identified minerals in each sample were estimated from their respective thin-section images which were interrogated using *Photoshop*.

APPENDIX 1g: Whole-Rock Chemistry Methods

The whole-rock chemical composition of sample T06-30 was acquired from Franklin & Marshall College, Lancaster, PA, U.S.A. A PANanalytical 2404 X-ray fluorescence vacuum spectrometer coupled with a PW2540 X–Y sample handler was used for the

analysis, which included both major and trace elements. Whole-rock chemical analyses for samples T06-20 and T01-40 were provided by Brick (2011).

APPENDIX 1h: Extended Clinopyroxene Compositional Reintegration

The following procedure describes the calculations pertaining to the compositional reintegration of the inferred precursor omphacite in retrogressed eclogite sample T01-40.

1. In order to estimate the amount of sodium (in oxide wt%) in the inferred clinopyroxene domain at peak conditions, modal proportions of the inferred peak minerals *garnet* + *omphacite* + *quartz* + *rutile* were estimated.
2. Peak *garnet* mode was estimated using the proportions of current garnet present in the sample and the surrounding plagioclase coronae. Here, it is assumed that the entire volume of garnet present at peak conditions is now occupied by the current garnet in the rock + the plagioclase coronae that surround garnet, as a consequence of decompression. Peak *omphacite* mode was estimated by adding the proportions of current diopside in the sample and the plagioclase present as intergrowths in diopside. The assumption here is that omphacite broke down to produce diopside and intergrown plagioclase. The current modal proportion of *quartz* present in the rock was used as a direct estimate of quartz present at peak conditions – quartz is inferred to be a part of peak assemblage based on its texture in the rock. The mode of peak *rutile* was estimated directly from the amount of ilmenite currently present in the sample. This is justified under the assumption that all rutile present at peak conditions subsequently broke down to form ilmenite.

3. The proportions of the inferred peak minerals were converted to concentrations (in wt%) by considering the respective mineral densities.
4. Using the current amount of sodium in the rock (Na_2O = 2.24 wt%), derived from the whole-rock geochemistry of sample T01-40, the sodium content in clinopyroxene[1] was calculated using the following equation:

$$Na_2O_{(whole-rock)} \times \left(\frac{100}{peak\ proportion_{cpx1}}\right)$$

5. The reintegrated Na_2O content in clinopyroxene[1] was supplemented into 15 EPMA-derived clinopyroxene compositional analyses from T01-40. As a result, 15 omphacite compositions (in oxide wt%) were obtained.

Although not typically regarded as a mineral species with respect to the strict definition, omphacite may be regarded as an intermediate composition in the solid solution series between pyroxene end-members, diopside (calcic) and jadeite (sodic). In THERMOCALC, the proportion of jadeite in omphacite is defined based on Al on the two M1 sites and Na on the two M2 sites. Given that (i) jadeite proportion is defined with respect to both Al and Na and thus (ii) the calculation of jadeite proportion is not influenced by the amount of Ca, Mg or Fe in omphacite, it is most reasonable to combine the reintegrated clinopyroxene Na_2O content in sample T01-40 with current, EPMA-derived clinopyroxene compositions to derive a set of reintegrated peak omphacite compositions.

APPENDIX 2a: Extended Petrography

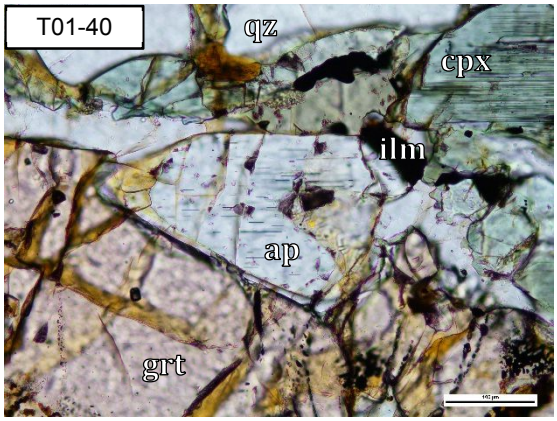

Apatite (ap) bordered by garnet (grt) and clinopyroxene (cpx)

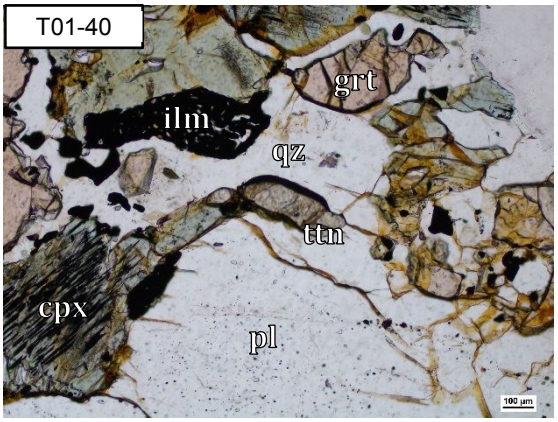

Titanite (ttn) associated with plagioclase (pl) and quartz (qz)

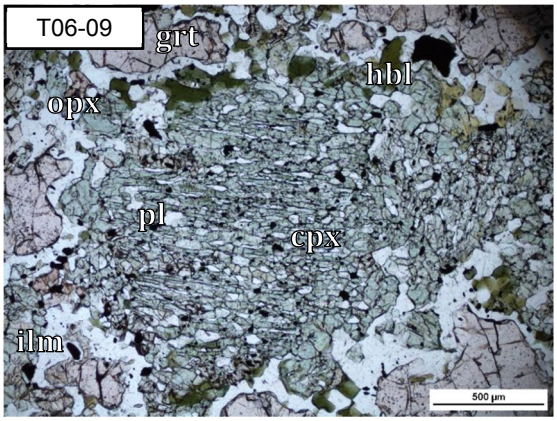

Clinopyroxene (cpx) with plagioclase (pl) intergrowths. Both hornblende (hbl) and orthopyroxene (opx) overprint its margin.

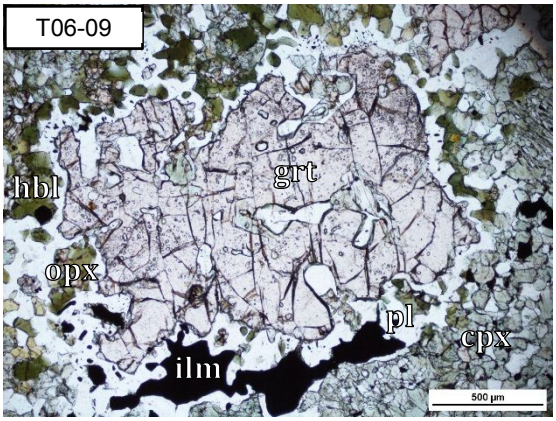

Porphyroblastic garnet (grt) separated from clinopyroxene (cpx) by a plagioclase (pl) corona.

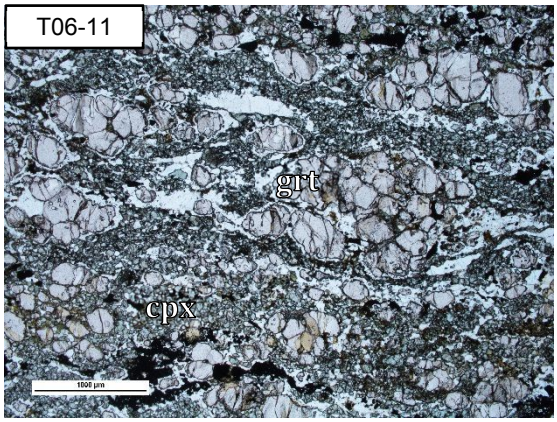

Distinct coarse-grained garnet (grt) domains layered amongst a clinopyroxene (cpx) fabric.

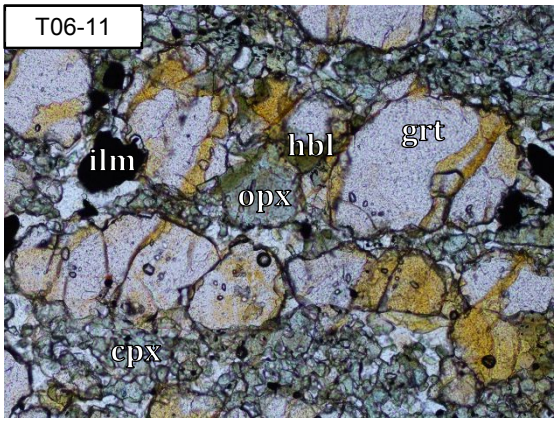

Intact orthopyroxene (opx) overprinted by hornblende (hbl).

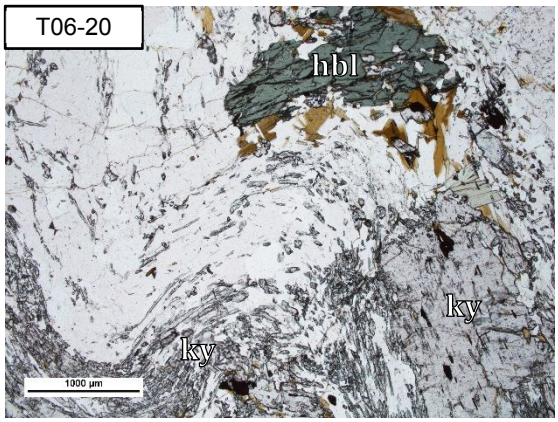

Microscale fold comprising a coarse-grained, reoriented hornblende porphyroblast (hbl), kyanite porphyroblast (ky) and fine-grained kyanite needles.

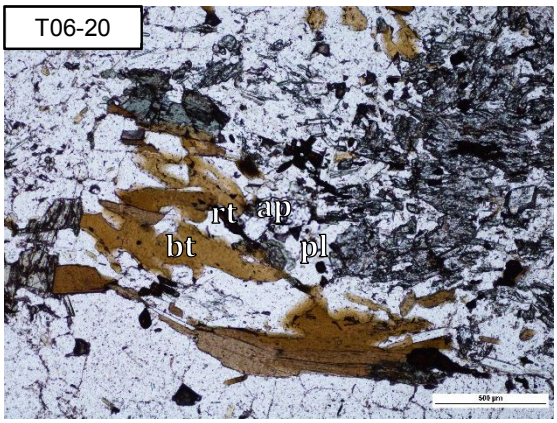

Matrix apatite (ap) – centre of photograph – bordered by plagioclase (pl), biotite (bt) and rutile (rt).

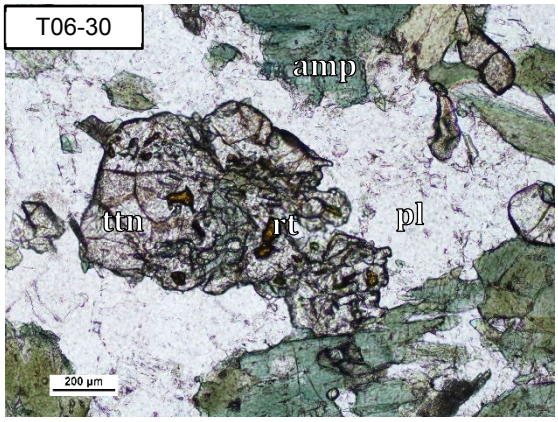

Rutile (rt) hosted by medium-grained titanite (ttn).

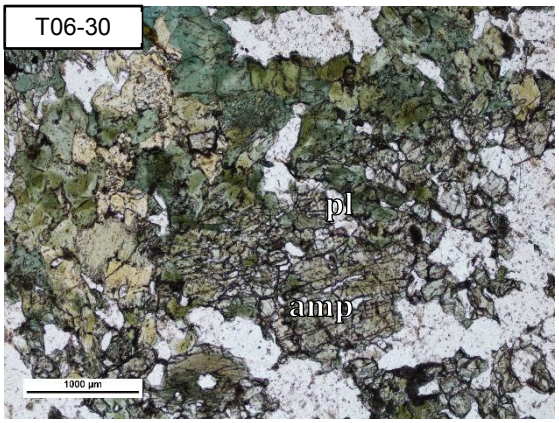

Anhedral amphibole (amp) with remnant plagioclase (pl) lamellae textures.

APPENDIX 2b: Brief Petrographic Descriptions of Samples T06-21, T06-21A, T06-27

Metapelitic samples T06-20, T06-21, T06-21A and T06-27 were all obtained from the same section of the Great Ruaha River, however, samples T06-21, 21A and 27 were only used in the U–Pb Rutile geochronology component of this study whereas T06-20 was incorporated into the wider scope of the study. All samples are very similar in both mineralogy and textural features and are considered to represent the same rock package.

T06-21 Metapelite

UTM Coordinates (WGS 84): 186492, 9208414

Kyanite and garnet are the dominant coarse-grained porphyroblasts and matrix minerals comprise plagioclase, quartz, rutile and hornblende. Late muscovite and chlorite, albeit minor in proportion, are also evident in association with kyanite porphyroblasts.

T06-21A Metapelite

UTM Coordinates (WGS 84): 186492, 9208414

As with T06-21, kyanite and garnet are the dominant coarse-grained porphyroblasts and matrix minerals comprise plagioclase, quartz, rutile and hornblende. Again, late muscovite is observed and pervasively overprints kyanite. Garnets in T06-21 are significantly larger than those in T06-21, with a diameter of 5-1.8 mm. Biotite strongly overprints garnet porphyroblasts.

T06-27 Metapelite

UTM Coordinates (WGS 84): 186225, 9208532

T06-27 is almost identical to T06-21A. The fabric comprising kyanite, biotite, plagioclase and quartz, however, is much more strongly developed.

APPENDIX 2c: Representative Electron Probe Micro Analyses

T01-40	Garnet Rim	Garnet Core	Diopside	Diopside-in-Garnet	Tschermakite	Tschermakite-in-Grt	Plagioclase	Plagioclase-in-Grt	Titanite
SiO2	37.61	37.11	52.23	51.59	42.00	39.94	61.35	60.16	29.60
TiO2	0.04	0.06	0.11	0.50	1.36	2.00	0.06	0.01	38.27
Al2O3	21.60	21.37	1.68	5.48	11.93	13.46	23.76	24.11	1.43
Cr2O3	0.03	0.00	0.02	0.04	0.00	0.00	0.00	0.00	0.00
FeO	25.94	27.06	8.84	9.07	15.44	15.17	0.18	0.43	0.53
MnO	1.21	2.52	0.10	0.05	0.07	0.03	0.00	0.00	0.01
MgO	4.73	3.36	13.43	11.40	11.18	10.59	0.01	0.01	0.00
ZnO	0.00	0.03	0.00	0.02	0.03	0.04	0.00	0.00	0.01
CaO	8.83	8.12	22.74	20.50	11.30	11.12	4.91	5.42	27.50
Na2O	0.03	0.02	0.75	1.55	2.21	2.20	9.15	8.71	0.01
K2O	0.00	0.01	0.01	0.00	0.24	1.02	0.01	0.04	0.00
Cl	0.00	0.01	0.00	0.00	0.13	0.13	0.00	0.00	0.02
F	0.00	0.00	0.00	0.00	0.02	0.08	0.00	0.02	0.39
Total	100.03	99.67	99.92	100.17	95.89	95.71	99.45	98.87	97.59
Cations									
Si	2.94	2.94	1.94	1.91	6.26	6.02	2.72	2.69	0.99
Ti	0.00	0.00	0.00	0.01	0.15	0.23	0.00	0.00	0.96
Al	1.99	2.00	0.07	0.24	2.10	2.39	1.24	1.27	0.06
Cr	0.00	0.00	0.00	0.00	0.00	0.00	0.00	0.00	0.00
Fe3+	0.13	0.11	0.09	0.03	0.85	0.75	0.00	0.00	0.01
Fe2+	1.56	1.68	0.18	0.26	1.07	1.16	0.01	0.02	0.00
Mn2+	0.08	0.17	0.00	0.00	0.01	0.00	0.00	0.00	0.00
Mg	0.55	0.40	0.74	0.63	2.49	2.38	0.00	0.00	0.00
Zn	0.00	0.00	0.00	0.00	0.00	0.00	0.00	0.00	0.00
Ca	0.74	0.69	0.91	0.81	1.81	1.79	0.23	0.26	0.98
Na	0.00	0.00	0.05	0.11	0.64	0.64	0.79	0.76	0.00
K	0.00	0.00	0.00	0.00	0.05	0.20	0.00	0.00	0.00
Cl	0.00	0.00	0.00	0.00	0.033	0.033	0.00	0.00	0.001
F	0.00	0.00	0.00	0.00	0.011	0.038	0.00	0.00	0.042
OH^-	0.00	0.00	0.00	0.00	0.000	0.000	0.00	0.00	0.000
Total Cations (S)	8.00	8.00	4.00	4.00	15.43	15.57	5.00	5.00	3.00

T06-11	Garnet Rim	Garnet Core	Diopside	Tschermakite	Plagioclase	Titanite
SiO2	37.21	36.38	50.31	42.75	56.68	28.47
TiO2	0.07	0.13	0.58	1.10	0.00	37.93
Al2O3	21.71	21.72	4.35	12.53	27.00	1.59
Cr2O3	0.07	0.00	0.13	0.13	0.00	0.03
FeO	23.14	22.31	7.15	13.10	0.23	0.70
MnO	0.72	0.71	0.08	0.04	0.00	0.03
MgO	5.39	5.71	13.45	13.07	0.00	0.00
ZnO	0.03	0.05	0.05	0.05	0.00	0.00
CaO	10.88	11.52	22.77	11.61	8.71	27.58
Na2O	0.05	0.02	0.76	1.68	6.88	0.01
K2O	0.00	0.00	0.01	1.26	0.12	0.00
Cl	0.00	0.01	0.02	0.07	0.00	0.00
F	0.00	0.00	0.00	0.18	0.00	0.50
Total	99.28	98.55	99.66	97.48	99.61	96.60
Cations						
Si	2.90	2.85	1.86	6.23	2.54	0.96
Ti	0.00	0.01	0.02	0.12	0.00	0.96
Al	1.99	2.00	0.19	2.15	1.43	0.06
Cr	0.00	0.00	0.00	0.01	0.00	0.00
Fe3+	0.20	0.29	0.10	0.80	0.09	0.04
Fe2+	1.30	1.17	0.12	0.80	0.00	0.00
Mn2+	0.05	0.05	0.00	0.00	0.00	0.00
Mg	0.63	0.67	0.74	2.84	0.00	0.00
Zn	0.00	0.00	0.00	0.01	0.00	0.00
Ca	0.91	0.97	0.90	1.81	0.42	1.00
Na	0.01	0.00	0.05	0.47	0.60	0.00
K	0.00	0.00	0.00	0.23	0.01	0.00
Cl	0.00	0.00	0.00	0.02	0.00	0.00
F	0.00	0.00	0.00	0.08	0.00	0.05
OH^-	0.00	0.00	0.00	0.00	0.00	0.00
Total Cations (S)	8.00	8.00	4.00	15.48	5.00	3.00

T06-09	Garnet Rim	Garnet Core	Diopside	Diopside-in-Garnet	Tschermakite	Plagioclase	Orthopyroxene
SiO2	36.96	36.55	52.05	50.25	42.66	59.54	51.39
TiO2	0.05	0.08	0.06	0.43	1.45	0.00	0.03
Al2O3	21.79	21.73	1.45	6.16	11.52	25.32	1.01
Cr2O3	0.01	0.01	0.01	0.02	0.07	0.00	0.00
FeO	24.29	23.99	10.26	7.78	16.12	0.17	26.19
MnO	0.53	0.58	0.12	0.05	0.06	0.00	0.27
MgO	6.67	6.68	13.47	12.46	10.64	0.00	20.54
ZnO	0.01	0.06	0.00	0.00	0.07	0.01	0.08
CaO	8.75	9.21	21.96	21.25	11.11	6.52	0.29
Na2O	0.00	0.03	0.55	1.12	2.09	8.28	0.00
K2O	0.00	0.00	0.01	0.00	0.22	0.05	0.00
Cl	0.00	0.01	0.00	0.00	0.72	0.00	0.01
F	0.00	0.00	0.00	0.00	0.00	0.00	0.00
Total	99.05	98.94	99.94	99.54	96.57	99.91	99.81
Cations							
Si	2.88	2.85	1.94	1.86	6.34	2.64	1.94
Ti	0.00	0.00	0.00	0.01	0.16	0.00	0.00
Al	2.00	1.99	0.06	0.27	2.02	1.32	0.04
Cr	0.00	0.00	0.00	0.00	0.01	0.00	0.00
Fe3+	0.24	0.31	0.09	0.06	0.81	0.11	0.06
Fe2+	1.34	1.26	0.23	0.18	1.20	0.00	0.76
Mn2+	0.04	0.04	0.00	0.00	0.01	0.00	0.01
Mg	0.77	0.78	0.75	0.69	2.36	0.00	1.16
Zn	0.00	0.00	0.00	0.00	0.01	0.00	0.00
Ca	0.73	0.77	0.88	0.84	1.77	0.31	0.01
Na	0.00	0.00	0.04	0.08	0.60	0.71	0.00
K	0.00	0.00	0.00	0.00	0.04	0.00	0.00
Cl	0.00	0.00	0.00	0.00	0.185	0.00	0.00
F	0.00	0.00	0.00	0.00	0.00	0.00	0.00
OH^-	0.00	0.00	0.00	0.00	0.00	0.00	0.00
Total Cations (S)	8.00	8.00	4.00	4.00	15.31	5.00	4.00

T06-20	Garnet Rim	Garnet Core	Tschermakite	Plagioclase	Staurolite-in-Garnet	Staurolite	Biotite	Muscovite	Chlorite
SiO2	37.48	37.77	40.80	58.76	26.08	26.69	37.68	44.71	23.89
TiO2	0.00	0.02	0.42	0.00	0.60	0.59	1.55	0.47	0.06
Al2O3	21.50	21.36	18.42	26.26	54.42	53.47	18.13	34.89	22.86
Cr2O3	0.03	0.01	0.08	0.01	0.28	0.32	0.20	0.10	0.15
FeO	32.77	30.51	15.52	0.11	11.88	11.96	14.52	1.17	17.23
MnO	0.65	0.23	0.04	0.02	0.04	0.01	0.01	0.00	0.00
MgO	5.29	4.44	8.22	0.00	1.95	2.17	13.64	0.92	19.47
ZnO	0.00	0.07	0.00	0.03	1.84	1.56	0.00	0.00	0.00
CaO	2.24	5.67	10.65	7.74	0.01	0.00	0.01	0.03	0.00
Na2O	0.01	0.01	1.87	7.60	0.07	0.04	0.29	1.65	0.00
K2O	0.00	0.00	0.50	0.04	0.01	0.00	9.00	8.56	0.00
Cl	0.01	0.00	0.55	0.00	0.00	0.00	0.27	0.01	0.04
F	0.00	0.00	0.08	0.00	0.00	0.02	0.07	0.01	0.00
Total	99.99	100.08	97.01	100.56	97.17	96.83	95.27	92.51	83.68
Cations									
Si	2.97	2.98	6.03	2.60	7.31	7.51	2.78	3.05	2.531
Ti	0.00	0.00	0.05	0.00	0.13	0.12	0.09	0.02	0.005
Al	2.01	1.99	3.21	1.37	17.97	17.72	1.58	2.80	2.853
Cr	0.00	0.00	0.01	0.00	0.06	0.07	0.01	0.01	0.012
Fe3+	0.06	0.06	0.40	0.00	0.13	0.00	0.04	0.01	0.058
Fe2+	2.11	1.96	1.52	0.00	2.65	2.81	0.85	0.06	1.468
Mn2+	0.04	0.02	0.00	0.00	0.01	0.00	0.00	0.00	0.000
Mg	0.62	0.52	1.81	0.00	0.82	0.91	1.50	0.09	3.074
Zn	0.00	0.00	0.00	0.00	0.38	0.32	0.00	0.00	0.000
Ca	0.19	0.48	1.69	0.37	0.00	0.00	0.00	0.00	0.000
Na	0.00	0.00	0.54	0.65	0.04	0.02	0.04	0.22	0.000
K	0.00	0.00	0.10	0.00	0.00	0.00	0.85	0.74	0.000
Cl	0.00	0.00	0.14	0.00	0.00	0.00	0.03	0.00	0.01
F	0.00	0.00	0.04	0.00	0.00	0.01	0.02	0.00	0.00
OH^-	0.00	0.00	0.00	0.00	4.00	3.99	1.95	2.00	7.99
Total Cations (S)	8.00	8.00	15.34	5.00	29.50	29.50	7.74	7.00	10.00

T06-30	Garnet Rim	Garnet Core	Tschermakite	Magnesio-hornblende	Plagioclase	Titanite
SiO2	39.34	39.24	41.35	48.42	45.76	30.67
TiO2	0.09	0.08	0.14	0.45	0.00	37.17
Al2O3	21.94	21.61	16.77	7.31	34.90	2.30
Cr2O3	0.03	0.04	0.07	0.03	0.02	0.02
FeO	20.56	21.22	15.08	11.99	0.26	0.31
MnO	0.34	0.62	0.16	0.16	0.01	0.00
MgO	9.74	9.13	9.48	14.29	0.00	0.01
ZnO	0.00	0.00	0.00	0.01	0.00	0.00
CaO	7.91	7.88	11.61	11.97	17.76	28.41
Na2O	0.01	0.01	1.99	0.98	1.46	0.00
K2O	0.00	0.00	0.32	0.16	0.01	0.00
Cl	0.01	0.00	0.35	0.16	0.01	0.00
F	0.01	0.00	0.07	0.07	0.00	0.24
Total	99.99	99.85	97.28	95.94	100.19	99.05
Cations						
Si	2.97	2.98	6.08	7.07	2.10	1.00
Ti	0.01	0.00	0.02	0.05	0.00	0.91
Al	1.96	1.94	2.91	1.26	1.89	0.09
Cr	0.00	0.00	0.01	0.00	0.00	0.00
Fe3+	0.08	0.08	0.55	0.40	0.00	0.00
Fe2+	1.22	1.27	1.30	1.06	0.01	0.01
Mn2+	0.02	0.04	0.02	0.02	0.00	0.00
Mg	1.10	1.04	2.08	3.11	0.00	0.00
Zn	0.00	0.00	0.00	0.00	0.00	0.00
Ca	0.64	0.64	1.83	1.87	0.87	0.99
Na	0.00	0.00	0.57	0.28	0.13	0.00
K	0.00	0.00	0.06	0.03	0.00	0.00
Cl	0.00	0.00	0.09	0.04	0.00	0.00
F	0.00	0.00	0.03	0.03	0.00	0.02
OH^-	0.00	0.00	0.00	0.00	0.00	0.00
Total Cations (S)	8.00	8.00	15.42	15.16	5.00	3.00

APPENDIX 2d: Extended Electron Probe Micro Analysis X-ray Elemental Concentration Maps

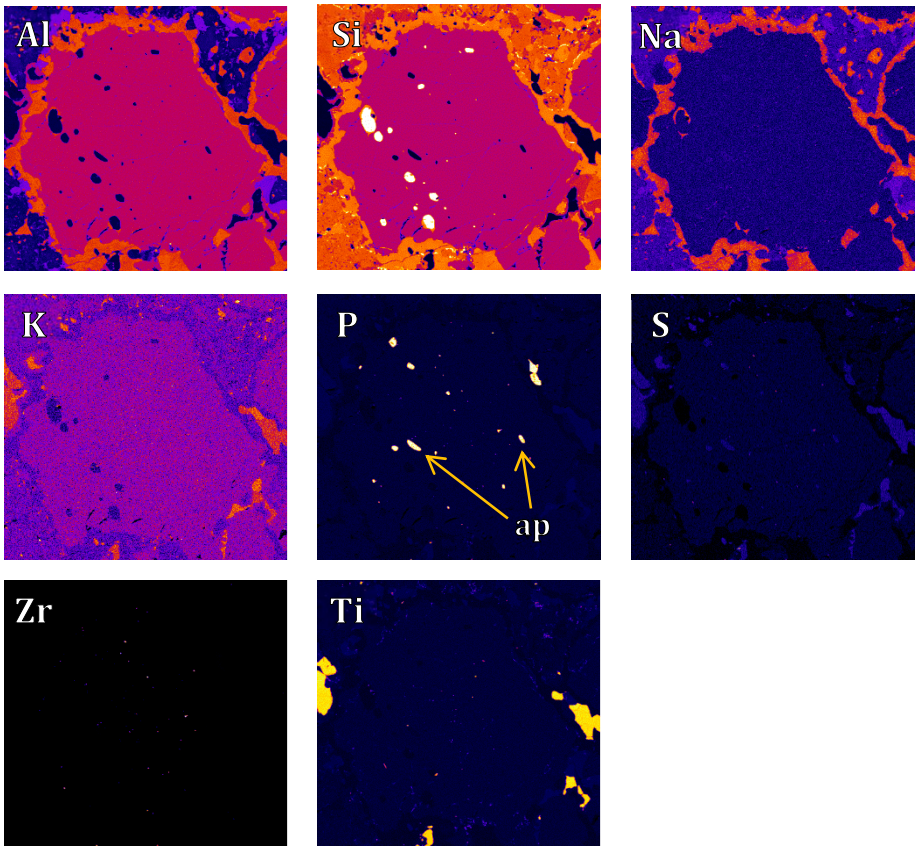

Garnet – Sample T01-40

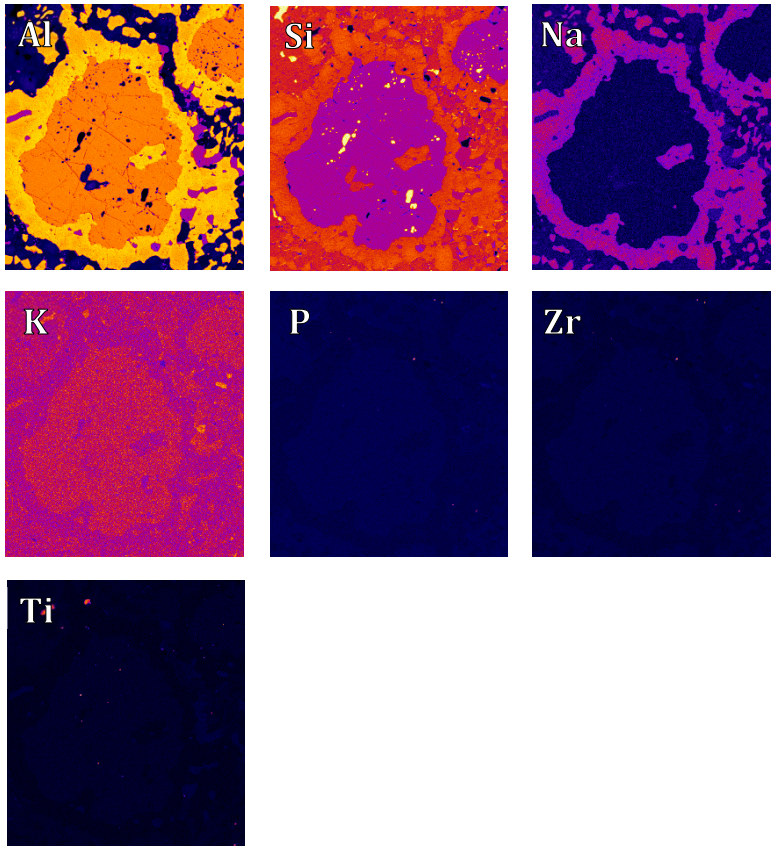

Garnet – Sample T06-09

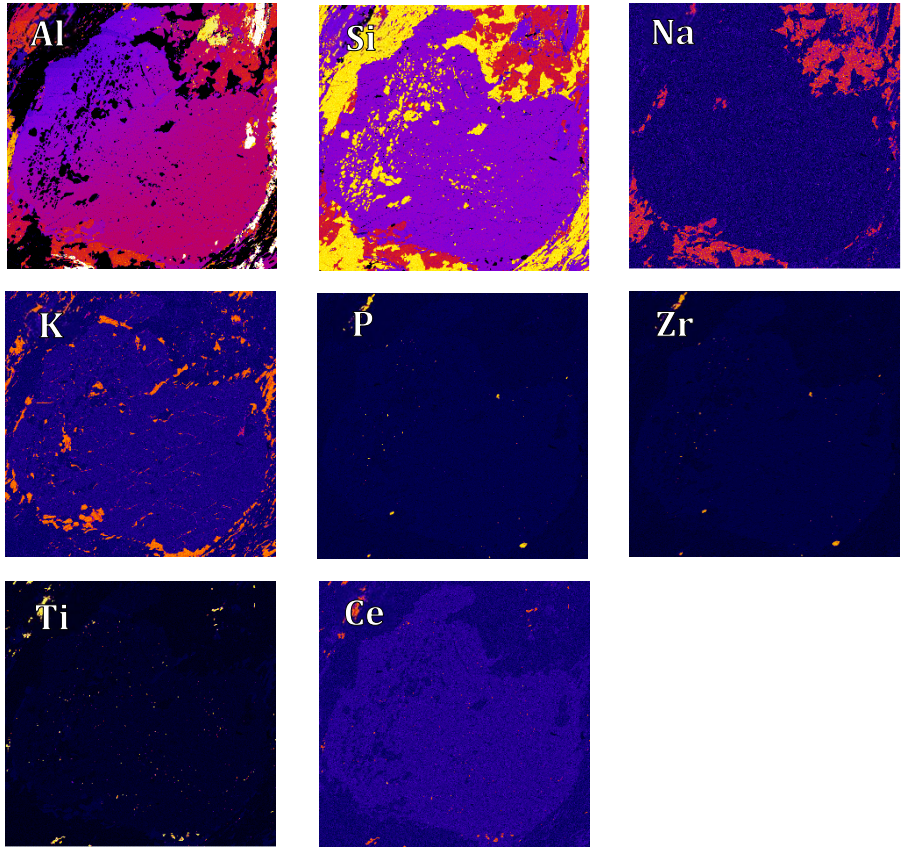

Garnet – Sample T06-20

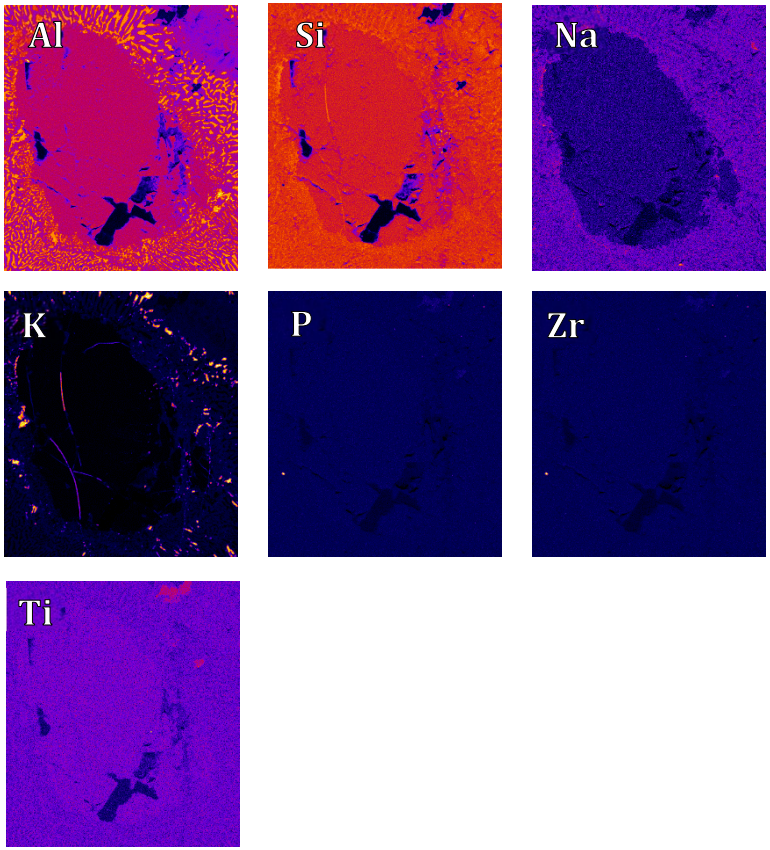

Garnet – Sample T06-30

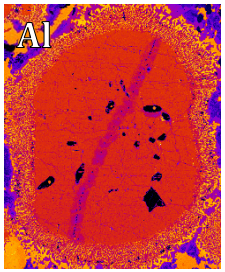

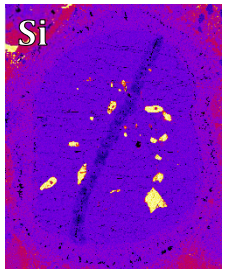

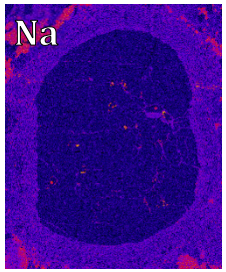

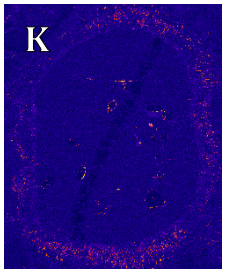

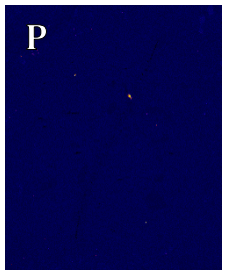

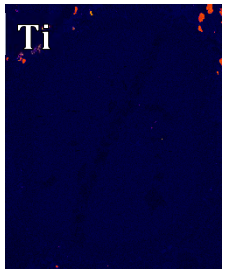

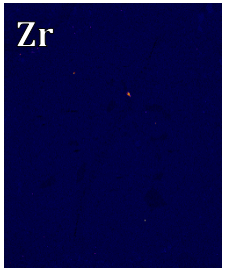

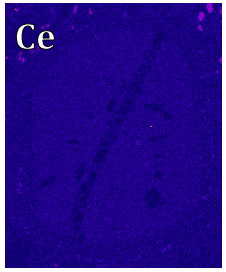

Coarse-grained Garnet – Sample T06-30

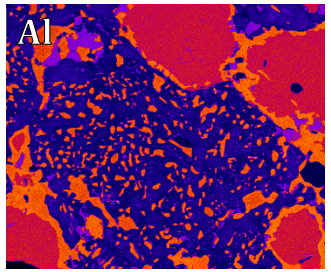

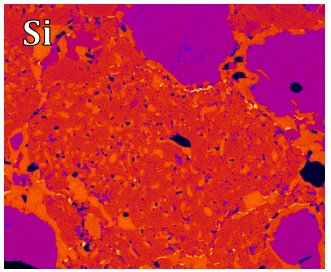

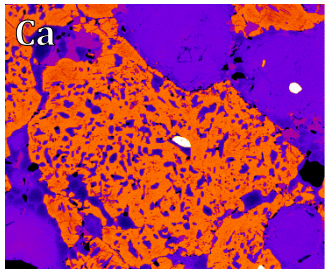

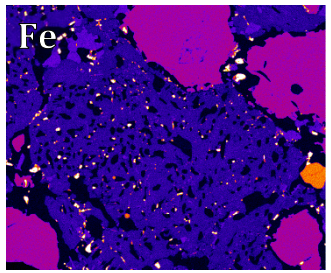

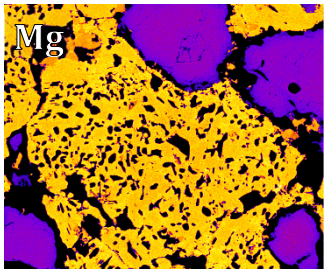

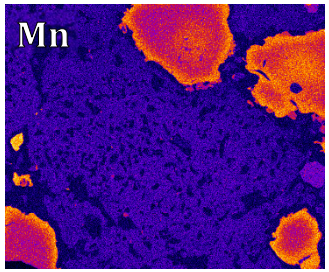

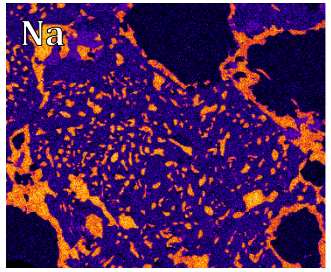

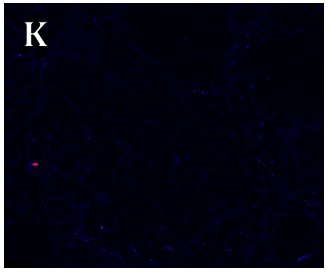

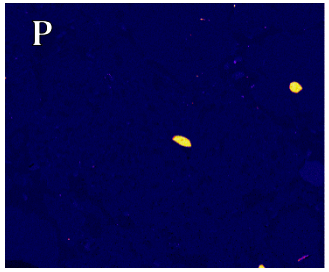

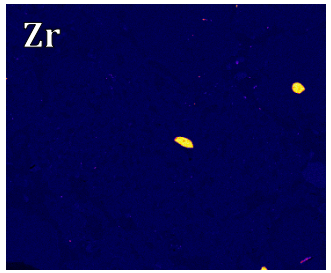

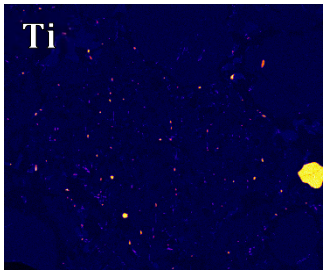

Clinopyroxene-plagioclase intergrowth textures – Sample T01-40

APPENDIX 2e: Extended LA–ICP–MS Garnet Rare-Earth Element Results

SESSION (A)															
Standard	**P**	**Y**	**Ce**	**Pr**	**Nd**	**Sm**	**Eu**	**Gd**	**Tb**	**Dy**	**Ho**	**Er**	**Tm**	**Yb**	**Lu**
GSD - 1	626	35.89	37.49	40.23	40.51	42.55	36.41	42.46	40.94	45.88	44.23	34.23	45.43	46.13	46.24
GSD - 2	648	37.12	38.07	40.13	41.2	43.5	36.42	43.1	41.43	46.53	45.19	34.9	46.39	46.72	46.76
GSD - 3	626	36.14	37.73	40.31	40.44	43.6	36.5	42.68	41.56	46.85	44.25	34.55	45.73	46.28	46.22
GSD - 4	640	36.48	37.79	40.16	40.4	43.7	36	42.4	41.66	46.6	44.21	34.35	45.76	46.52	46.12
GSD - 5	649	36.17	38.14	40.82	40.37	43.01	36.47	42.18	41.54	47.11	44.04	34.38	45.83	46.5	46.56
GSD - 6	684	37.23	38.5	40.2	40.2	43.4	36.17	43	41.67	46.75	45.01	34.61	46.3	47.3	47.07
GSD - 7	647	36.5	38.26	40.9	40.42	43.31	36.55	42.79	41.19	46.79	44.37	34.59	46.01	46.58	46.59
GSD - 8	684	36.63	38.9	40.93	41.29	43.8	36.52	42.7	41.66	48	45	35.14	47.13	46.89	47.08
GSD - 9	656	35.83	38.08	40.27	40.15	43.44	35.82	42.42	40.52	45.5	43.53	33.75	45.1	45.46	45.82
GSD - 10	728	37.27	39.11	41	41	44.9	36.93	43.5	42.12	47.1	44.89	35.1	47.02	46.7	47.12
GSD - 19	660	36.26	38.61	40.83	40.29	44	36.26	43.2	40.81	46.36	43.99	34.62	45.8	46.2	46.03
GSD - 20	684	35.07	36.86	38.8	38	42.4	34.7	41.1	38.65	44.1	42.39	33.35	44.28	44.2	44.4
GSD - 21	662	36.92	39.26	41.8	41.55	44.79	37.31	43.87	41.8	46.87	44.85	35.34	46.58	47	47.2
GSD - 22	684	34.96	36.38	38.63	39	41.4	34.9	41.4	39.22	45.1	42.7	33.2	44.7	44.3	44.93
GSD - 23	718	36.96	39.49	41.83	41.61	44.28	37.47	44.1	41.92	47.36	44.97	35.17	46.79	47.2	47.78
GSD - 24	699	34.75	36.09	38.93	38	41.6	34.13	41.1	39.2	44.4	42.24	33.55	44.3	44	44.82
GSD - 25	780	37.18	39.69	42.14	41.32	44.4	37.24	44.3	42.28	47.72	45.36	35.14	46.87	47.03	47.35
GSD - 26	767	34.54	36.3	38.8	38.6	40.5	34.2	40.6	38.47	43.5	42.36	32.7	43.3	43.8	43.9
GSD - 27	760	37.41	39.55	41.87	41.25	44.9	37.56	43.84	42.05	47.1	44.98	35.57	46.87	46.52	47.22
GSD - 28	717	34.45	36.05	38.4	38.2	40.4	33.83	39.9	38.63	43.4	41.74	32.28	43.1	44.2	43.7
GSD - 29	722	36.74	39.47	41.96	41.48	44	37.23	43.54	42.02	48	45.14	34.75	46.63	47	47.24
GSD - 30	719	34.3	36.04	38.59	37.9	41	34.65	40.8	38.76	45.1	41.94	32.57	43.46	43.5	43.8
GSD - 31	732	36.1	38.7	41.17	40.84	43.98	36.78	43.03	41.46	46.9	44.54	34.69	46.1	46.25	46.58
GSD - 32	695	34.2	36.8	39	38.2	41.5	33.98	40.7	39.09	44.6	43	33.19	44.4	45.1	44.17
GSD - 31	733	35.94	38.76	41.11	40.65	43.88	36.84	42.87	41.54	47	44.57	34.77	46.22	46.25	46.52
GSD - 32	696	34.08	36.8	39	38	41.4	34.03	40.6	39.16	44.7	43.1	33.26	44.5	45.2	44.12
GSD - 33	710	36.07	38.2	40.4	40.28	43.3	36.08	42.08	40.61	45.73	43.39	34.27	45.2	45.26	45.73

GSD - 34	739	34.99	36.78	38.88	38.8	41.5	34.69	40.9	38.96	45.03	42.2	32.59	43.79	43.9	44.67
GSD - 35	746	36.54	39.29	41.17	40.85	43.7	37.11	43.9	41.51	46.7	44.95	34.85	46.43	46.4	46.9
GSD - 36	742	34.96	36.7	39	37.7	41.5	35.1	41.9	39.5	44.7	42.5	33.1	44.4	44.4	44.6
GSD - 37	728	36.89	39.39	42.12	41.63	43.8	37.19	43.53	42.05	47.72	45.16	34.84	46.56	46.25	47.25
GSD - 38	706	35.53	37.22	38.79	38.9	41.5	35.38	41.7	39.55	45.1	43.29	32.48	44.9	44.5	45.1
GSD - 39	759	37.04	39.45	41.82	41.9	44.77	37.41	42.94	42.1	47.31	45.21	35.16	47.14	47.6	47.35
GSD - 40	724	34.78	36.1	38.52	38.3	40.7	34.75	41.3	38.8	43.4	42.4	32.8	43.38	44.7	45.1
GSD - 41	739	36.37	38.76	40.74	40.66	43.4	36.51	41.97	41.48	46.4	44.43	34.22	45.93	46.84	46.4
GSD - 42	716	34.31	36.51	38.11	38.7	40.8	34.6	40.6	38.97	44.3	42.44	32.87	43.21	43.9	44.04
NIST612 - 1	54.3	37.97	38.94	37.35	36.43	38.08	35.44	37.03	36.28	36.21	38.61	38.59	38.4	39.45	37.41
NIST612 - 2	52	38.13	38.61	37.21	35.58	38.15	34.87	36.72	35.87	36.05	38.04	38.04	37.84	39.31	36.89
NIST612 - 3	47	38.09	38.84	37.22	35.63	38.1	35.06	36.92	35.93	36.02	37.91	37.82	37.93	39.16	36.76
NIST612 - 4	50.1	38.16	38.32	36.77	35.75	38.02	34.73	35.88	35.73	35.56	37.31	37.21	37.54	38.65	36.14
NIST612 - 5	51.9	37.63	38.68	37.44	36.1	38.27	34.99	37.12	36.13	36.32	38.14	38.31	38.23	39.58	37.12
NIST612 - 6	50.2	37.99	38.64	37.19	36.01	38.04	34.76	36.17	35.85	35.84	37.77	37.76	37.78	39.12	36.75
NIST612 - 7	51.2	38.06	38.65	37.21	36.03	38.17	35.13	37.15	36.18	35.98	38.31	38.43	38.36	39.38	37.25
NIST612 - 8	49.4	38.04	38.63	37.17	35.79	37.94	34.97	36.45	35.94	36.04	37.84	37.84	37.82	38.84	36.54
NIST612 - 9	48	38.29	38.98	37.42	36.32	38.45	35.19	36.91	36.19	36.18	38.39	38.37	38.14	39.42	37.18
NIST612 - 10	57.1	37.81	38.58	36.94	35.48	37.84	34.92	36.46	35.72	35.84	37.67	37.69	37.77	39.24	36.7
NIST612 - 19	50.6	37.93	38.63	37.41	36.07	38.42	34.99	36.83	36.18	36.3	37.99	37.79	38.06	39.49	37.07
NIST612 - 20	49.3	38.19	38.8	37.14	36.04	38.1	35.03	36.89	36.07	36.09	38.21	37.98	38.08	39.69	36.79
NIST612 - 21	50.7	37.87	38.4	37.35	35.59	37.93	34.96	36.69	35.85	35.72	37.92	38.09	38.03	38.85	36.87
NIST612 - 22	55.7	38.02	38.59	37.05	35.54	38.06	34.88	36.46	35.74	35.84	37.83	38.26	37.9	39.22	36.66
NIST612 - 23	52.5	38.12	39.07	37.43	36.53	38.32	35.26	37.04	36.49	36.19	38.27	38.39	38.42	39.54	37.26
NIST612 - 24	47.6	37.76	38.47	36.85	35.55	37.98	34.78	36.26	35.58	35.55	37.72	37.76	37.68	38.68	36.8
NIST612 - 25	50	38.17	39	37.33	36.55	37.93	35.23	37.21	36.29	36.26	38.28	38.01	38.05	39.56	36.98
NIST612 - 26	48.8	38.18	38.92	37.19	35.77	38.05	35.14	36.41	35.94	35.93	37.91	38.04	37.83	39	36.76
NIST612 - 27	56.1	38.06	38.98	37.35	35.78	38.27	35	37.16	36.12	35.98	38.12	38.17	38.39	39.42	37.05
NIST612 - 28	47.4	37.56	38.33	36.96	35.75	37.74	34.66	36.05	35.61	35.84	37.51	37.83	37.61	38.73	36.63
NIST612 - 29	50.9	37.93	38.85	37.21	35.73	38.14	35.13	36.6	36.05	36.43	38.28	38.04	38.23	39.35	36.87
NIST612 - 30	52.7	37.97	38.39	37.09	35.77	38.22	34.75	36.65	35.76	35.69	37.61	37.72	37.69	39.51	36.65
NIST612 - 31	53	38.08	38.74	37.21	35.95	38.15	35.29	36.98	36.18	36	38.15	38.23	38.22	39.14	37.1

NIST612 - 32	48.9	38.21	38.69	37.34	36.18	38.25	34.97	36.93	36.12	36.15	38.01	37.99	38.09	39.26	37.02
NIST612 - 31	53.1	37.98	38.8	37.15	35.79	38.09	35.35	36.87	36.24	36.06	38.18	38.31	38.31	39.19	37.06
NIST612 - 32	49	38.14	38.75	37.28	36.01	38.2	35.04	36.83	36.19	36.21	38.04	38.07	38.19	39.34	36.98
NIST612 - 33	52.5	37.97	38.77	37.32	36.72	38.33	35.03	36.81	36.05	36.05	38.29	37.97	38.32	39.08	37.01
NIST612 - 34	51.8	37.86	38.43	36.97	35.51	37.82	34.48	36.36	35.46	35.73	37.36	37.51	37.45	39.07	36.44
NIST612 - 35	50.9	38.1	38.82	37.23	36.27	38.35	35.28	36.82	36.16	36.18	37.99	38.45	37.96	39.5	37.13
NIST612 - 36	48.2	37.81	38.31	36.82	34.9	37.64	34.63	36.49	35.67	35.43	37.81	37.46	37.68	38.76	36.49
NIST612 - 37	50.4	38.25	39.07	37.79	36.12	38.48	35.33	36.91	36.33	36.24	38.24	38.06	38.43	39.58	37.24
NIST612 - 38	48.6	37.95	38.74	37.13	35.83	38.15	34.84	36.57	35.92	35.97	37.91	38.1	37.96	39.2	36.81
NIST612 - 39	56.4	37.86	38.89	37.25	35.86	37.94	35	36.77	36.24	35.9	38.12	38.06	38.1	39.28	37.17
NIST612 - 40	49.8	38.11	38.81	37.33	36.17	37.99	35.04	36.88	36.06	35.78	37.87	37.87	37.98	38.78	36.77
NIST612 - 41	53.1	38.18	38.69	37.27	36.16	37.92	35.08	37.01	36.22	36.1	38.36	38.05	38.15	39.44	36.99
NIST612 - 42	47.8	37.84	38.42	36.92	35.57	38.51	34.96	36.29	35.71	36.2	37.7	38	37.86	39.09	36.58
Unknown															
T01-40 - 1	66	80.9	0.45	0.082	0.94	2.14	1.05	7.86	1.77	14.61	2.86	6.66	0.865	5.18	0.588
T01-40 - 2	107	92.6	0.7	0.108	0.91	1.83	0.95	6.35	1.65	14.7	3.53	10.12	1.08	4.99	0.582
T01-40 - 3	58	118.7	0.122	0.074	0.9	1.46	0.618	2.99	1.109	15.4	4.84	12.94	1.378	6.36	0.712
T01-40 - 4	52	132	0.085	0.053	0.82	1.04	0.489	2.44	0.848	14.98	4.96	15.1	1.783	9.6	1.147
T01-40 - 5	36	106.1	0.115	0.05	0.8	0.59	0.306	1.86	0.656	11.52	3.57	10.68	1.4	6.99	0.733
T01-40 - 6	44	97.7	0.096	0.061	0.92	0.91	0.313	1.58	0.572	9.94	3.43	10.48	1.307	6.8	0.795
T01-40 - 7	41	101.5	0.097	0.073	1.14	1.08	0.367	1.66	0.556	9.38	3.4	11.86	1.624	9.2	1.066
T01-40 - 8	50	95.2	0.163	0.1	0.79	1.01	0.272	1.26	0.368	7.14	3.28	14.41	2.26	13.25	1.68
T01-40 - 9	63	81.2	0.128	0.062	0.82	0.58	0.194	0.5	0.241	4.98	2.8	14.01	2.33	14.65	1.95
T01-40 - 10	48	70.5	0.146	0.07	0.93	0.56	0.172	0.3	0.169	3.92	2.33	12.76	2.57	17.21	2.34
T01-40 - 11	42	66.8	0.134	0.066	0.87	0.49	0.177	0.4	0.132	3.57	2.185	13.45	2.9	21.61	2.95
T01-40 - 12	38	63.7	0.15	0.077	0.93	0.49	0.163	-	0.131	3.17	2.04	13.25	3.03	22.81	3.26
T01-40 - 13	46	60.5	0.117	0.093	1.17	0.54	0.246	0.52	0.133	3.18	1.86	12.38	2.87	21.9	3.06
T01-40 - 14	57	65.7	0.113	0.065	1.07	0.56	0.171	0.39	0.135	3.27	1.93	12.97	3.12	24.63	3.53
T01-40 - 15	53	90.3	0.096	0.057	1.24	0.89	0.254	0.52	0.161	4.36	2.76	18	4.57	39.6	5.88
T01-40 - 16	57	103.7	0.143	0.068	1.09	0.79	0.303	0.51	0.229	4.87	3.11	21.7	5.49	49.8	7.35
T01-40 - 17	35	148.4	0.069	0.091	1.06	0.92	0.43	1.13	0.254	7.48	4.79	39.2	10.83	97.5	17.98
T01-40 - 18	49	179.4	0.101	0.056	1.21	1.37	0.452	1.15	0.356	8.27	5.89	48.7	13.86	138.1	25.04

T01-40 - 19	42	191.3	0.1	0.08	1.34	1.38	0.588	1.42	0.413	9.06	6.36	52.4	15.58	169.7	33.17
T01-40 - 20	37	179.1	0.138	0.083	1.37	1.83	-	1.65	0.41	8.86	6.21	48.1	14.31	156.5	30.9
T01-40 - 21	34	163.2	0.2	0.049	1.44	1.59	0.64	1.98	0.428	7.42	5.13	41.2	12.94	153.4	33.7
T01-40 - 22	27	153.1	0.303	0.086	1.29	1.65	0.622	2.2	0.418	7.11	4.81	39	13.03	157.9	36
T01-40 - 23	51	156.3	0.094	0.048	1.39	2.01	0.74	2.13	0.454	7.5	4.75	39.9	13.59	178.9	42.5
T01-40 - 24	31	150.8	0.09	0.057	1.37	1.87	0.65	2.62	0.478	7.19	4.67	35.1	12.01	150.5	34.7
T01-40 - 25	38	155	0.107	0.055	1.35	1.85	0.759	2.4	0.527	7.74	4.77	38.3	12.3	149.1	32.6
T01-40 - 26	32	160.5	0.085	0.078	1.52	2.05	0.837	2.96	0.56	8.46	5.13	41.2	13.21	156.3	33.51
T01-40 - 27	-	155.2	0.064	0.049	1.38	2.13	0.81	2.91	0.526	8.33	5.03	39.3	12.24	141.3	29.58
T01-40 - 28	51	154.5	0.128	0.061	1.29	1.99	0.8	2.79	0.48	8.17	4.99	39.9	12.34	130.1	24.76
T01-40 - 29	45	150.5	0.121	0.08	1.45	2.11	0.86	2.82	0.463	8.18	4.78	38.7	11.47	124.2	24.06
T01-40 - 30	48	150.3	0.078	0.056	1.66	2.11	0.89	2.73	0.509	7.83	4.9	37.1	10.89	111.6	20.2
T01-40 - 31	45	142.5	0.105	0.091	1.54	1.98	0.95	2.65	0.469	7.46	4.55	34.1	9.31	89.9	15.2
T01-40 - 32	52	127.3	0.126	0.085	1.49	2.15	0.81	2.91	0.461	6.94	4.15	29.65	8.04	72.6	11.57
T01-40 - 33	43	103	0.095	0.074	1.87	1.85	0.682	2.06	0.397	5.75	3.3	22.63	5.86	52.7	8.07
T01-40 - 34	44	80.9	0.085	0.106	1.74	2.13	0.65	2.11	0.317	5.15	2.58	18.3	4.63	39.3	5.98
T01-40 - 35	32	68.3	0.103	0.1	1.74	1.64	0.519	1.12	0.204	3.47	2.09	14.68	3.75	31	4.49
T01-40 - 36	45	70.3	0.133	0.088	1.12	1.18	0.353	0.8	0.138	3.33	2.32	16	3.64	28.81	4.31
T01-40 - 37	42	74.4	0.123	0.096	1.7	1.42	0.39	0.89	0.199	4.21	2.46	16.03	3.44	26.9	3.87
T01-40 - 38	82	79.1	0.208	0.099	1.45	1.15	0.281	0.85	0.203	4.05	2.61	15.8	3.2	23	3.22
T01-40 - 39	58	88.3	0.116	0.083	1.08	0.76	0.292	0.58	0.23	5.32	2.94	14.97	2.61	17.31	2.3
T01-40 - 40	48	105.6	0.134	0.074	0.96	0.99	-	1.39	0.563	9.7	3.63	13.76	1.95	11.89	1.62
T01-40 - 41	44	118.6	0.093	0.057	0.47	0.407	-	1.08	0.634	11.25	4.15	14.78	2.216	12.71	1.551
T01-40 - 42	60	134.5	0.133	0.05	0.4	0.45	-	1.39	0.74	13.74	5.27	17.4	2.32	12.3	1.54
T01-40 - 43	29	131.5	0.109	0.051	0.561	0.58	-	1.94	0.847	14.98	5.12	15.96	2	10.06	1.127
T01-40 - 44	45	71.1	0.075	0.045	1.15	2.24	1.07	5.86	1.39	11.77	2.68	7.2	0.834	4.15	0.487
T01-40 - 45	45	84.9	0.104	0.039	0.83	2.32	1.19	7.29	1.66	14.09	3.01	7.86	0.948	5.67	0.663
T01-40(2) - 1	68	63.4	0.59	0.117	1.01	1.91	0.96	7.55	1.792	13.91	2.43	4.71	0.53	2.95	0.331
T01-40(2) - 2	-	45.5	0.071	0.045	0.87	2.1	1.18	6.54	1.433	10.44	1.86	3.51	0.356	1.7	0.194
T01-40(2) - 3	36	59	0.079	0.041	0.86	1.73	0.76	4.04	1.022	9.56	2.25	4.89	0.544	2.46	0.261
T01-40(2) - 4	-	67.8	0.064	0.069	0.97	1.5	0.607	3.21	0.899	9.68	2.33	5.48	0.634	3.09	0.326
T01-40(2) - 5	44	85.1	0.088	0.065	1.08	1.13	0.38	1.74	0.577	9.42	2.94	10.08	1.329	7.3	0.854

T01-40(2) - 6	54	99.5	0.112	0.054	1.02	1.26	0.463	1.68	0.532	9.21	3.74	13.45	2.16	11.86	1.54
T01-40(2) - 7	-	97.2	0.102	0.072	1.12	1.19	0.376	1.58	0.367	7.81	3.52	15.82	2.69	17.3	2.44
T01-40(2) - 8	62	81	0.139	0.077	0.93	0.75	-	0.75	0.281	5.06	2.75	15.66	2.98	21.05	3.33
T01-40(2) - 9	40	75.5	0.114	0.064	1.73	1.92	0.693	2.54	0.432	5.49	2.54	14.4	2.94	22.33	3.34
T01-40(2) - 10	35	72.2	0.254	0.096	1.69	1.53	0.645	2.33	0.391	5.25	2.5	14.03	2.95	23.15	3.58
T01-40(2) - 11	182	75.7	0.59	0.139	1.92	2.06	0.75	2.42	0.458	5.48	2.67	15.38	3.35	24.8	3.66
T01-40(2) - 12	36	67.8	0.095	0.081	1.61	1.79	0.542	1.78	0.34	4.45	2.36	13.98	3.32	26.1	3.89
T01-40(2) - 13	54	61.9	0.115	0.073	1.41	1.2	0.355	1.03	0.184	3.73	1.98	14.26	3.58	30.1	4.89
T01-40(2) - 14	53	69.8	0.17	0.085	1.51	1.24	0.379	1.21	0.273	4.45	2.28	15.39	4.15	36.3	5.84
T01-40(2) - 15	50	96	0.083	0.059	1.55	1.01	-	1.63	0.412	6.28	3.23	21	5.5	48.9	8.03
T01-40(2) - 16	47	118.7	0.112	0.071	1.13	1.19	0.448	1.82	0.466	8.09	3.94	26.29	6.53	59.6	9.29
T01-40(2) - 17	42	138.1	0.115	0.08	1.17	1.14	0.321	1.55	0.419	8.06	4.66	30.1	7.99	75.4	12.24
T01-40(2) - 18	43	167.8	0.138	0.059	1.14	1.01	0.344	1.26	0.415	8.38	5.73	43.5	11.81	113.5	20.11
T01-40(2) - 19	54	182.2	0.105	0.073	1.39	0.92	0.346	1.05	0.38	8.89	6.27	47.2	13.39	132.2	23.82
T01-40(2) - 20	54	184.6	0.111	0.07	1.14	1.1	0.342	1.12	0.406	9.09	6.24	46.8	13.3	131.3	23.39
T01-40(2) - 21	80	177.9	0.316	0.082	1.42	1.11	0.366	1.05	0.306	8.51	6.07	46.1	13.15	128.8	22.9
T01-40(2) - 22	103	173.1	0.41	0.109	1.42	1.04	0.346	1.03	0.34	8.47	5.98	44.3	12.44	120.9	21.23
T01-40(2) - 23	38	165	0.139	0.059	1.32	1.13	0.42	1.36	0.307	8.11	5.52	42.5	11.2	112.3	19.49
T01-40(2) - 24	50	132.5	0.144	0.071	1.18	1.16	0.395	1.06	0.267	6.41	4.54	32.78	9	84.2	14.14
T01-40(2) - 25	33	110.9	0.107	0.047	1.35	1.2	0.37	1.27	0.266	5.68	3.68	28.1	7.67	70.6	11.67
T01-40(2) - 26	45	85.5	0.087	0.064	1.23	1.11	0.364	0.88	0.232	3.94	2.79	20.49	5.53	50.9	8.54
T01-40(2) - 27	45	64	0.103	0.072	1.32	1.13	0.377	0.83	0.178	3.27	2.02	14.33	3.49	32.7	5.23
T01-40(2) - 28	33	61.1	0.135	0.071	1.03	0.77	0.221	0.68	0.167	3.65	1.99	13.07	2.86	24.46	3.58
T01-40(2) - 29	45	64.9	0.152	0.069	0.72	0.57	-	0.48	0.157	3.54	2.106	13.19	2.86	21.7	3.09
T01-40(2) - 30	-	76.7	0.09	0.057	0.63	0.51	0.227	0.72	0.243	4.95	2.61	14.11	2.89	19.6	2.73
T01-40(2) - 31	49	92	0.073	0.032	0.4	0.311	-	0.77	0.475	9.02	3.52	12.12	1.76	10.08	1.195
T01-40(2) - 32	45	89.8	0.049	0.0162	0.233	0.219	-	1.03	0.547	9.55	3.06	9.31	1.146	6.15	0.713
T01-40(2) - 33	59	100.9	0.074	0.043	0.84	0.77	0.49	2.46	0.717	11.34	3.93	13.27	1.76	10.14	1.26
T01-40(2) - 34	39	96.9	0.1	0.043	0.97	1.25	0.565	2.87	0.795	11.51	3.82	12.49	1.62	9.46	1.155
T01-40(2) - 35	42	72	0.062	0.047	1	1.76	-	4.44	1.166	11.46	2.77	7.49	0.872	4.84	0.567
T01-40(2) - 36	38	51.8	0.053	0.025	0.88	2.19	1.05	6.73	1.389	10.39	1.99	4.79	0.478	2.92	0.344
T01-40(2) - 37	50	48.02	0.026	0.041	0.86	2.29	1.2	7.05	1.413	10.79	1.91	3.95	0.433	2.28	0.267

T06-20 - 1	65	280	-	-	0.112	0.96	0.414	8.12	3.64	45.2	12.15	32.9	3.76	19.3	2.43
T06-20 - 2	66	280.2	-	0.007	0.146	1.06	0.455	8.72	3.84	46.8	12.41	32.73	3.35	15.91	1.691
T06-20 - 3	59	319.2	-	-	0.111	0.95	0.414	8.07	3.65	46.63	13.58	42.14	5.41	31.3	4.17
T06-20 - 4	53	288.6	0.0044	0.0052	0.177	1.23	0.508	8.74	3.542	42.72	11.73	36.69	4.86	28.44	4.03
T06-20 - 5	46.3	221.3	0.0036	0.0102	0.202	1.38	0.532	9.14	3.3	36.1	8.49	23.33	3.04	18.12	2.247
T06-20 - 6	26	229.2	0.0143	0.0052	0.144	1.53	0.601	10.31	3.61	37.8	8.87	25.4	3.04	18	2.33
T06-20 - 7	37.6	199.9	0.0094	-	0.188	1.31	0.543	8.85	3.2	32.6	7.63	20.91	2.77	15.85	2.041
T06-20 - 8	41.8	188.6	0.0074	0.0051	0.162	1.3	0.534	9.2	3.42	32.8	7.22	19.25	2.342	14.37	1.708
T06-20 - 9	49	200.8	-	0.0067	0.13	0.92	0.455	8.81	3.5	34.08	7.84	21.59	2.845	15.87	2.038
T06-20 - 10	55	181.3	-	-	0.117	1.21	0.487	9.54	3.41	32.78	7.01	18.23	2.296	13.67	1.799
T06-20 - 11	37.9	166.9	-	-	0.242	1.37	0.533	10.68	3.48	30.51	6.4	17.04	2.324	13.32	1.795
T06-20 - 12	45.9	158.9	-	-	0.163	1.31	0.544	9.5	3.27	29.16	6.05	16.81	2.13	12.75	1.757
T06-20 - 13	41.1	165.3	-	0.0037	0.238	1.52	0.657	9.81	3.037	28.91	6.16	17.11	2.172	13.38	1.738
T06-20 - 14	49.5	176.5	0.0093	0.0059	0.175	1.58	0.621	9.86	3.26	29.84	6.65	18.38	2.291	14.03	1.818
T06-20 - 15	50	171.8	0.0042	0.0048	0.268	1.64	0.621	9.23	2.98	28.56	6.47	18.16	2.391	14.39	1.886
T06-20 - 16	47	147.3	0.247	0.103	0.72	1.77	0.638	8.44	2.613	24.32	5.45	15.11	2.028	12.74	1.798
T06-20 - 17	47.2	151.4	-	-	0.2	1.65	0.582	9.45	3.03	26.65	5.74	15.18	1.997	11.9	1.659
T06-20 - 18	37	139.5	0.005	0.015	0.229	1.79	0.73	10.41	3.02	27.6	5.31	13.64	1.62	10.52	1.48
T06-20 - 19	51	82.6	0.0081	0.0129	0.353	2.48	0.943	8.08	2.101	15.85	3.21	8.85	1.259	8.12	1.186
T06-20 - 20	47	69.8	0.02	0.0163	0.57	2.17	0.93	5.27	1.549	13.36	2.7	7.46	1.047	6.97	1.038
T06-20 - 21	41	78.8	0.0078	0.0088	0.398	1.81	0.746	5.7	1.774	15.06	2.97	8.96	1.305	9.36	1.32
T06-20 - 22	60	76.6	0.036	0.0168	0.342	1.21	0.616	4.5	1.53	13.8	2.94	8.73	1.359	8.95	1.231
T06-20 - 23	69	77.2	0.0158	0.0088	0.339	1.21	0.535	4.22	1.342	13.25	2.91	8.77	1.396	9.45	1.349
T06-20 - 24	53	81.3	0.0141	0.0179	0.366	1.14	0.516	4.15	1.495	13.89	3.15	9.82	1.577	10.34	1.403
T06-20 - 25	44.9	80.6	0.0094	0.0132	0.45	0.96	0.42	3.99	1.406	13.7	3.073	9.77	1.549	10.7	1.47
T06-20 - 26	75	77.6	0.0166	0.0166	0.35	0.65	0.326	3.66	1.425	13.35	3.05	9.3	1.401	9.44	1.306
T06-20 - 27	64	72.4	0.016	0.0176	0.65	0.6	0.263	3.59	1.427	13.04	2.54	7.45	1.108	7.07	0.91
T06-20 - 28	76	65.1	0.0097	0.0133	0.5	0.58	0.281	3.72	1.305	12.31	2.56	6.73	0.979	6.06	0.729
T06-20 - 29	49.9	63.56	0.0237	0.0191	0.579	0.71	0.331	3.47	1.281	12.11	2.412	6.73	0.93	6.05	0.878
T06-20 - 30	40	78.4	0.0156	0.0115	0.41	1	0.402	4.66	1.546	14.27	3.03	7.85	1.16	6.83	0.901
T06-20 - 31	64	86.2	0.031	0.036	0.68	1.12	0.524	4.13	1.58	14.34	3.15	8.36	1.118	6.93	0.974
T06-20 - 32	51.7	93.5	0.0302	0.038	0.644	0.93	0.488	3.67	1.517	15.66	3.53	9.51	1.128	7.33	0.988

T06-20 - 33	45	108.8	0.0203	0.0114	0.59	1.81	0.699	5.31	1.694	18.62	3.99	10.83	1.399	8.37	1.158
T06-20 - 34	42	113	0.0121	0.0184	0.413	1.78	0.839	5.72	1.889	19.44	4.32	10.98	1.372	8.51	1.05
T06-20 - 35	52	125.2	-	0.0069	0.345	1.66	0.781	7.05	2.273	22.01	4.71	12.2	1.472	9.22	1.097
T06-20 - 36	54	178.1	0.0082	0.0112	0.332	1.45	0.726	8.05	2.88	30.48	6.95	18.06	2.063	12.25	1.404
T06-20 - 37	40	180.5	0.053	0.0214	0.236	1.44	0.55	7.95	3.05	31.83	7.23	17.45	2.11	11.49	1.325
T06-20 - 38	61	197.6	0.0082	0.0067	0.196	1.35	0.564	7.97	2.95	32.86	7.62	19.93	2.359	12.48	1.432
T06-20 - 39	46	204.1	-	-	0.176	1.08	0.526	7.86	2.945	32.05	8.1	22.81	2.682	15.52	1.85
T06-20 - 40	41	235.4	-	0.0064	0.218	1.19	0.533	7.96	3.2	36.2	9.43	28.86	3.95	23.31	3.05
T06-20 - 41	51	290.7	0.0028	0.0012	0.198	0.94	0.453	8.23	3.45	42.2	12.44	40.6	5.55	32.58	4.35
T06-20 - 42	67	326	-	0.0054	0.167	1.04	0.467	8.41	3.86	48.4	14.11	42.37	5.19	27.77	3.45
T06-20 - 43	60	348.6	-	0.0034	0.16	1.13	0.467	8.99	3.99	53	15.12	43.8	5.18	25.98	3.125
T06-20 - 44	53	386.7	0.457	0.372	1.47	1.44	0.564	9.94	4.45	59.1	16.81	47.8	5.57	27.09	3.15
T06-20 - 45	53	367.9	0.0079	0.0107	0.176	1.11	0.516	10.02	4.48	57.1	15.96	45.54	5.01	24.75	2.89
T06-20 - 46	41	385.3	0.0093	0.0104	0.189	1.18	0.471	10.06	4.62	59.6	16.43	45.9	5.16	25.18	2.85
T06-20 - 47	47.9	361.4	0.0102	0.0079	0.236	1.26	0.523	10.51	4.62	57.2	15.53	43.2	4.74	23.03	2.58
T06-20 - 48	49	351	0.0087	0.0075	0.17	1.25	0.558	10.23	4.79	57.6	15.13	39.5	4.23	18.86	2.028
T06-20 - 49	50	331.4	0.0089	0.0089	0.329	1.41	0.58	10.8	4.67	56.1	13.77	35.13	3.51	15.51	1.566
T06-20 - 50	68	323	0.0071	0.0075	0.283	1.44	0.587	10.96	4.73	54.6	13.83	34.37	3.45	14.58	1.576
T06-20 - 51	59	316	0.0098	0.0068	0.213	1.34	0.547	11.2	4.71	54.3	13.63	34	3.38	14.71	1.48
T06-20 - 52	47	293	-	0.0082	0.249	1.11	0.443	8.67	3.99	49.6	12.46	32	3.33	16.5	1.871
T06-20 - 53	60.8	286	0.0074	0.0081	0.204	1.29	0.494	10.72	4.61	50.9	12.24	30.4	3.08	14.58	1.717
T06-20 - 54	59	267.6	0.32	0.0216	0.212	1.01	0.401	8.59	4.01	45.7	11.59	29.49	3.2	16.66	2.08
T06-20 - 55	69	272	0.0125	0.0065	0.155	1.09	0.496	10.25	4.42	49.4	11.77	29.34	3.042	15.67	1.992
T06-20 - 56	49	238	0.0091	-	0.047	0.322	0.179	4.87	2.78	36.7	10.15	29.9	4.05	24	3.32
T06-20(2) - 1	66	201.3	-	-	0.124	0.619	0.369	8	3.35	35.37	8.06	21.1	2.572	14.24	1.756
T06-20(2) - 2	53	242.8	-	-	0.103	0.74	0.325	7.36	3.37	38.68	10.08	30.3	4.13	26.44	3.82
T06-20(2) - 3	39.8	236.3	-	-	0.096	0.76	0.268	7.3	3.15	36.58	9.64	29.98	4.04	25.43	3.43
T06-20(2) - 4	44	252.3	-	0.0002	0.029	0.358	0.158	4.68	2.56	33.98	10.42	38.3	6.36	45.2	7.65
T06-20(2) - 5	42	256.8	0.0005	0.0001	0.142	0.72	0.393	7.4	3.28	37.4	10.39	34.2	5.08	31.9	4.56
T06-20(2) - 6	46	255.4	-	-	0.027	0.549	0.248	6.02	2.98	35.7	9.92	33.8	5.26	36.4	5.33
T06-20(2) - 7	36.2	245.9	-	-	-	0.287	0.15	4.18	2.24	30.9	9.8	35.8	5.89	38.8	5.59
T06-20(2) - 8	34.4	270.4	0.125	0.022	0.165	0.565	0.223	5.64	2.67	35.2	11.32	40.4	6.59	44	6.47

T06-20(2) - 9	36	236.3	0.116	0.0222	0.2	0.75	0.392	7.4	2.89	32.91	9.16	30.95	4.75	30.1	3.99
T06-20(2) - 10	47.9	245.4	0.0106	-	0.142	0.82	0.344	7.4	3.04	34.98	9.61	32.46	4.93	31.5	4.13
T06-20(2) - 11	42	296.5	0.028	-	0.022	0.195	0.102	4.6	2.88	38.9	12.04	43.8	7.06	46.5	6.13
T06-20(2) - 12	55	359	114	0.97	3.82	1.44	0.387	5.44	3.38	46.8	14.3	47.2	7.24	48.1	5.82
T06-20(2) - 13	54	237.5	6.2	0.067	0.43	0.85	0.343	7.3	2.96	34.2	9.35	31.4	4.72	30.3	4.35
T06-20(2) - 14	62	228.8	0.59	0.0101	0.223	0.95	0.391	7.47	2.89	31.7	8.82	28.36	4.02	24.93	3.107
T06-20(2) - 15	58	230.2	0.071	0.0088	0.1	0.55	0.261	6.18	2.532	32.18	9.26	33.49	5.21	35	5.07
T06-20(2) - 16	59	239.6	0.157	0.041	0.308	0.88	0.356	7.71	3.05	33.7	9.43	32.5	4.95	32.8	4.45
T06-20(2) - 17	37	271.3	0.05	-	0.084	0.46	0.18	5.09	2.51	34.7	10.99	40.6	6.54	47.1	6.55
T06-20(2) - 18	48	218.2	0.33	0.26	0.92	0.98	0.336	6.73	2.76	30.44	8.99	30.89	4.83	32.13	4.6
T06-20(2) - 19	45	229.7	-	-	0.114	0.67	0.297	6.84	2.87	32.9	9.33	32.2	4.95	31.8	4.26
T06-20(2) - 20	65	221	-	-	0.061	0.74	0.24	6.27	2.62	30.62	8.77	30.9	4.61	30.6	4.1
T06-20(2) - 21	51	222.2	-	0.0044	0.046	0.641	0.308	6.57	2.66	30.68	8.89	32.1	5.41	38.81	5.73
T06-20(2) - 22	60	222.7	-	-	0.077	0.73	0.301	6.62	2.68	31.44	8.89	30.76	4.89	32.28	4.56
T06-20(2) - 23	43	224.6	0.0071	0.004	0.114	0.95	0.326	7.27	2.87	31.3	8.8	28.7	4.364	25.52	3.01
T06-20(2) - 24	47	222.6	0.0059	0.0049	0.177	0.94	0.407	8.1	2.924	32.25	8.8	28.78	4.39	28.05	3.71
T06-20(2) - 25	-	274.1	0.031	-	0.042	0.25	0.153	4.59	2.92	37	11.37	37.2	5.77	39	5.38
T06-20(2) - 26	153	149	0.112	0.021	0.143	0.58	0.194	4.75	1.82	20.7	5.93	21.2	3.4	22.7	3.32
T06-20(2) - 27	68	118.6	0.0068	0.0039	0.178	1.1	0.505	7.59	2.245	21.37	4.73	14.01	2.05	13.19	1.855
T06-20(2) - 28	55	91	0.0073	0.0066	0.131	1.42	0.53	7.41	2.082	16.93	3.76	11.46	1.724	10.79	1.335
T06-20(2) - 29	57	99.3	0.0153	0.0062	0.209	1.26	0.495	7.71	2.175	18.71	4.14	12.52	1.888	12.01	1.634
T06-20(2) - 30	51	136.7	-	-	0.164	1.13	0.446	7.87	2.551	24.44	5.57	16.75	2.486	16.99	2.388
T06-20(2) - 31	46	213.2	-	-	0.108	0.85	0.378	7.37	2.94	31.9	8.43	28	4.13	26.8	3.65
T06-20(2) - 32	49	205.8	0.0274	0.0057	0.075	0.516	0.255	5.8	2.442	28.3	8.07	28.2	4.63	31.7	4.54
T06-20(2) - 33	59	183.3	-	0.0039	0.114	0.99	0.385	7.52	2.84	29.27	7.07	21.7	3.03	19.06	2.63
T06-20(2) - 34	55	182.1	0.0002	0.0067	0.145	0.84	0.324	7.48	2.92	29.87	7.13	20.94	2.84	16.34	2.197
T06-20(2) - 35	63	151.5	12.4	0.167	0.81	1.05	0.432	7.32	2.666	26.63	5.94	16	1.981	11.22	1.441
T06-20(2) - 36	73	96.8	0.031	0.0051	0.222	1.21	0.463	7.7	2.354	19.87	3.79	8.55	0.984	5.59	0.757
T06-20(2) - 37	82	55.34	1.18	0.0218	0.253	1.59	0.667	7.44	1.976	12.73	2.259	5	0.604	3.49	0.446
T06-20(2) - 38	67	39.31	0.0145	-	0.279	1.8	0.736	7.12	1.618	9.78	1.533	3.32	0.373	2.3	0.29
T06-20(2) - 39	74	34.23	0.0177	0.0062	0.328	2.06	0.75	7.1	1.673	9.37	1.356	2.73	0.346	1.8	0.241
T06-20(2) - 40	89	33.34	0.0105	0.0101	0.304	1.96	0.729	7.39	1.585	9.47	1.307	2.47	0.296	1.59	0.174

T06-20(2) - 41	72	38.5	0.0125	0.0055	0.323	1.9	0.821	7.86	1.87	11.03	1.484	2.89	0.288	1.69	0.17
T06-20(2) - 42	90	36.47	0.0121	-	0.178	1.85	0.702	8.38	1.894	11.12	1.358	2.59	0.267	1.28	0.144
T06-20(2) - 43	80	39.32	0.0069	0.0093	0.249	1.6	0.675	8.49	2.02	12.05	1.475	2.53	0.222	1.1	0.108
T06-20(2) - 44	67	53	0.0101	0.0126	0.265	1.77	0.726	9.13	2.325	15.44	2.048	3.35	0.287	1.31	0.153
T06-20(2) - 45	79	64.9	-	0.0138	0.251	1.87	0.633	9.38	2.52	17.18	2.4	4.56	0.418	1.75	0.194
T06-20(2) - 46	71	71.4	0.0051	0.0095	0.201	1.35	0.609	8.71	2.59	18.03	2.62	4.73	0.43	2.06	0.216
T06-20(2) - 47	54	85.8	-	0.0062	0.125	1.34	0.52	8.8	2.576	20.76	3.19	6.48	0.576	2.76	0.302
T06-20(2) - 48	38	100.8	0.0065	-	0.238	1.51	0.587	9.91	2.98	23.31	3.77	7.8	0.724	3.49	0.347
T06-20(2) - 49	33	113.7	-	-	0.114	1.1	0.522	9.13	3.07	25.36	4.48	9.21	0.876	3.86	0.435
T06-20(2) - 50	42	118	-	-	0.127	1.12	0.526	9.49	2.98	25.76	4.6	9.83	1.03	5.03	0.525
T06-20(2) - 51	32	126.3	-	-	0.164	1.33	0.538	9.34	3.15	27.9	5.01	10.68	1.067	5.26	0.631
T06-20(2) - 52	41	261	-	-	-	0.119	0.2	5	2.69	35.6	9.95	31	4.37	25.5	2.88
T06-30 - 1	54	32.64	0.0338	0.0237	0.59	1.01	0.455	3.32	0.883	6.75	1.348	2.98	0.325	1.51	0.15
T06-30 - 2	51	37.66	0.042	0.0246	0.507	0.93	0.475	3.74	0.939	7.54	1.468	3.68	0.418	1.84	0.185
T06-30 - 3	61	40.57	0.035	0.0327	0.62	0.98	0.507	3.62	0.925	7.69	1.584	3.92	0.465	2.31	0.212
T06-30 - 4	47.9	43.22	0.05	0.0199	0.518	0.99	0.489	3.22	0.932	8.28	1.735	4.48	0.525	2.55	0.232
T06-30 - 5	59	44.9	0.0332	0.0306	0.464	0.87	0.456	3.44	0.941	7.79	1.736	4.43	0.534	2.68	0.292
T06-30 - 6	72	47.1	0.053	0.028	0.541	0.892	0.477	3.6	0.957	8.45	1.793	4.86	0.597	2.93	0.291
T06-30 - 7	54	52.3	0.0439	0.0314	0.559	0.77	0.478	3.35	0.972	9.01	1.994	5.48	0.673	3.52	0.377
T06-30 - 8	62	58.2	0.047	0.0237	0.47	0.8	0.422	3.62	0.999	9.33	2.238	6.68	0.912	5.19	0.575
T06-30 - 9	55.1	61.1	0.0411	0.0275	0.579	0.78	0.418	3.52	1.014	9.57	2.318	6.89	0.989	5.48	0.675
T06-30 - 10	61	67.1	0.0273	0.0195	0.487	0.77	0.436	3.46	1.026	10.11	2.579	8.27	1.194	7.23	0.896
T06-30 - 11	60	72.4	0.0227	0.0203	0.419	0.92	0.436	3.68	1.112	11	2.78	8.73	1.272	7.72	0.958
T06-30 - 12	57	68.2	0.0198	0.018	0.347	0.8	0.446	3.54	1.039	9.97	2.635	7.87	1.059	6.55	0.807
T06-30 - 13	55	72.1	0.0115	0.0184	0.405	0.83	0.39	3.8	1.066	10.7	2.76	8.76	1.249	7.66	0.959
T06-30 - 14	62	73.9	0.0219	0.0127	0.378	0.819	0.419	3.52	1.081	11.13	2.797	8.65	1.257	7.57	0.916
T06-30 - 15	66	73.8	0.0147	0.0187	0.351	0.83	0.372	3.61	1.039	10.75	2.819	8.3	1.157	7.09	0.821
T06-30 - 16	55	73.6	0.0133	0.0126	0.319	0.83	0.396	3.6	1.065	10.43	2.663	8.32	1.154	6.57	0.784
T06-30 - 17	53	90.4	0.01	0.01	0.364	0.78	0.39	3.41	1.092	11.77	3.396	11.68	1.79	12.07	1.633
T06-30 - 18	58	104.9	0.0108	0.0106	0.314	0.79	0.386	3.56	1.078	13.21	4.03	15.52	2.677	20.81	3.16
T06-30 - 19	52	124.3	0.0209	0.0127	0.357	0.75	0.405	3.78	1.236	14.4	4.72	19.25	3.481	28	4.76
T06-30 - 20	55	134.3	0.0145	0.0159	0.306	0.75	0.422	3.84	1.254	15.03	5.12	21.1	4.07	33.87	5.59

T06-30 - 21	57	152.9	0.0115	0.0085	0.277	0.7	0.334	3.62	1.319	16.57	5.89	26.07	5.31	45.7	8.33
T06-30 - 22	54	154.5	0.0085	0.0145	0.305	0.82	0.376	4.02	1.348	16.91	5.71	25.16	5.07	43.7	7.79
T06-30 - 23	50	166.2	0.0156	0.0167	0.293	0.8	0.358	3.8	1.382	17.93	6.33	28.24	5.69	50.2	9.12
T06-30 - 24	61	164.4	-	0.0136	0.347	0.82	0.39	3.25	1.269	16.61	6.16	28.98	6.25	58.06	11.11
T06-30 - 25	40	175	0.0156	0.0112	0.4	0.83	0.403	3.77	1.306	17.38	6.46	30.5	6.51	59.7	11.19
T06-30 - 26	50	170.4	-	0.0147	0.391	0.84	0.418	3.45	1.328	18.05	6.48	30.12	6.15	56.8	10.69
T06-30 - 27	51	123.7	0.01	0.0145	0.325	0.85	0.429	3.69	1.118	13.83	4.57	21.14	4.25	36.98	6.86
T06-30 - 28	44	102.7	-	0.0161	0.33	0.87	0.416	3.58	1.144	12.95	3.89	14.98	2.538	19.26	3.025
T06-30 - 29	51	85.1	0.009	0.0077	0.318	0.9	0.412	3.5	1.094	11.33	3.09	10.55	1.637	10.83	1.332
T06-30 - 30	50	77.9	0.0075	0.0058	0.348	0.84	0.398	3.56	1.016	10.98	2.98	9.87	1.494	9.27	1.202
T06-30 - 31	53	76.4	0.0069	0.0148	0.353	0.81	0.418	3.45	1.019	11.15	2.96	9.37	1.337	8.33	1.066
T06-30 - 32	49	75.1	0.0094	0.0108	0.36	0.83	0.455	3.65	1.13	10.9	2.895	8.9	1.291	7.71	0.96
T06-30 - 33	60	74.4	0.0121	0.0159	0.414	0.84	0.426	3.38	1.088	11.01	2.85	9.11	1.24	7.8	1.001
T06-30 - 34	57	69.7	0.0109	0.0251	0.401	1.01	0.434	3.74	1.085	10.66	2.707	8.21	1.176	6.95	0.855
T06-30 - 35	51	68.2	0.0247	0.0238	0.43	0.83	0.358	3.35	1.034	9.96	2.566	8.15	1.093	6.5	0.83
T06-30 - 36	63	66.7	0.0212	0.02	0.49	0.94	0.393	3.77	1.028	10.03	2.471	8.03	1.129	6.92	0.839
T06-30 - 37	58	66.3	0.0209	0.0225	0.482	0.89	0.447	3.56	1.09	10.49	2.531	7.71	1.083	6.62	0.775
T06-30 - 38	63	65.5	0.0328	0.0233	0.433	0.84	0.472	3.63	1.102	10.37	2.666	7.91	1.071	6.42	0.766
T06-30 - 39	61	62.9	0.0369	0.018	0.433	0.93	0.427	3.84	1.044	9.99	2.457	7.32	0.989	5.48	0.695
T06-30 - 40	58	56.7	0.04	0.0314	0.442	0.83	0.454	3.61	0.97	9.13	2.148	6.23	0.754	4.32	0.515
T06-30 - 41	63	54.13	0.0397	0.0244	0.482	0.85	0.46	3.59	0.98	8.97	2.026	5.92	0.732	3.98	0.394
T06-30 - 42	59	50.7	0.032	0.0286	0.467	0.89	0.476	3.52	1.03	8.79	1.935	5.61	0.693	3.82	0.382
T06-30 - 43	57	49.7	0.031	0.0247	0.522	0.996	0.44	3.5	1.016	8.84	1.974	5.41	0.657	3.59	0.374
T06-30 - 44	75	45.6	0.0385	0.0318	0.503	0.98	0.472	3.59	0.885	8.14	1.815	4.72	0.569	2.86	0.308
T06-30 - 45	66	43.37	0.0443	0.0273	0.542	1.02	0.518	3.64	0.896	7.86	1.675	4.32	0.541	2.73	0.26
T06-30 - 46	54	39.4	0.048	0.0224	0.47	1.01	0.431	3.59	0.899	7.46	1.547	4.06	0.468	2.41	0.246
T06-30 - 47	63	32.8	0.04	0.0229	0.474	0.85	0.423	2.99	0.764	6.56	1.261	3.14	0.361	1.91	0.158
T06-30(2) - 1	55	69.9	0.0177	0.0189	0.405	0.85	0.418	3.56	1.028	10.42	2.59	7.79	1.059	5.87	0.658
T06-30(2) - 2	54	71.8	0.0271	0.0314	0.319	0.727	0.437	3.69	1.055	10.65	2.583	7.68	1.067	6.22	0.696
T06-30(2) - 3	49	73.9	0.0316	0.0229	0.454	0.92	0.44	3.5	1.099	11.05	2.83	8.57	1.169	7.08	0.825
T06-30(2) - 4	50	77.1	0.0235	0.0234	0.454	0.87	0.401	3.43	1.159	11.15	2.892	8.93	1.316	7.88	0.892
T06-30(2) - 5	55	77.5	0.0246	0.0208	0.451	0.75	0.467	3.6	1.076	11.17	2.9	9.3	1.379	8.04	1.011

T06-30(2) - 6	46.2	80.8	0.0168	0.0154	0.427	0.8	0.388	3.83	1.095	11.44	3.08	9.78	1.422	8.79	1.072
T06-30(2) - 7	47	84.5	0.0232	0.0261	0.378	0.8	0.417	3.54	1.125	11.46	3.13	10.14	1.467	9.14	1.098
T06-30(2) - 8	52.7	89.9	0.0193	0.019	0.442	0.77	0.402	3.56	1.123	12.04	3.3	10.93	1.68	10.85	1.394
T06-30(2) - 9	44	106.1	0.0165	0.02	0.424	0.84	0.41	3.36	1.207	13.18	3.92	14.45	2.396	18.18	2.71
T06-30(2) - 10	59	110.7	0.0167	0.0311	0.437	0.9	0.4	3.42	1.171	13.26	4.24	16.37	2.84	21.87	3.41
T06-30(2) - 11	45.5	116.5	0.0225	0.0167	0.429	0.7	0.44	3.64	1.181	13.39	4.28	17.9	3.19	24.67	4.2
T06-30(2) - 12	51	119.8	0.0181	0.0193	0.331	0.79	0.404	3.82	1.174	14.17	4.54	18.05	3.36	26.56	4.36
T06-30(2) - 13	57	122.7	0.0206	0.0178	0.419	0.96	0.407	3.6	1.237	14.61	4.64	19.29	3.5	28.08	4.67
T06-30(2) - 14	53	125.8	0.0096	0.022	0.438	0.69	0.413	3.78	1.253	15.13	4.95	19.92	3.83	30.11	5.01
T06-30(2) - 15	59	121.7	0.0173	0.015	0.414	0.89	0.409	3.49	1.159	14.32	4.93	20.22	3.79	30.68	5.26
T06-30(2) - 16	39	108	0.0193	0.0168	0.437	0.84	0.421	3.64	1.123	12.93	4.21	17.36	3.32	27.46	4.77
T06-30(2) - 17	39	118.1	0.0089	0.0196	0.464	0.84	0.414	3.87	1.194	13.81	4.52	19.37	3.86	32.84	5.7
T06-30(2) - 18	41	133.7	0.0116	0.0195	0.417	0.81	0.415	3.55	1.199	14.99	5.22	22.72	4.42	38.72	6.99
T06-30(2) - 19	46	134.9	0.0074	0.0233	0.41	0.86	0.397	3.48	1.281	15.38	5.21	23.61	4.61	40.8	7.49
T06-30(2) - 20	51	130.9	0.0098	0.0221	0.366	0.87	0.407	3.93	1.203	15.21	4.95	21.44	4.39	37.28	7.03
T06-30(2) - 21	45	146.9	0.0186	0.0183	0.396	0.91	0.403	3.56	1.296	15.93	5.7	23.89	4.68	40	6.89
T06-30(2) - 22	64	157.4	0.0134	0.0145	0.382	1.02	0.376	3.58	1.338	16.82	6.09	27.26	5.46	48.3	8.77
T06-30(2) - 23	62	154.2	0.0164	0.0112	0.345	0.91	0.424	3.7	1.298	16.59	6.19	28.73	5.91	52.8	10.41
T06-30(2) - 24	47	144.2	0.0082	0.021	0.441	0.95	0.423	3.9	1.309	16.46	5.56	22.92	4.3	36.1	6.05
T06-30(2) - 25	56	144.8	0.0088	0.02	0.395	0.83	0.424	3.58	1.311	15.67	5.49	24.46	4.8	41.22	7.26
T06-30(2) - 26	59	139.6	0.0135	0.0178	0.46	0.88	0.394	3.4	1.187	15.11	5.47	24.16	4.98	43.2	8.13
T06-30(2) - 27	43	113	0.0089	0.0141	0.466	0.91	0.426	3.5	1.18	13.6	4.2	16.29	3.15	26.1	4.37
T06-30(2) - 28	64	127.1	0.0136	0.0097	0.369	0.69	0.311	3.12	1.112	13.79	4.97	21.63	4.19	34.95	6.38
T06-30(2) - 29	43	118.5	0.0121	0.0213	0.355	0.67	0.359	3.39	1.159	13.76	4.37	17.97	3.45	26.92	4.52
T06-30(2) - 30	52	98.9	0.0056	0.0123	0.453	0.74	0.42	3.46	1.154	12.46	3.73	13.42	2.347	16.81	2.456
T06-30(2) - 31	51	88.7	0.0066	0.0178	0.417	0.64	0.384	3.56	1.044	11.65	3.43	11.5	1.742	12.25	1.651
T06-30(2) - 32	68	86.8	0.0145	0.0237	0.417	0.87	0.368	3.48	1.094	11.82	3.38	11.45	1.763	11.84	1.577
T06-30(2) - 33	60	80.1	0.0124	0.025	0.362	0.73	0.387	3.37	1.092	11.48	3.12	10.46	1.504	9.45	1.244
T06-30(2) - 34	62	80.5	0.0176	0.0171	0.426	0.72	0.402	3.47	1.056	11.42	3.07	10.03	1.487	9.15	1.263
T06-30(2) - 35	63	71.1	0.0128	0.0216	0.418	0.83	0.406	3.47	1.005	10.25	2.65	8.4	1.256	7.51	0.912
T06-30(2) - 36	50	64.7	0.034	0.033	0.48	0.89	0.38	3.25	1.004	9.72	2.518	7.4	1.019	6.26	0.767
T06-30(2) - 37	71	57.4	0.0355	0.0284	0.417	0.93	0.451	3.58	0.991	9.33	2.219	6.06	0.802	4.36	0.499

T06-30(2) - 38	49	52.4	0.0284	0.0258	0.455	0.94	0.393	3.38	0.97	8.93	2.058	5.43	0.704	3.55	0.376
T06-30(2) - 39	47.7	45.8	0.0344	0.0313	0.404	0.86	0.445	3.42	0.935	8.22	1.74	4.47	0.513	2.36	0.268
T06-30(2) - 40	50	45.17	0.0343	0.0284	0.568	0.85	0.42	3.49	0.92	8.17	1.714	4.25	0.504	2.32	0.199
T06-30(2) - 41	58	43.53	0.053	0.0248	0.476	0.89	0.49	3.26	0.913	8.15	1.658	3.99	0.457	2.24	0.215
T06-30(2) - 42	57	43.23	0.037	0.0317	0.447	0.92	0.437	3.39	0.916	7.88	1.662	4.32	0.478	2.21	0.235
T06-30(2) - 43	59	41.31	0.05	0.0274	0.485	0.86	0.481	3.47	0.913	7.57	1.659	3.98	0.474	2.29	0.244
T06-30(2) - 44	44	39.63	0.0203	0.0309	0.472	0.82	0.5	3.34	0.887	7.43	1.589	3.91	0.429	2.08	0.205
T06-30(2) - 45	56	37.81	0.043	0.0281	0.58	0.85	0.488	3.5	0.87	7.45	1.517	3.39	0.395	2	0.204
T06-30(2) - 46	56	37.22	0.046	0.0346	0.479	0.97	0.479	3.4	0.912	7.25	1.471	3.41	0.367	1.84	0.162
T06-30(2) - 47	68	35.78	0.037	0.023	0.56	1.05	0.505	3.62	0.901	7.04	1.418	3.44	0.347	1.62	0.152
T06-30(2) - 48	58	35.3	0.04	0.0244	0.47	0.93	0.462	3.48	0.906	7.19	1.448	3.33	0.361	1.68	0.173
T06-30(2) - 49	66	33.83	0.0465	0.0314	0.415	1.05	0.545	3.77	0.925	6.88	1.324	3.08	0.32	1.46	0.147
T06-30(2) - 50	56	31.84	0.039	0.0292	0.514	0.95	0.53	3.59	0.917	6.85	1.194	2.77	0.272	1.37	0.125
T06-30(2) - 51	54.9	30.29	0.0442	0.0303	0.522	0.99	0.476	3.39	0.846	6.59	1.154	2.67	0.295	1.33	0.126
SESSION (B)															
Standard	**P**	**Y**	**Ce**	**Pr**	**Nd**	**Sm**	**Eu**	**Gd**	**Tb**	**Dy**	**Ho**	**Er**	**Tm**	**Yb**	**Lu**
GSD-1G-19 - 1	486	31.5	38.47	40.8	40.4	44	37	36.8	41	37.2	44.4	26.1	45.1	486	31.5
GSD-1G-19 - 2	546	31.5	42.4	44.31	45.9	46.4	39.7	42.3	45.8	39.8	48.5	30.9	49.2	546	31.5
GSD-1G-29 - 1	555	33.93	39.44	41.88	41.1	45.1	38.31	43.4	42.58	45.4	45.64	33.18	47.35	555	33.93
GSD-1G-29 - 2	545	31.18	39.39	42.47	42.8	45.9	37.86	43	43.15	45.7	45.96	34.11	47.49	545	31.18
GSD-1G-51 - 1	526	37.31	39.05	41.58	41.12	43.84	37.39	43.72	42.23	48.11	45.69	35.52	47.14	526	37.31
GSD-1G-51 - 2	508	38.09	38.72	41.18	41	44.07	36.97	43.38	41.7	47.46	44.47	34.83	46.51	508	38.09
GSD-1G-19 - 3	562	33.5	40.6	43.7	42.6	47.1	37.6	43.2	43.8	42.8	46.7	32.2	49	562	33.5
GSD-1G-19 - 4	590	33.1	43.3	44.9	44.5	48.4	39.2	46.1	45.3	43.4	48	33.4	50.3	590	33.1
GSD-1G-29 - 3	517	35.6	39.7	42.8	42.3	45.9	38.18	44.7	43.25	45.9	46.62	34.04	48.6	517	35.6
GSD-1G-29 - 4	543	32.6	41.1	43.89	43	46.5	39.26	45.8	44.9	48.5	47.6	36.22	50.26	543	32.6
GSD-1G-51 - 3	493	36.1	39.1	42.06	41.37	44.9	36.98	44.1	42.38	47.5	44.77	35.35	47.09	493	36.1
GSD-1G-51 - 4	493	36.15	39.62	41.72	41.36	44.5	37.02	43	42.11	46.58	44.64	35.25	46.76	493	36.15
GSD-1G-19 - 5	491	30.7	38.3	40.51	40.8	42.8	36.7	41.5	40.73	42.3	43.6	32.3	45.3	491	30.7
GSD-1G-19 - 6	586	30.9	42.6	45	43.5	49	39.9	44.6	44.9	43.4	48.4	33.9	50.5	586	30.9
GSD-1G-29 - 5	518	34.2	39.71	42.46	41.9	45.1	37.83	44.4	42.75	45.7	45.92	33.49	47.66	518	34.2
GSD-1G-29 - 6	541	31.9	41.82	44.6	44.5	48.5	39.1	46.3	44.6	45.3	48.84	35	50.6	541	31.9

GSD-1G-51 - 5	497	37.6	41.97	44.51	44.16	46.99	39.36	46.23	44.39	48.73	47.91	35.51	49.08	497	37.6
GSD-1G-51 - 6	520	37.8	42.72	45.22	45.4	48.7	40.51	47.3	45.58	49.4	48.9	36.54	50.2	520	37.8
NIST-612 - 1	50	38.03	38.71	37.15	36.22	38.22	35.01	36.96	36.03	36.01	37.96	37.9	38.01	50	38.03
NIST-612 - 2	52.8	37.95	38.71	37.27	35.69	37.97	35.17	36.51	35.99	35.99	38.12	38.02	37.99	52.8	37.95
NIST-612 - 3	51.2	38.06	38.67	37.18	35.82	38.09	34.7	36.66	36	35.94	37.91	37.95	37.91	51.2	38.06
NIST-612 - 4	50.8	37.93	38.68	37.21	35.78	38.02	35.07	36.75	35.95	36.06	38.01	38.24	38.07	50.8	37.93
NIST-612 - 5	50.7	38.13	38.61	37.12	35.95	38.03	34.96	36.65	35.97	36.06	37.96	37.88	37.97	50.7	38.13
NIST-612 - 6	51.3	37.87	38.83	37.28	35.99	38.22	35.23	36.76	36.07	35.95	38.05	38.06	38.02	51.3	37.87
Unknown															
T06-30 - 1	79	69	0.04	-	-	0.42	0.324	2.59	0.82	8.97	2.47	8.68	1.13	8.1	1.007
T06-30 - 2	69	69.2	-	-	-	-	0.224	2.18	0.787	9.28	2.06	7.47	0.96	6.89	0.591
T06-30 - 3	68	56.2	-	-	0.2	0.54	0.322	2.17	0.673	7.4	1.73	6.08	0.81	5.59	0.606
T06-30 - 4	56	79.2	0.033	0.0184	0.304	0.61	0.373	3.06	1.047	10.32	2.89	9.21	1.395	8.66	1.127
T06-30 - 5	73	70.2	0.03	0.0179	0.332	0.66	0.369	2.97	0.862	8.91	2.59	8.46	1.247	7.77	1.046
T06-30 - 6	61	67.1	0.027	0.0173	0.48	0.6	0.364	2.87	0.918	9.12	2.57	7.83	1.125	6.52	0.876
T06-30 - 7	77	70.6	0.026	0.026	0.313	0.73	0.424	3.15	0.928	9.53	2.61	8.47	1.2	7.7	1.144
T06-30 - 8	81	72.2	0.021	0.0219	0.37	0.82	0.421	2.98	0.928	9.47	2.7	8.52	1.366	7.57	1.085
T06-30 - 9	69	70.9	0.028	0.0137	0.362	0.65	0.399	2.98	0.96	9.56	2.71	8.42	1.285	7.27	0.971
T06-30 - 10	71	71.8	-	0.0142	0.351	0.65	0.392	3	0.992	9.59	2.72	8.46	1.348	7.44	0.988
T06-30 - 11	63	71.8	-	0.0159	0.369	0.78	0.407	2.83	0.988	9.78	2.76	8.34	1.32	7.29	0.981
T06-30 - 12	63	69.8	0.024	0.0174	0.327	0.64	0.382	3.01	0.963	9.43	2.63	7.86	1.228	7.22	0.912
T06-30 - 13	68	68.3	0.024	0.026	0.41	0.74	0.402	2.83	0.929	9.04	2.58	7.76	1.18	6.39	0.987
T06-30 - 14	63	72.6	0.022	0.0169	0.338	0.63	0.367	2.93	0.934	8.87	2.54	7.7	1.255	6.66	0.98
T06-30 - 15	59	72	0.028	0.024	0.405	0.88	0.345	2.75	0.894	8.21	2.42	7.15	1.21	6.66	1.034
T06-30 - 16	68	67.8	0.045	0.021	0.47	0.82	0.4	2.94	0.988	8.96	2.66	7.73	1.293	7.58	1.076
T06-30 - 17	56	63	0.03	-	0.37	0.84	0.352	2.71	0.881	8.54	2.44	7.48	1.208	6.77	0.99
T06-30 - 18	59	62	0.047	0.036	0.354	0.8	0.358	2.54	0.793	8.29	2.36	7.38	1.098	6.97	0.936
T06-30 - 19	61	61	0.022	0.0204	0.331	0.66	0.365	2.85	0.844	8.17	2.28	7.22	1.144	6.49	0.88
T06-30 - 20	74	58.2	0.028	0.0163	0.323	0.73	0.365	2.45	0.897	8.07	2.26	6.77	0.976	5.25	0.657
T06-30 - 21	63	54.1	0.022	0.019	0.4	0.87	0.421	2.73	0.77	7.76	1.84	5.95	0.86	4.61	0.549
T06-30 - 22	66	50.9	0.029	0.0153	0.47	0.71	0.372	2.33	0.763	7.42	1.82	5.4	0.789	4.01	0.459
T06-30 - 23	61	47.3	0.019	0.0169	0.319	0.74	0.393	2.72	0.808	7.51	1.728	5.13	0.666	3.52	0.406

T06-30 - 24	76	47.4	0.026	0.018	0.462	0.84	0.345	2.91	0.768	7.53	1.79	5.09	0.67	3.54	0.401
T06-30 - 25	61	44.2	0.023	0.0215	0.354	0.68	0.437	2.96	0.796	7.1	1.723	4.59	0.591	3.08	0.339
T06-30 - 26	60	42.6	0.018	0.024	0.377	0.79	0.365	2.97	0.738	7.4	1.66	4.37	0.573	2.67	0.251
T06-30 - 27	50	37	0.0158	0.0174	0.317	0.7	0.402	2.92	0.702	6.89	1.465	3.93	0.47	2.21	0.228
T06-30 - 28	54	30.4	-	0.0147	0.29	0.67	0.379	2.44	0.68	5.77	1.14	3.43	0.35	1.71	0.178

Garnet rare-earth element concentrations in ppm for internal standards GSD-1G and NIST-612, and unknowns T01-40, T06-20 and T06-30. Data was collected over two sessions using a RESOlution LR 193 nm Excimer laser system coupled with an Agilent 7900x ICP–MS at Adelaide Microscopy. Where cells contain no value, the given elemental analysis was below the limit of detection (LOD).

APPENDIX 2f: Extended LA–ICP–MS U–Pb Rutile Geochronology Results

Standard	Pb207/U235	2σ	Pb206/U328	2σ	Error Corr.	Pb207/Pb206	2σ	Pb207/U235 Age	2σ	Pb206/U328 Age	2σ	Pb207/Pb206 Age	2σ	Th232 (CPS)
R10 - 1	1.913	0.045	0.184	0.0021	0.24492	0.0754	0.0017	1082	16	1088	11	1061	47	78
R10 - 2	1.956	0.035	0.1862	0.0019	0.13784	0.0764	0.0015	1098	12	1102	10	1088	40	0
R10 - 3	1.861	0.04	0.1819	0.0021	0.10193	0.0744	0.0018	1064	14	1077	11	1033	49	49.2
R10 - 4	1.988	0.038	0.1884	0.0019	0.14645	0.0763	0.0016	1109	13	1112	10	1096	42	0
R10 - 5	1.876	0.038	0.1798	0.0017	0.20047	0.0759	0.0016	1070	13	1065.4	9.3	1072	42	273.8
R10 - 6	1.955	0.035	0.1869	0.002	0.1159	0.0761	0.0014	1098	12	1104	11	1080	40	0
R10 - 7	1.911	0.038	0.1827	0.002	0.16131	0.076	0.0015	1082	13	1081	11	1083	40	33.6
R10 - 8	1.922	0.039	0.1843	0.0021	0.084369	0.0758	0.0016	1086	13	1090	11	1070	42	0
R10 - 9	1.912	0.036	0.1839	0.0019	0.16072	0.0756	0.0016	1084	13	1088	11	1066	43	182
R10 - 10	1.974	0.038	0.1894	0.0023	0.093814	0.0758	0.0017	1106	13	1118	12	1080	46	0
R19 - 1	0.582	0.069	0.0811	0.003	0.050001	0.0532	0.0064	442	44	502	18	100	220	626
R19 - 2	0.612	0.068	0.0814	0.0033	0.042852	0.0544	0.0061	455	45	504	19	220	220	0
R19 - 3	0.624	0.08	0.0821	0.0031	0.086137	0.0563	0.0074	453	50	508	18	150	240	609
R19 - 4	0.613	0.075	0.0824	0.0029	0.072585	0.0566	0.0072	450	49	510	17	160	240	0
R19 - 5	0.627	0.066	0.081	0.0029	0.054391	0.0588	0.0071	476	46	501	17	300	230	626
R19 - 6	0.697	0.071	0.0843	0.0034	0.22302	0.0618	0.0061	520	42	521	20	430	190	0
R19 - 7	0.617	0.065	0.0821	0.0031	0.064016	0.0576	0.0065	466	43	508	18	230	210	616
R19 - 8	0.612	0.071	0.0785	0.003	0.050194	0.0563	0.0069	452	47	486	18	210	240	0
R19 - 9	0.657	0.063	0.0826	0.0032	0.068276	0.0603	0.0063	499	41	511	19	360	200	2370
R19 - 10	0.646	0.07	0.0855	0.0033	0.020589	0.0569	0.0065	480	46	528	20	230	220	0
Unknown														
T06-20-grt2 - 1	2.004	0.061	0.1485	0.002	0.37919	0.0978	0.0027	1113	21	892	11	1568	51	1061
T06-20-grt2 - 2	2.965	0.084	0.2032	0.0039	0.53779	0.1073	0.0028	1394	22	1192	21	1739	47	0
T06-20-grt3 - 1	8.45	0.47	0.395	0.016	0.51552	0.1577	0.0073	2271	50	2141	71	2412	84	1070
T06-20-grt3 - 2	5.96	0.53	0.2848	0.0084	0.031699	0.153	0.013	1927	67	1613	42	2270	120	499
T06-20-grt3 - 3	4.719	0.091	0.2864	0.0032	0.14102	0.121	0.0025	1768	16	1623	16	1961	37	183
T06-20-grt3 - 4	4.3	0.16	0.2467	0.0062	0.39611	0.1283	0.0046	1683	31	1420	32	2043	65	427
T06-21-grt3 - 1	4.51	0.37	0.269	0.018	0.88003	0.1228	0.0051	1707	70	1527	90	1976	75	5760

T06-21-grt4 - 1	2.975	0.078	0.2002	0.0031	0.31549	0.1094	0.003	1400	21	1176	17	1771	50	602
T06-21-grt5 - 1	5.26	0.11	0.3246	0.0037	0.31622	0.118	0.0023	1860	18	1811	18	1917	36	27.8
T06-21-grt6 - 1	4.86	0.47	0.172	0.017	0.57133	0.226	0.022	1733	89	1012	94	2920	150	179
T06-21A-grt1 - 1	3.531	0.073	0.2299	0.0039	0.64441	0.1114	0.0018	1530	17	1333	21	1820	29	10.7
T06-21A-grt2 - 1	4.287	0.074	0.2793	0.003	0.27543	0.1116	0.0019	1688	14	1587	15	1816	30	0
T06-21A-grt2 - 2	4.14	0.17	0.2609	0.0067	0.36961	0.1169	0.0045	1655	34	1493	34	1882	70	147
T06-21A-grt2 - 3	1.148	0.083	0.0837	0.0031	0.070222	0.1006	0.0076	765	40	518	19	1510	160	107
T06-21A-grt3 - 1	5.17	0.15	0.3164	0.0049	0.03062	0.1197	0.0036	1844	24	1772	24	1947	56	223
T06-21A-grt3 - 2	3.93	0.12	0.2277	0.0051	0.36303	0.1277	0.0041	1618	26	1320	27	2039	55	1270
T06-21A-grt3 - 3	3.23	0.15	0.174	0.0048	0.30428	0.137	0.0063	1450	37	1033	27	2140	85	0
T06-21A-grt5 - 1	5.424	0.077	0.333	0.0028	0.2569	0.1181	0.0017	1887	12	1855	13	1922	26	0
T06-21A-grt5 - 2	5.61	0.15	0.3482	0.0072	0.27254	0.1187	0.0035	1913	24	1925	34	1921	54	271
T06-21A-grt5 - 3	5.62	0.13	0.3366	0.0042	0.14641	0.1225	0.0029	1915	19	1870	20	1982	41	110
T06-21A-grt6 - 1	4.29	0.1	0.2775	0.0039	0.021931	0.1139	0.0029	1688	20	1578	20	1849	47	235
T06-21A-grt6 - 2	4.395	0.077	0.281	0.0034	0.34463	0.1134	0.0019	1708	14	1595	17	1847	31	163
T06-21A-grt6 - 3	2.358	0.066	0.1788	0.0028	0.30889	0.0967	0.0026	1226	20	1060	15	1542	52	322
T06-21A-grt7 - 1	3.01	0.079	0.2139	0.0035	0.2045	0.1028	0.0026	1407	20	1249	19	1661	47	346
T06-21A-grt8 - 1	4.09	0.12	0.2632	0.0061	0.75594	0.1149	0.0024	1655	25	1505	31	1872	38	650
T06-27 - 1	1.136	0.055	0.106	0.0021	0.081046	0.0788	0.004	762	26	649	12	1080	110	2470
T06-27 - 2	1.72	0.045	0.1335	0.0017	0.075224	0.0942	0.0028	1012	16	807.5	9.7	1481	56	1730
T06-27 - 3	5.799	0.088	0.3524	0.0043	0.58589	0.1208	0.0014	1945	13	1946	21	1965	21	0
T06-27 - 4	3.39	0.13	0.2335	0.0065	0.82922	0.1065	0.0023	1496	31	1351	34	1731	40	0
T06-27 - 5	3.12	0.14	0.2139	0.0068	0.82309	0.1067	0.003	1428	35	1248	36	1731	52	10360
T06-27 - 6	2.34	0.15	0.185	0.012	0.72509	0.094	0.0045	1208	49	1089	67	1468	90	1365
T06-27 - 7	3.639	0.049	0.2405	0.002	0.41598	0.1097	0.0013	1556	11	1389	10	1788	22	0
T06-27 - 8	4.73	0.13	0.3007	0.0062	0.87819	0.1137	0.0016	1764	25	1692	31	1851	25	49000
T06-27 - 9	3.37	0.3	0.1112	0.0058	0.21325	0.231	0.023	1426	68	677	34	2870	170	838
T06-27 - 10	2.54	0.15	0.1875	0.0074	0.89012	0.0988	0.0028	1272	41	1106	40	1585	54	1960
T06-27 - 11	2.602	0.072	0.1883	0.0024	0.24261	0.1014	0.0029	1301	19	1112	13	1630	53	0
T06-27 - 12	5.871	0.078	0.35	0.0037	0.52636	0.1226	0.0013	1956	12	1934	18	1992	19	46300
T06-27 - 13	3.117	0.06	0.214	0.002	0.41494	0.1068	0.002	1435	15	1250	11	1739	34	8800
T06-27 - 14	1.752	0.075	0.1363	0.0032	0.53184	0.0942	0.0034	1024	28	824	18	1496	68	12160

T06-27 - 15	1.86	0.05	0.1402	0.0029	0.2516	0.0972	0.0027	1065	18	846	16	1559	53	30400
T06-27 - 16	3.75	0.23	0.241	0.013	0.94365	0.1135	0.0024	1561	50	1388	69	1846	40	25100
T06-27 - 17	2.24	0.16	0.1725	0.0098	0.93915	0.0922	0.0023	1163	49	1020	54	1459	49	76000
T06-27 - 18	4.049	0.052	0.2592	0.0021	0.35382	0.1125	0.0014	1643	10	1486	11	1839	24	0
T06-27 - 19	1.084	0.027	0.1076	0.0014	0.51904	0.0734	0.0016	745	13	658.4	8.3	1004	45	3640
T06-27 - 20	1.22	0.16	0.118	0.01	0.98681	0.0745	0.0034	801	68	724	60	990	89	317
T06-27 - 21	1.627	0.068	0.1412	0.0039	0.94642	0.0844	0.0019	974	24	851	22	1301	44	964
T06-27 - 22	1.584	0.029	0.1356	0.0014	0.27389	0.085	0.0016	962	11	819.5	8	1301	35	0
T06-27 - 23	1.592	0.032	0.1346	0.0017	0.12999	0.0851	0.002	965	12	813.9	9.8	1305	45	4190
T06-27 - 24	3.556	0.089	0.241	0.0048	0.87979	0.1065	0.0013	1534	20	1391	25	1737	22	2520
T06-27 - 25	4.32	0.14	0.2781	0.0067	0.78541	0.1125	0.0019	1688	26	1580	34	1832	30	633
T06-27 - 26	1.904	0.083	0.1513	0.0042	0.85999	0.0902	0.0021	1069	30	907	24	1406	47	770
T06-27 - 27	1.911	0.044	0.1525	0.0023	0.43562	0.0917	0.0019	1082	16	915	13	1448	40	6940
T06-27 - 28	1.093	0.038	0.1073	0.0021	0.48457	0.075	0.0025	753	20	657	12	1051	68	0
T06-27 - 29	1.162	0.054	0.1094	0.0028	0.90549	0.0784	0.0026	779	25	668	16	1113	65	5460
T06-27 - 30	5.55	0.17	0.3357	0.008	0.95702	0.1187	0.0013	1903	26	1863	38	1935	19	0
T06-27 - 31	0.759	0.032	0.0807	0.0012	0.24022	0.0686	0.0029	569	19	499.9	7.2	827	92	4600
T06-27 - 32	1.148	0.043	0.1053	0.0023	0.2402	0.0796	0.0029	771	20	645	13	1157	70	0
T06-27 - 33	4.51	0.11	0.2818	0.0054	0.80943	0.115	0.0014	1729	21	1599	27	1878	23	10300
T06-27 - 34	2.77	0.2	0.196	0.01	0.96633	0.1012	0.0031	1316	62	1147	57	1624	62	2690
T06-27 - 35	2.071	0.057	0.1623	0.003	0.53316	0.0934	0.0022	1136	19	969	17	1481	45	300
T06-27 - 36	2.216	0.091	0.169	0.0041	0.89445	0.0965	0.003	1183	28	1007	22	1548	56	501

U and Pb isotopic ratios and age values from rutile in metapelitic samples T06-20, T06-21, T06-21A and T06-27. Analyses highlighted in grey were not used to constrain an upper intercept age (applicable to a U–Pb rutile Tera-Wasserburg concordia).

APPENDIX 2g: Extended Mineral Equilibria Forward Modelling Results

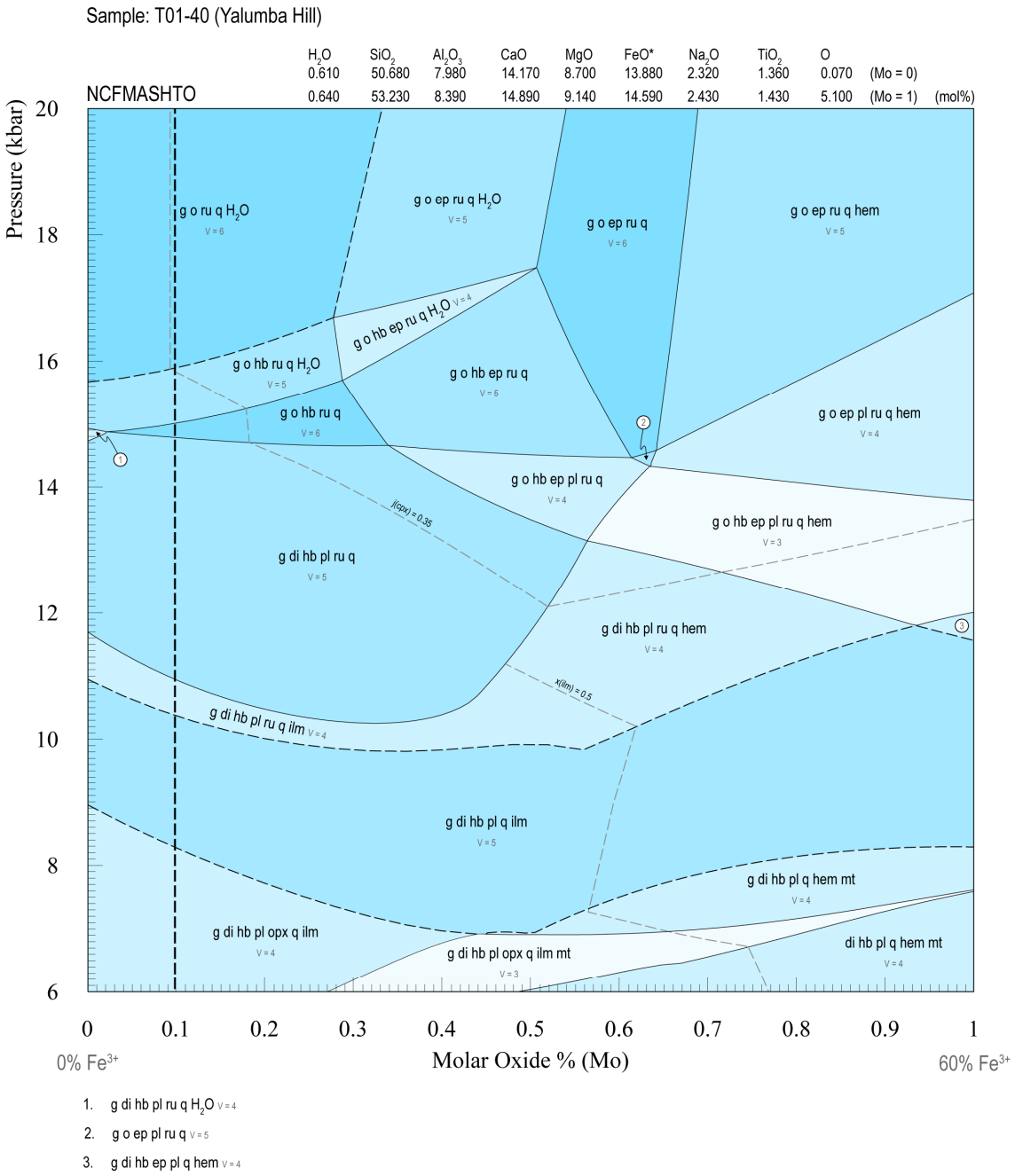

Pressure–composition (*P–X*) pseudosection for retrogressed eclogite sample T01-40. Given on the horizontal axis is 0–60% Fe^{3+}. The peak field, g o ru q H_2O (bordered by the dashed black line), is located at ca. 15.7–20 kbar (up-pressure unconstrained) and ca. 0–0.3 molar oxide proportion. The vertical dashed black line that passes through the inferred peak field at 0.1 molar oxide marks the oxidation state selected for subsequent *P–T* calculations.

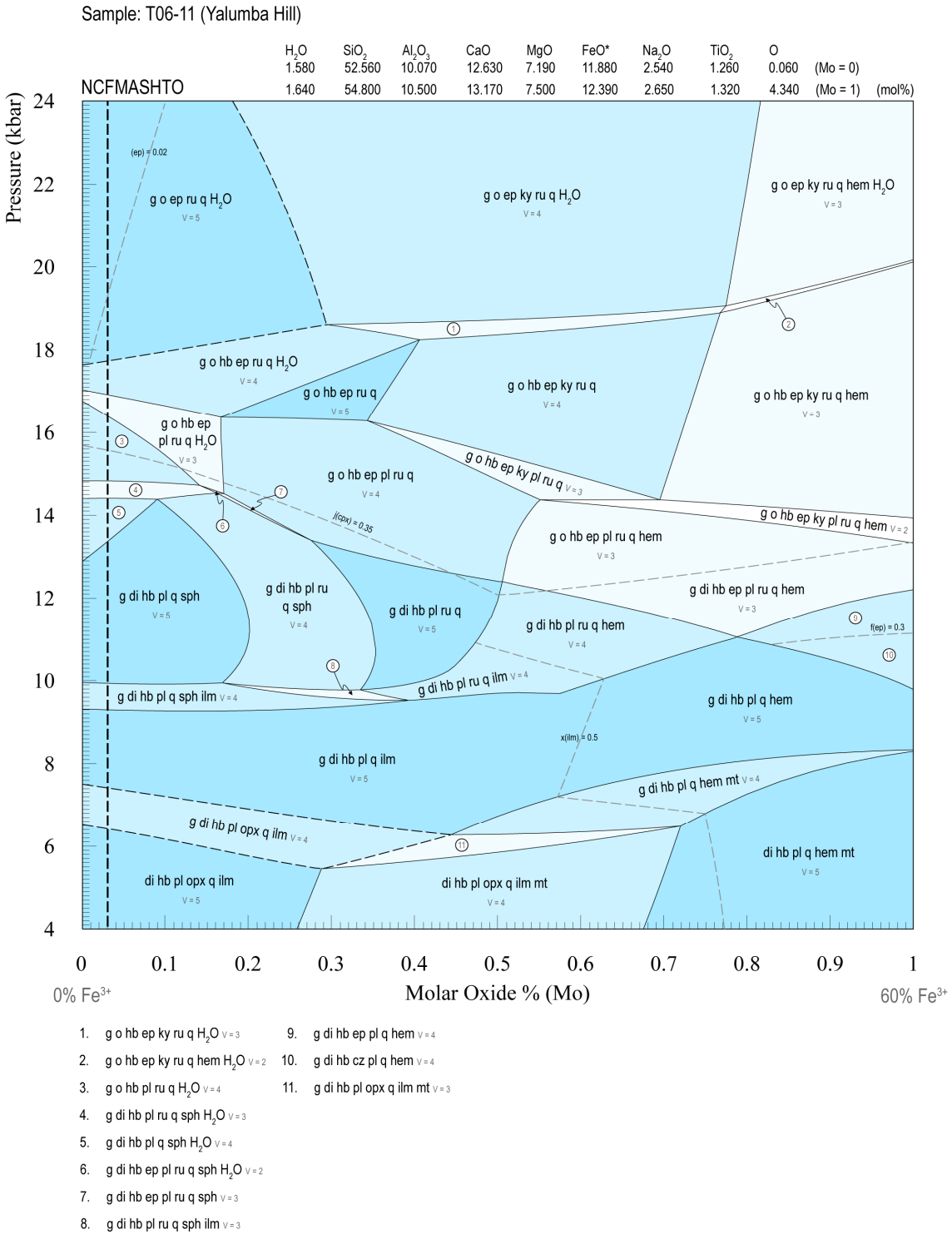

1. g o hb ep ky ru q H_2O V = 3
2. g o hb ep ky ru q hem H_2O V = 2
3. g o hb pl ru q H_2O V = 4
4. g di hb pl ru q sph H_2O V = 3
5. g di hb pl q sph H_2O V = 4
6. g di hb ep pl ru q sph H_2O V = 2
7. g di hb ep pl ru q sph V = 3
8. g di hb pl ru q sph ilm V = 3
9. g di hb ep pl q hem V = 4
10. g di hb cz pl q hem V = 4
11. g di hb pl opx q ilm mt V = 3

Pressure–composition (*P–X*) pseudosection for retrogressed eclogite sample T06-11. Given on the horizontal axis is 0–60% Fe^{3+}. The peak field, g o ep ru q H_2O (bordered by the dashed black line), is located at ca. 17.7–24 kbar (up-pressure unconstrained) and ca. 0–0.3 molar oxide proportion. The vertical dashed black line that passes through the inferred peak field at 0.03 molar oxide marks the oxidation state selected for subsequent *P–T* calculations.

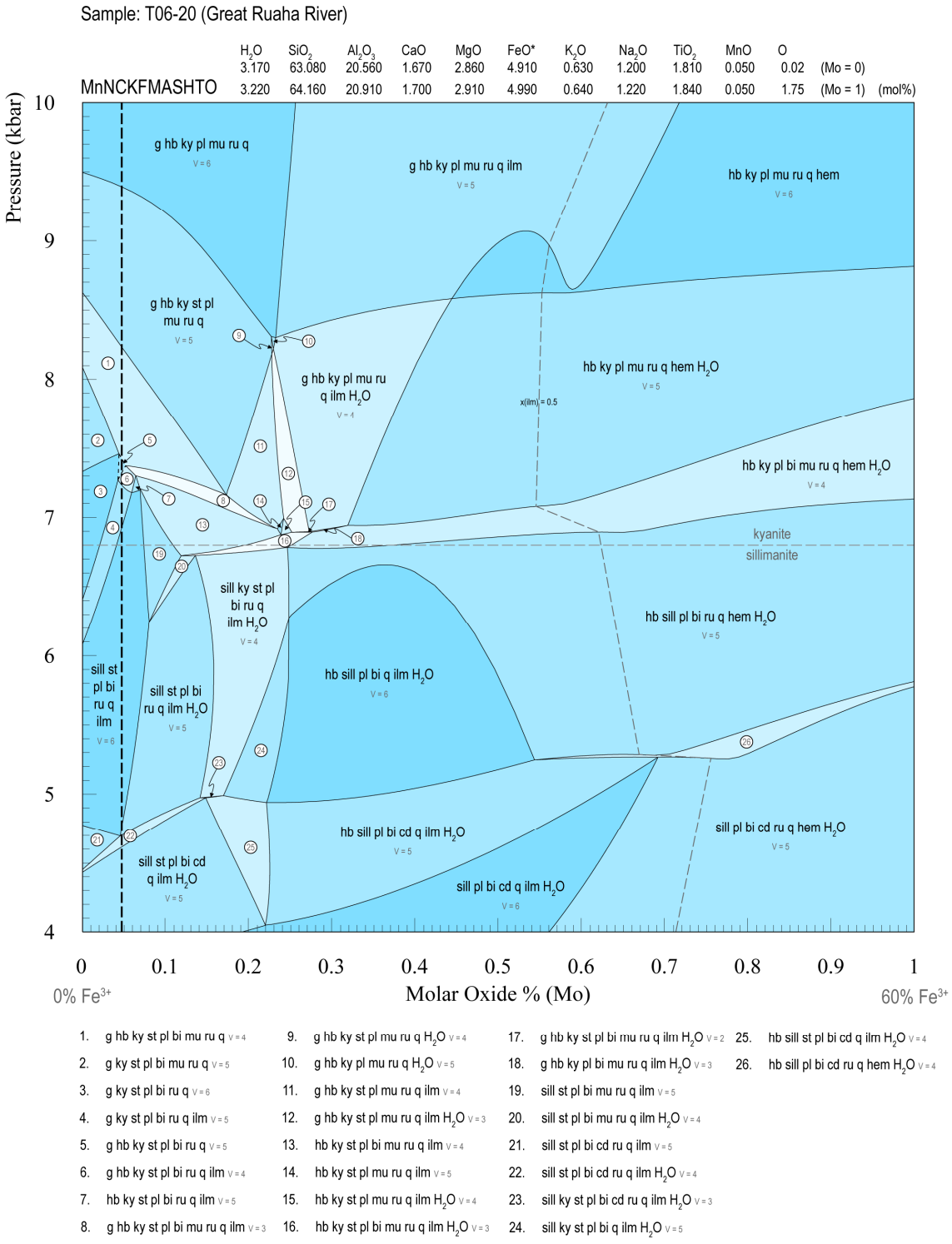

Pressure–composition (*P–X*) pseudosection for T06-20 metapelite. Given on the horizontal axis is 0–60% Fe^{3+}. The peak field, g hb ky st pl bi ru q (bordered by the dashed black line), is located at ca. 7.25–7.45 kbar and ca. 0.04–0.05 molar oxide proportion. The vertical dashed black line that passes through the inferred peak field at 0.045 molar oxide marks the oxidation state selected for subsequent *P–T* calculations.

APPENDIX 2h: LA–ICP–MS Zr-in-Rutile Thermometry Results

T01-40

The occurrence of both zircon and quartz in sample T01-40 (Reddy *et al*., 2003; Collins *et al*., 2004) ensures its suitability with respect to the application of Zr-in-rutile thermometry (Watson *et al*., 2006). Sample T01-40 yielded a range of Zr-in-rutile concentrations from 258 ppm to 1180 ppm, correlating with temperatures of 672–814 °C at 18 kbar (section 4.6) using the pressure-dependent thermometer calibration of Tomkins *et al*. (2007). Of 36 total analyses, 25 were derived from mounted rutile grains and the remainder were obtained from in-situ rutile grains within garnet (Fig. a). The rutile grains showed no evidence of Zr exsolution (Fig. c). The analyses reported here comprise 31 of the original 36 – 3 analyses returned no values for Zr (ppm) and 2 contained significant Si. All temperature estimates are plotted at a pressure of 18 kbar (Fig. d, e) – a pressure selected in light of pressure estimate results derived from mineral equilibria forward modelling (section 4.6). The complete array of Zr-in-rutile results are detailed below.

T06-20

A total of 37 rutile grains hosted within garnet were analysed in zircon- and quartz-bearing sample T06-20; the majority of these grains were influenced significantly by Si contamination. Omitted grains included 7 that recorded Si concentrations above 10000 ppm, 1 which returned no Zr (ppm) value, and 11 that were inferred to represent prograde temperatures, as shown in Figure f. Consequently, 18 grains were retained for further application in this study. Resultant temperature estimates ranged from 671–745 °C at 9 kbar (this pressure selected given its relevance to mineral equilibria forward modelling), corresponding to Zr concentration of 411–926 ppm (Fig. f).

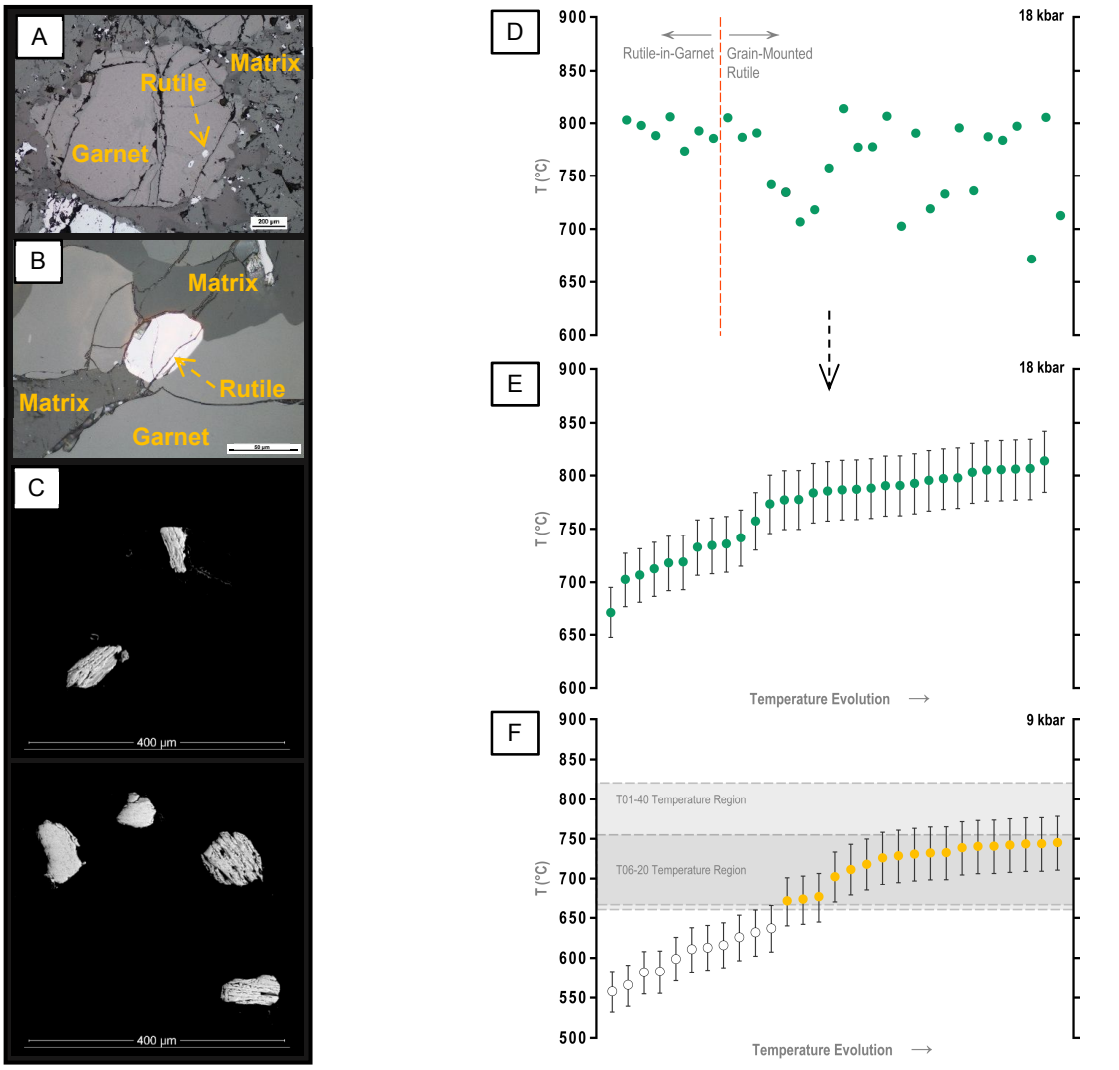

Fig: (A) Reflected light image of in-situ rutile grains within garnet in sample T01-40. (B) Reflected light image of an in-situ rutile grain in sample T01-40, included to demonstrate that in some cases, rutile has been exposed to matrix processes. (C) Backscattered electron images of grain-mounted rutile grains in sample T01-40 where rutile grains show no evidence of Zr exsolution. (D) Each Zr-in-rutile analysis as a function of temperature for sample T01-40. Temperatures were calculated at a pressure of 18 kbar. (E) Zr-in-rutile analyses ordered as a function of ascending temperature for sample T01-40. (F) Zr-in-rutile analyses as a function of ascending temperature for sample T06-20. White circles represent analyses that are inferred to represent prograde temperatures, and as a result, a grey rectangle comprises the retained analyses for use in conjunction with mineral equilibria forward modelling (yellow circles) Temperatures were calculated for a pressure of 9 kbar. An additional grey rectangle is used to show the temperature region defined by the analyses applicable to sample T01-40 (i.e. in E). In both (E) and (F), 2σ error bars are given for each data point (see Appendix 1d for error propagation methodology).

Standard	Zr (ppm)	Zr (2σ)
NIST610 - 1	447.1	4
NIST610 - 2	448.8	3.9
NIST610 - 3	448.6	3.4
NIST610 - 4	447.4	4.3
NIST610 - 5	447.1	4.2
NIST610 - 6	448.3	4.2
NIST610 - 7	450	3.8
NIST610 - 8	446.5	3.7
NIST610 - 9	448.9	4.2
NIST610 - 10	446.8	4.2
NIST610 - 11	449.4	4.4
NIST610 - 12	447	3.9
NIST610 - 13	447.8	4.3
NIST610 - 14	448.1	4.3
GSD51 - 1	39.8	0.27
GSD51 - 2	39.94	0.26
GSD13 - 1	39.2	1
GSD19 - 1	39.26	0.68
GSD29 - 1	39.88	0.46
GSD51 - 3	39.82	0.28
GSD51 - 4	39.53	0.27
GSD13 - 2	39.8	1.1
GSD19 - 2	39.09	0.74
GSD29 - 2	39.88	0.49
GSD51 - 5	39.72	0.29
GSD51 - 6	39.6	0.31
GSD13 - 3	40.1	1.1
GSD19 - 3	39.89	0.59
GSD29 - 3	39.93	0.42

GSD51 - 7	39.76	0.28
GSD51 - 8	39.3	0.3
GSD13 - 4	40	1
GSD19 - 4	39.21	0.89
GSD29 - 4	40.02	0.52
GSD51 - 9	39.89	0.27
GSD51 - 10	39.8	0.29
GSD13 - 5	39.2	1.1
GSD19 - 5	39.81	0.92
GSD29 - 5	39.05	0.68
GSD51 - 11	39.83	0.26
GSD51 - 12	40.06	0.3
GSD13 - 6	39.3	1.2
GSD19 - 6	39.79	0.83
GSD29 - 6	38.95	0.69
GSD51 - 13	39.84	0.31
GSD51 - 14	40.27	0.27
GSD13 - 7	40.6	1.3
GSD19 - 7	40.42	0.75
GSD29 - 7	40.26	0.52

Unknown	**Zr (ppm)**	**Zr (2σ)**	**Temp. (°C) – 18 kbar**	**Temp. (2σ)**	**Rel. Error Quadrature Sum**
T01-40-Ru-Mount - 2	418	6.6	712.54	25.72	0.034875864
T01-40-Ru-Mount - 3	1092	14	805.52	29.04	0.03484103
T01-40-Ru-Mount - 4	258	3.5	671.72	24.26	0.034894646
T01-40-Ru-Mount - 5	1009	21	797.21	28.75	0.034843772
T01-40-Ru-Mount - 6	887	15	783.93	28.27	0.03484829
T01-40-Ru-Mount - 7	916	11	787.22	28.39	0.034847157
T01-40-Ru-Mount - 8	541	27	735.91	26.55	0.034866174
T01-40-Ru-Mount - 9	993	25	795.55	28.69	0.03484433
T01-40-Ru-Mount - 10	524	9.5	732.90	26.45	0.034867381
T01-40-Ru-Mount - 11	449	5.5	718.98	25.95	0.034873125
T01-40-Ru-Mount - 12	946	12	790.53	28.51	0.034846025

T01-40-Ru-Mount - 14	373	5.1	702.62	25.36	0.034880204
T01-40-Ru-Mount - 15	1102.3	8.7	806.52	29.08	0.034840705
T01-40-Ru-Mount - 16	832.8	7	777.56	28.04	0.034850522
T01-40-Ru-Mount - 17	831	11	777.34	28.03	0.034850599
T01-40-Ru-Mount - 18	1180	16	813.80	29.34	0.034838361
T01-40-Ru-Mount - 19	680	14	757.57	27.33	0.034857792
T01-40-Ru-Mount - 20	445	5.3	718.12	25.92	0.034873489
T01-40-Ru-Mount - 21	391.4	2.5	706.76	25.51	0.034878375
T01-40-Ru-Mount - 22	533	18	734.53	26.50	0.034866727
T01-40-Ru-Mount - 23	576	16	741.75	26.76	0.034863857
T01-40-Ru-Mount - 25	948.4	5.1	790.79	28.52	0.034845937
T01-40-Ru-Mount - 26	911.8	5.2	786.75	28.37	0.034847319
T01-40-Ru-TS - 1	1089	31	805.23	29.03	0.034841125
T01-40-Ru-TS - 2	902	19	785.64	28.33	0.034847699
T01-40-Ru-TS - 3	966.1	7.8	792.70	28.58	0.034845289
T01-40-Ru-TS - 4	799.7	8.2	773.49	27.90	0.034851965
T01-40-Ru-TS - 8	1098	13	806.10	29.06	0.03484084
T01-40-Ru-TS - 9	925.5	8.7	788.27	28.43	0.034846794
T01-40-Ru-TS - 10	1016.5	9.1	797.98	28.77	0.034843515
T01-40-Ru-TS - 11	1066	11	802.97	28.95	0.034841863
Unknown	**Zr (ppm)**	**Zr (2σ)**	**Temp. (°C) – 9 kbar**	**Temp. (2σ)**	**Rel. Error Quadrature Sum**
T06-20-Ru - 1	926	21	745.42	34.58	0.044411791
T06-20-Ru - 3	437	8	676.40	31.39	0.044437321
T06-20-Ru - 4	881	12	740.54	34.35	0.04441342
T06-20-Ru - 7	884	13	740.88	34.37	0.044413308
T06-20-Ru - 8	866	13	738.87	34.27	0.044413983
T06-20-Ru - 9	810	14	732.42	33.98	0.044416186
T06-20-Ru - 10	912	15	743.93	34.51	0.044412288
T06-20-Ru - 12	587	17	702.44	32.59	0.044427019
T06-20-Ru - 13	910	8	743.67	34.49	0.044412375
T06-20-Ru - 18	779	15	728.69	33.80	0.044417479
T06-20-Ru - 19	759	14	726.21	33.69	0.044418344

T06-20-Ru - 28	798	13	730.99	33.91	0.04441668
T06-20-Ru - 29	696	61	718.07	33.31	0.044421243
T06-20-Ru - 30	813	40	732.77	33.99	0.044416064
T06-20-Ru - 31	898	18	742.41	34.44	0.044412794
T06-20-Ru - 32	649	17	711.59	33.02	0.044423601
T06-20-Ru - 34	411	11	671.27	31.16	0.044439454
T06-20-Ru - 36	421	22	673.31	31.25	0.044438601

Zr-in-rutile temperature estimates with associated 2σ errors – calculated from the quadrature sum of relative errors (also given) – for internal standards NIST-610 and GSD-1G, and unknowns T01-40 and T06-20. Provided additionally are Zr concentrations and their accompanying 2σ error.

APPENDIX 2i: Garnet-Orthopyroxene Thermometry Results

Garnet-Orthopyroxene thermometry after Harley (1984) was applied to the garnet- and orthopyroxene-bearing sample, T06-09 (Fig. 6e) using the *a–x* relationships and thermodynamic data of Holland & Powell (1998). Average garnet rim compositions and average matrix orthopyroxene compositions (Appendix 2c) were used to derive temperature estimates. These span from 710 °C at 6 kbar to 757 °C at 10 kbar – this pressure range chosen given its relevance to the mineral equilibria model for sample T06-09 (section 4.6).

Pressure (kbar)	**6.0**	**7.0**	**8.0**	**9.0**	**10.0**
Temperature (°C)	710	721	733	745	757
Mineral end-member	**en**	**fs**	**py**	**alm**	
Activity	0.33	0.17	0.025	0.13	

Sample T06-09: Temperatures derived from garnet-orthopyroxene thermometry at set pressures. Also presented are both garnet and orthopyroxene mineral end-member activities. Abbreviations: en(enstatite), fs(ferrosilite), py(pyrope), alm(almandine). Abbreviations defined in THERMOCALC v.321. Activities are derived from Holland & Powell (1998).

APPENDIX 2j: Whole-Rock Chemistry Analyses

Wt% Oxide	T01-40	T06-11	T06-09	T06-20	T06-30
SiO2	47.5	48.6	50.4	55.1	47.57
TiO2	1.7	1.555	1.36	2.06	0.57
Al2O3	12.7	15.8	13.7	30.5	19.41
Fe2O3(Tot.)	17.3	14.6	14.45	5.63	10.56
MnO	0.28	0.31	0.24	0.053	0.18
MgO	5.47	4.46	6.56	1.78	6.38
CaO	12.4	10.9	10.45	1.48	12.37
Na2O	2.24	2.42	2.63	1.065	2.34
K2O	0.05	0.17	<0.001	0.848	0.2
P2O5	0.23	0.16	0.11	0.198	0.04
Total	99.87	98.975	99.9	98.714	99.62
LOI	0.18	0.47	0.10	1.24	1.24
FeO	-	-	-	-	7.17
Fe2O3	-	-	-	-	2.59

Whole-rock geochemical analyses for samples T01-40, T06-11, T06-09, T06-20 and T06-20. For all samples excluding T06-30, the LOI was calculated manually (see text).

APPENDIX 2k: Clinopyroxene Compositional Reintegration Results

Wt% Oxide	Composition 1	Composition 2	Composition 3	Composition 4	Composition 5	Composition 6	Composition 7	Composition 8	Composition 9	Composition 10
SiO2	51.14	50.93	51.90	50.08	49.84	52.23	52.26	51.70	46.94	48.94
TiO2	0.15	0.11	0.08	0.19	0.26	0.11	0.13	0.24	0.64	0.42
Al2O3	2.49	2.24	1.86	2.33	2.77	1.68	1.77	2.15	5.87	3.55
Cr2O3	0.00	0.02	0.03	0.01	0.00	0.02	0.02	0.02	0.01	0.02
FeO	9.01	9.63	8.74	9.46	9.25	8.84	9.52	7.92	12.38	8.27
MnO	0.10	0.06	0.07	0.13	0.11	0.10	0.13	0.08	0.10	0.05
MgO	13.01	13.19	13.55	12.73	12.80	13.43	13.02	13.65	11.80	13.01
ZnO	0.00	0.02	0.00	0.02	0.03	0.00	0.03	0.01	0.07	0.01
CaO	22.47	20.76	22.42	22.10	21.85	22.74	22.55	22.37	17.83	22.11
Na2O	4.48	4.48	4.48	4.48	4.48	4.48	4.48	4.48	4.48	4.48
K2O	0.00	0.16	0.00	0.00	0.00	0.01	0.00	0.00	0.02	0.00
Cl	0.00	0.00	0.01	0.01	0.01	0.00	0.00	0.00	0.02	0.00
F	0.00	0.00	0.00	0.00	0.00	0.00	0.00	0.00	0.00	0.00
Total	102.87	101.59	103.14	101.55	101.40	103.66	103.92	102.62	100.18	100.87
Jadeite	0.305	0.309	0.304	0.309	0.309	0.303	0.303	0.305	0.315	0.310
Diopside	0.501	0.490	0.511	0.487	0.491	0.509	0.494	0.525	0.431	0.509
Hedenbergite	0.194	0.201	0.185	0.203	0.199	0.188	0.203	0.171	0.254	0.181
Aegirine	0.000	0.000	0.000	0.000	0.000	0.000	0.000	0.000	0.000	0.000

Wt% Oxide	Composition 11	Composition 12	Composition 13	Composition 14	Composition 15
SiO2	51.19	51.81	50.84	52.43	51.59
TiO2	0.11	0.17	0.27	0.47	0.50
Al2O3	1.62	2.14	2.99	4.74	5.48
Cr2O3	0.00	0.01	0.01	0.02	0.04
FeO	9.55	9.26	9.48	8.54	9.07
MnO	0.12	0.11	0.10	0.08	0.05
MgO	13.49	12.95	12.92	12.30	11.40
ZnO	0.02	0.00	0.00	0.00	0.02
CaO	22.21	22.37	20.88	21.20	20.50
Na2O	4.48	4.48	4.48	4.48	4.48
K2O	0.00	0.00	0.04	0.00	0.00
Cl	0.01	0.00	0.01	0.00	0.00
F	0.00	0.00	0.00	0.00	0.00
Total	102.80	103.31	102.03	104.26	103.12
Jadeite	0.305	0.304	0.308	0.301	0.306
Diopside	0.497	0.497	0.490	0.503	0.480
Hedenbergite	0.198	0.199	0.202	0.196	0.214
Aegirine	0.000	0.000	0.000	0.000	0.000

15 clinopyroxene compositions from EPMA of clinopyroxenes in sample T01-40. Highlighted in orange is the reintegrated whole-rock sodium oxide component in sample T01-40 – inferred to represent the amount of sodium present in former clinopyroxene at peak metamorphic conditions. Additionally, the clinopyroxene end-member proportions are given below the compositions. The average Jadeite value from the 15 compositions is 0.306.